

COMPUTATIONAL FLUID DYNAMICS MODEL OF
ETHYLENE-BUTENE COPOLYMERIZATION IN
FLUIDIZED BED REACTOR



Mr. Suchart Kreesaeng

จุฬาลงกรณ์มหาวิทยาลัย
CHULALONGKORN UNIVERSITY

A Dissertation Submitted in Partial Fulfillment of the Requirements
for the Degree of Doctor of Philosophy in Chemical Technology
Department of Chemical Technology
FACULTY OF SCIENCE
Chulalongkorn University
Academic Year 2022
Copyright of Chulalongkorn University

แบบจำลองพลศาสตร์ของไหลเชิงคำนวณของการเกิดพอลิเมอร์ร่วมเอทิลีน-บิวทีน
ในเครื่องปฏิกรณ์แบบฟลูอิดไคซ์เบด



วิทยานิพนธ์นี้เป็นส่วนหนึ่งของการศึกษาตามหลักสูตรปริญญาวิทยาศาสตรดุษฎีบัณฑิต
สาขาวิชาเคมีเทคนิค ภาควิชาเคมีเทคนิค
คณะวิทยาศาสตร์ จุฬาลงกรณ์มหาวิทยาลัย
ปีการศึกษา 2565
ลิขสิทธิ์ของจุฬาลงกรณ์มหาวิทยาลัย

Thesis Title	COMPUTATIONAL FLUID DYNAMICS MODEL OF ETHYLENE-BUTENE COPOLYMERIZATION IN FLUIDIZED BED REACTOR
By	Mr. Suchart Kreesaeng
Field of Study	Chemical Technology
Thesis Advisor	Professor PORNPOTE PIUMSOMBOON, Ph.D.
Thesis Co Advisor	Associate Professor BENJAPON CHALERMSINSUWAN, Ph.D.

Accepted by the FACULTY OF SCIENCE, Chulalongkorn University in Partial
Fulfillment of the Requirement for the Doctor of Philosophy

Dean of the FACULTY OF SCIENCE
(Professor POLKIT SANGVANICH, Ph.D.)

DISSERTATION COMMITTEE

----- Chairman
(Associate Professor PRASERT REUBROYCHAROEN,
Ph.D.)

----- Thesis Advisor
(Professor PORNPOTE PIUMSOMBOON, Ph.D.)

----- Thesis Co-Advisor
(Associate Professor BENJAPON CHALERMSINSUWAN,
Ph.D.)

----- Examiner
(Professor NAPIDA HINCHIRANAN, Ph.D.)

----- Examiner
(Associate Professor SOMPONG PUTIVISUTISAK, Ph.D.)

----- External Examiner
(Associate Professor Siripon Anantawaraskul, Ph.D.)

จุฬาลงกรณ์มหาวิทยาลัย
CHULALONGKORN UNIVERSITY

สุชาติ กรีแสง : แบบจำลองพลศาสตร์ของไหลเชิงคำนวณของการเกิดพอลิเมอร์ร่วมเอทิลีน-บิวทีนในเครื่องปฏิกรณ์แบบฟลูอิดไคซ์เบด. (COMPUTATIONAL FLUID DYNAMICS MODEL OF ETHYLENE-BUTENE COPOLYMERIZATION IN FLUIDIZED BED REACTOR) อ.ที่ปรึกษาหลัก : ศ. ดร.พรพจน์ เปี่ยมสมบูรณ์, อ.ที่ปรึกษาร่วม : รศ. ดร.เบญจพล เกลิมสินสุวรรณ

พลศาสตร์ของไหลเชิงคำนวณเป็นเครื่องมือที่มีประสิทธิภาพสำหรับการศึกษาปรากฏการณ์ของไหลในระบบต่างๆ ในการศึกษาจะมุ่งเน้นไปที่การพัฒนาแบบจำลองเพื่อใช้ศึกษาการเกิดปฏิกิริยาการเกิดพอลิเมอร์ร่วมในเครื่องปฏิกรณ์แบบฟลูอิดไคซ์เบด แบบจำลองจะประกอบไปด้วยสองส่วนหลัก คือ แบบจำลองอุทกพลศาสตร์และแบบจำลองพอลิเมโรไลเซชัน แบบจำลองอุทกพลศาสตร์ถูกใช้ในการวิเคราะห์พฤติกรรมการแยกตัวของอนุภาคภายในระบบ จากการจำลองได้ว่าการใส่แผ่นกั้นเข้าไปในเครื่องปฏิกรณ์สามารถช่วยลดการแยกตัวได้ โดยเฉพาะอย่างยิ่ง การใส่แผ่นกั้นทำมุม 45 องศาตรงกลางส่วนการเกิดปฏิกิริยา และใส่แผ่นกั้นอีกชั้นเหนือแผ่นแรกจะช่วยลดให้พฤติกรรมการแยกตัวได้อย่างมีประสิทธิภาพสูงสุด นอกจากนี้แบบจำลองพอลิเมโรไลเซชันได้รับการพัฒนาโดยใช้วิธีการแบบโมเมนต์ วิธีการนี้ทำให้สามารถสมมูลมวลของสปีชีส์ถูกโซ่ง่ายขึ้น ทำให้สามารถจัดการชุดสมการได้มากขึ้น เมื่อจับคู่แบบจำลองอุทกไดนามิกกับแบบจำลองพอลิเมโรไลเซชัน จึงมีความเป็นไปได้ที่จะแสดงปฏิกิริยาโคพอลิเมอร์ของเอทิลีนและ 1-บิวทีน แบบจำลอง CFD ให้ข้อมูลเชิงลึกเกี่ยวกับปฏิกิริยาโคพอลิเมอร์โรไลเซชัน โดยได้รับพารามิเตอร์ที่สำคัญ เช่น น้ำหนักโมเลกุลเฉลี่ยและดัชนีการกระจายตัวหลายส่วน พารามิเตอร์เหล่านี้สามารถวิเคราะห์ได้โดยใช้เครื่องมือทางสถิติ ซึ่งนำไปสู่ความเข้าใจที่ดีขึ้นเกี่ยวกับกระบวนการโคพอลิเมอร์โรไลเซชันในเครื่องปฏิกรณ์ฟลูอิดไคซ์เบด โดยรวมแล้ว แบบจำลอง CFD ที่พัฒนาขึ้นมีส่วนช่วยให้เกิดความรู้และความเข้าใจเกี่ยวกับปฏิกิริยาโคพอลิเมอร์โรไลเซชัน และเป็นเครื่องมือที่มีคุณค่าสำหรับการออกแบบเครื่องปฏิกรณ์ที่เหมาะสมและปรับปรุงคุณภาพผลิตภัณฑ์พอลิเมอร์

จุฬาลงกรณ์มหาวิทยาลัย
CHULALONGKORN UNIVERSITY

สาขาวิชา เคมีเทคนิค
ปีการศึกษา 2565

ลายมือชื่อนิสิต
ลายมือชื่อ อ.ที่ปรึกษาหลัก
ลายมือชื่อ อ.ที่ปรึกษาร่วม

6072860923 : MAJOR CHEMICAL TECHNOLOGY

KEYWORD CFD, Polymerization, Polyethylene, Fluidized bed reactor,
D: Segregation

Suchart Kreesaeng : COMPUTATIONAL FLUID DYNAMICS MODEL OF ETHYLENE-BUTENE COPOLYMERIZATION IN FLUIDIZED BED REACTOR. Advisor: Prof. PORNPOTE PIUMSOMBOON, Ph.D. Co-advisor: Assoc. Prof. BENJAPON CHALERMSINSUWAN, Ph.D.

Computational fluid dynamics (CFD) is a powerful tool for studying fluid phenomena in various systems. In this study, the focus is on developing a CFD model to investigate the copolymerization reaction in a fluidized bed reactor. The CFD model consists of two main parts: the hydrodynamic model and the polymerization model. The hydrodynamic model was used to analyze the particle segregation behavior within the system. The simulations revealed that the introduction of baffles into the reactor could reduce segregation. Particularly, inserting a baffle at a 45-degree angle in the middle of the reaction zone, and adding another baffle layer above the first one, proved to be the most effective approach in minimizing segregation behavior. On the other hand, the polymerization model is developed using the method of moments approach. This approach simplifies the mass balance equations for chain species, allowing for a more manageable set of equations. By coupling the hydrodynamic model with the polymerization model, it becomes possible to represent the copolymerization of ethylene and 1-butene. The CFD model provides insights into the copolymerization reaction by obtaining important parameters such as average molecular weight and polydispersity index. These parameters can be analyzed using statistical tools, leading to a better understanding of the copolymerization process in the fluidized bed reactor. Overall, the developed CFD model contributes to the knowledge and understanding of copolymerization reactions, and it serves as a valuable tool for optimizing reactor design and improving polymer product quality.

จุฬาลงกรณ์มหาวิทยาลัย
CHULALONGKORN UNIVERSITY

Field of Study: Chemical Technology

Student's Signature

Academic 2022

.....
Advisor's Signature

Year:

.....
Co-advisor's Signature

.....

ACKNOWLEDGEMENTS

Although this research project was on a topic that I had little prior knowledge of and presented numerous challenges, I successfully completed it with the invaluable help of my advisors, co-advisors, and other professors who provided guidance and advice. I am immensely grateful to Prof. Dr. Pornpote Piumsomboon for serving as my advisor, Assoc. Prof. Dr. Benjapon Chalermnsinsuwan for being my co-advisor, and Asst. Prof. Dr. Teerawat Sema for their unwavering support, guidance, and assistance in all aspects of my research.

I would also like to express my gratitude to all the members of the Cybernetics Lab who provided assistance throughout the research process. Their contributions and collaboration were instrumental in the success of this project.

Furthermore, I would like to acknowledge the financial support received from the Grant from the Doctoral Degree Chulalongkorn University 100th Year Birthday Anniversary and the Overseas Research Experience Scholarship for Graduate Students. Their support enabled me to conduct my research and gain valuable international research experience.

Lastly, I extend my sincere appreciation to the Department of Chemical Technology, Faculty of Science at Chulalongkorn University for providing me with the opportunity to pursue my Ph.D. studies. Their belief in my potential and the resources they provided were essential in the fulfillment of my academic journey.

Suchart Kreesaeng

TABLE OF CONTENTS

	Page
.....	iii
ABSTRACT (THAI)	iii
.....	iv
ABSTRACT (ENGLISH).....	iv
ACKNOWLEDGEMENTS.....	v
TABLE OF CONTENTS.....	vi
LIST OF FIGURES	ix
LIST OF TABLES	xiii
Chapter 1 Introduction.....	1
Objectives	2
Chapter 2 Theory and literature review	3
Polymer.....	3
Polymerization reaction and mathematical model.....	5
Chain polymerization	5
Mathematical model of chain polymerization.....	6
Copolymerization.....	7
Computational fluid dynamics.....	9
Discretization method.....	11
Method of moment	11
literature review	13
Chapter 3 Hydrodynamic model and segregation study	26
3.1 Introduction.....	26
3.2 Model development	26
Computational domain	26
Mesh construction	27

Mathematical model	28
Boundary condition	30
3.3 Model validation	31
Grid independency test	31
Model adjustment	32
3.4 Segregation investigation.....	34
Segregation behavior	34
Relative segregation rate	36
Effect of baffles on segregation behavior.....	37
Effect of baffles angle.....	46
Effect of stage number and arrangement.....	50
Effect of stage number.....	51
Effect of stage arrangement.....	56
Effect of baffle number.....	63
Chapter 4 Computational fluidized dynamics model of ethylene-butene copolymerization reaction in fluidized bed reactor	71
4.1 Introduction.....	71
4.2 Model Development	71
Computational Domain	71
Mesh Construction	72
Mathematical Model.....	73
Model assumption	75
Polymerization model.....	75
Boundary Condition	85
Initial conditions.....	86
4.3 Model Validation.....	87
4.4 Parametric Study.....	90
Simulation results	91
Average molecular weight.....	91

Effect of comonomer content	95
Effect of H ₂ to C ₂ ratio	97
Effect of the catalyst amount	99
Polydispersity index	101
Chapter 5 Conclusion.....	105
Part I: Hydrodynamic model and segregation study.....	105
Part II: Computational fluidized dynamics model of ethylene-butene copolymerization reaction in fluidized bed reactor	106
Research outcome and novel contribution.....	107
Limitation of the model	107
Recommendations for future studies	108
REFERENCES	109
VITA	113

LIST OF FIGURES

Figure 2.1 Random copolymer	4
Figure 2.2 Block copolymer	4
Figure 2.3 Graft copolymer.....	4
Figure 2.4 Alternate copolymer	4
Figure 2.5 Industrial fluidized bed polymerization reactor	14
Figure 2.6 Fluidized bed reactor and phase diagram	15
Figure 2.7 Industrial fluidized bed reactor and schematic diagram of the modeling structure.....	16
Figure 2.8 Schematic diagram of the modeling structure	18
Figure 2.9 The monomer conversion from CFD model	19
Figure 2.10 Contours of initiator mass fraction at impeller speeds of: (a) 50 rpm, (b) 500 rpm	20
Figure 2.11 Contour of temperature and monomer distribution in the reactor	22
Figure 3.1 Illustrator of computational domain	27
Figure 3.2 Illustration of the computational domain with a uniform size rectangular mesh shape	27
Figure 3.3 Pressure drop across the bed.....	31
Figure 3.4 Pressure drop across the bed comparison.....	33
Figure 3.5 Smallest particle bed height.....	34
Figure 3.6 Contour of smallest particle volume fraction	35
Figure 3.7 Contour of smallest particle volume fraction	35
Figure 3.8 Illustration of the baffle ^[31]	36
Figure 3.9 Computation domain of the reactor with 45-degree baffles	38

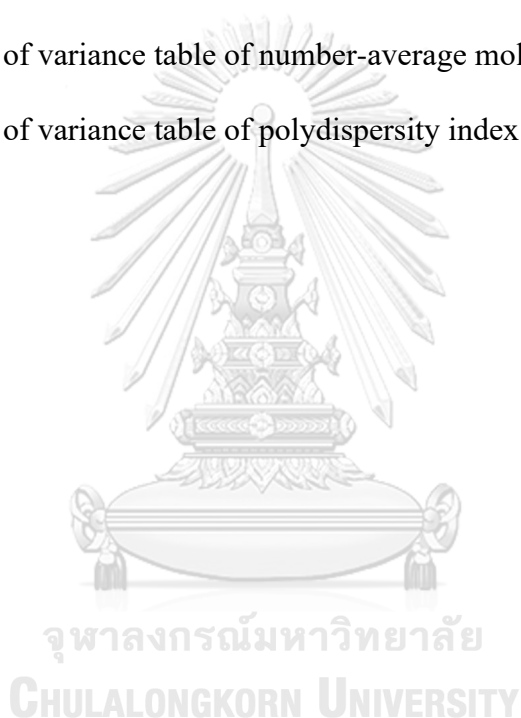
Figure 3.10 Computation domain of the reactor with 90-degree baffles	39
Figure 3.11 Relative segregation rate of the reactor without baffles, reactor with	39
Figure 3.12 Solid velocity vector within the no-baffles reactor	40
Figure 3.13 Solid velocity vector within the 45-degree baffles reactor	41
Figure 3.14 Solid velocity vector within the 90-degree baffles reactor	41
Figure 3.15 Solid y-velocity at the middle of reactor comparison	43
Figure 3.16 Overall solid volume fraction along reactor height comparison	43
Figure 3.17 Smallest particles volume fraction along reactor height comparison	44
Figure 3.18 Contour of smallest particles volume fraction comparison	45
Figure 3.19 Largest particles volume fraction along reactor height comparison	45
Figure 3.20 Contour of largest particles volume fraction comparison	46
Figure 3.21 Computation domain of the reactor with 30-degree baffles	47
Figure 3.22 Computation domain of the reactor with 60-degree baffles	47
Figure 3.23 Relative segregation rate of the reactor with difference baffles angle	48
Figure 3.24 Smallest particles volume fraction along reactor height comparison	49
Figure 3.25 Contour of the smallest particles volume fraction comparison	49
Figure 3.26 Largest particles volume fraction along reactor height comparison	50
Figure 3.27 Computation domain of the reactor of difference case (a) above case (b) below case and (c) expand case.	51
Figure 3.28 Relative segregation rate of the reactor with difference arrangement	52
Figure 3.29 Relative segregation rate of the reactor with difference arrangement	53
Figure 3.30 Smallest particle streamline of single stage and 2 stages case	53
Figure 3.31 Smallest particle mass flow rate through the first stage	54
Figure 3.32 Smallest particle streamline of single stage and 2 stages cases	55

Figure 3.33 Largest particles volume fraction along reactor height comparison.....	55
Figure 3.34 Smallest particles volume fraction along reactor height comparison.....	56
Figure 3.35 Smallest particles volume fraction along reactor height comparison.....	56
Figure 3.36 Smallest particle streamline of below and expand case	57
Figure 3.37 Largest particle mass flow rate through the first stage	58
Figure 3.38 Smallest particle mass flow rate through the second stage	59
Figure 3.39 Largest particle volume fraction along reactor height.....	60
Figure 3.40 Smallest particle volume fraction along reactor height.....	61
Figure 3.41 Smallest streamline of above and expand case.....	62
Figure 3.42 Comparison of computational domain between 9 and 4 baffles	63
Figure 3.43 Solid velocity vector within the 9 baffles reactor.....	64
Figure 3.44 Solid velocity vector within the 4 baffles reactor.....	64
Figure 3.45 Area using to calculate mass flow rate through the baffles	65
Figure 3.46 Mass flow rate above the baffles for the smallest particles	66
Figure 3.47 Mass flow rate above the baffles for the largest particles	66
Figure 3.48 Amount of the smallest particle above the baffles.....	67
Figure 3.49 Amount of the smallest particle above the baffles.....	68
Figure 3.50 Largest particle volume fraction along reactor height.....	69
Figure 3.51 Smallest particle volume fraction along reactor height	69
Figure 3.52 Relative segregation rate	70
Figure 4.1 Illustrator of computational domain	72
Figure 4.2 Illustrator of computational grid.....	73
Figure 4.3 Flow diagram of the coupling model{Canonsburg, 2013 #148;Mastan, 2015 #145}.....	85

Figure 4.4 Comparison of weight-average and number-average molecular weight between literature data [28] and simulation model.....	87
Figure 4.5 Schematic diagram of literature model[6].....	88
Figure 4.6 Ethylene distribution in the system	89
Figure 4.7 Solid distribution in the system	89
Figure 4.8 Instantaneous weight-average molecular weight.....	92
Figure 4.9 Weight-average molecular weight at 18000 second	92
Figure 4.10 Instantaneous number-average molecular weight	93
Figure 4.11 Number-average molecular weight at 18000 second	94
Figure 4.12 1-butene concentration in the system comparison of run1 2 and 3	96
Figure 4.13 Hydrogen concentration in the system comparison of.....	97
Figure 4.14 Solid volume fraction in the system comparison of run 1 2 and 9.....	99
Figure 4.15 Instantaneous active catalyst amount in the system	100
Figure 4.16 Instantaneous polydispersity index.....	102
Figure 4.17 Polydispersity index at 18000 seconds.....	102
Figure 4.18 Percentage of molecular weight change.....	104

LIST OF TABLES

Table 3.1 Average pressure drop and the Courant number of each grid number.	32
Table 4.1 Elementary equation and species mole balance equation used in the model.	77
Table 4.2 Kinetic rate constant of elementary reaction.....	80
Table 4.3 Detail of the studied parameter of each run	91
Table 4.4 Analysis of variance table of weight-average molecular weight	95
Table 4.5 Analysis of variance table of number-average molecular weight	95
Table 4.6 Analysis of variance table of polydispersity index	103



Chapter 1 Introduction

Polyethylene is the most widely used raw material in the plastic industries. Polyethylene can be divided into 3 types according to density consist of low-density polyethylene: LDPE, linear low-density polyethylene: LLDPE and high-density polyethylene: HDPE. Each type of polyethylene is used in different application such as LDPE bag, LLDPE sealing film or HDPE tank. Since the economic expansion causes more polyethylene demand, thus suppliers have to increase the production capacity of polyethylenes.

In industrial scale, the polyethylene is produced by ethylene polymerization in a fluidized bed reactor. Modification of polyethylene polymerization reactors is important to increase its production capacity. However, the effects of reactor modification on polymer product quality are necessary to be investigated before implementing the reactor modification.

Nowadays, computational fluid dynamics is widely used to investigate the reactor modification effect on polymer product quality. Computational fluid dynamics is a method using conservation of mass, conservation of momentum and conservation of energy to predict the fluid phenomena in a computational domain. Computational fluid dynamics can be adapted to use in the complicated system by including additional equation into the calculation model such as conservation of species.

Moreover, other calculation equation such as reaction rate equation can be included into the program through user define function predicting chemical reactions inside the reactor.

To predict polymerization phenomena in the reactor through computational fluid dynamics technique, the polymerization reaction model has to be included into the calculation model. Since the complication of polymerization reaction, the reaction model was derived by using method of moment approach. The advantage of this method is that it simplifies a theoretically infinite number of mass balance equations of chain species into smaller set of equations.

In this study, the CFD model couple with method of moment is used to study the copolymerization of ethylene and 1-butene in a fluidized bed reactor to investigate the effect of operation parameters on quality of polymer product. The operation parameters are superficial gas velocity, inlet gas components, catalyst feed rate. The quality to be observed are molecular weight, polydispersity index and melt flow index.

Objectives

- To develop computational fluid dynamics model of ethylene-butene copolymerization reaction in fluidized bed reactor
- To study effects of operation parameters on quality of polymer product such as molecular weight, polydispersity index

Chapter 2

Theory and literature review

Polymer

A polymer is a large molecule composed of repeating units called monomers. Monomers, as reactants, undergo a transformation to become monomeric units, which then bond together to form a polymer chain [1]. The types of polymers vary depending on the type of monomer, such as polystyrene, polyethylene, polyvinyl chloride, and others. Furthermore, different types of polymers are used in various applications due to their distinct properties.

When considering the monomeric units within the polymer chain, polymers can be classified into two types: homopolymers and copolymers. Homopolymers are polymer chains that consist of a single type of monomeric unit. Copolymers, on the other hand, contain more than one type of monomeric unit, which enhances the polymer's properties compared to homopolymers. The distribution of monomeric units in a copolymer chain can follow four patterns, as shown in Figure 2.1-2.4.

The first pattern is a random copolymer, where the positions of monomeric units in the chain occur randomly without any specific sequence or relation to other monomeric units. The second pattern is a block copolymer, which consists of large groups of different monomeric unit types linked together in distinct blocks. The third pattern is a graft copolymer. Similar to block copolymers, graft copolymers also contain large groups of different monomeric unit types. However, in graft copolymers, one large group of monomeric units forms the backbone chain, while the other large group is grafted onto the backbone chain. The last pattern is an alternating copolymer, where different monomeric units in the chain link together alternately.



Figure 2.1 Random copolymer



Figure 2.2 Block copolymer

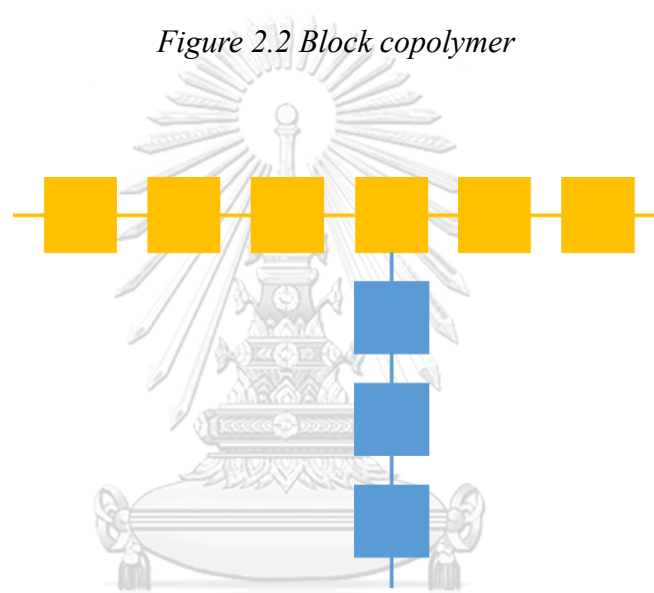


Figure 2.3 Graft copolymer

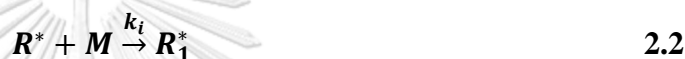


Figure 2.4 Alternate copolymer

Polymerization reaction and mathematical model

Chain polymerization

Polymerization is a process that results in the formation of a polymer. It can be categorized into three mechanisms: addition polymerization, condensation polymerization, and ring-opening polymerization. Chain polymerization is one of the types of addition polymerization. Chain polymerization can be divided into three steps: initiation, propagation, and termination.



In this step, the initiator combined with the first monomer forms a live polymer chain with a length of one [2]. The next step is the propagation step, where this live polymer chain continuously reacts with monomers. The majority of the monomers are consumed during this step, leading to the growth of the live polymer chain.



The final step is the termination step. During this step, the live polymer chain undergoes a transformation into a dead polymer chain that is no longer capable of reacting with monomers and growing further. Dead polymer chains can result from chain transfer reactions, which can be triggered by various factors such as monomers, cocatalysts, and hydrogen gas. Additionally, dead polymer chains can also arise from other reactions, including spontaneous transfer reactions.





Mathematical model of chain polymerization

Various mathematical models have been developed with different assumptions to investigate polymerization mechanisms within a system. These models are employed to study and understand the processes involved in polymerization.

$$R_p = k_p[M][R^*] \quad 2.6$$

However, determining the concentration of live polymer chains in the system can be challenging. As a result, several mathematical models have been developed to address this issue.

One such model is the steady-state hypothesis, which considers the three main steps of the polymerization mechanism: initiation, propagation, and termination.

$$R_i = 2fk_d[I] \quad 2.7$$

$$[I] = [I]_0 \exp(-k_d t) \quad 2.8$$

$$R_t = 2k_t[R^*]^2 \quad 2.9$$

The steady-state hypothesis assumes that the concentration of live polymer chains remains constant, meaning that the rate of initiator equals the termination rate. The majority of the monomers are consumed during the propagation step. In this model, an important equation is the consumption rate of monomer, which describes the rate at which monomers are consumed during the polymerization process.

$$R_i = R_t \quad 2.10$$

$$2fk_d[I] = 2k_t[R^*]^2 \quad 2.11$$

$$[R^*] = \left(\frac{R_i}{2k_t}\right)^{1/2} = \left(\frac{fk_d[I]}{k_t}\right)^{1/2} \quad 2.12$$

$$R_p = k_p[M] \left(\frac{fk_d[I]}{k_t}\right)^{1/2} \quad 2.13$$

$$[M] = [M]_0 \exp\left(-2k_p \left(\frac{f[I]_0}{k_t k_d}\right)^{1/2} \left(1 - \exp\left(\frac{-k_d t}{2}\right)\right)\right) \quad 2.14$$

$$v = \frac{R_p}{R_i} = \frac{R_p}{R_t} \quad 2.15$$

$$v = \frac{k_p[M][R^*]}{2fk_d[I]} = \frac{k_p[M][R^*]}{2k_t[R^*]^2} \quad 2.16$$

$$v = \frac{k_p[M]}{2(fk_d k_t [I])^{1/2}} \quad 2.17$$

$$v = \frac{k_p^2 [M]^2}{2k_t R_p} \quad 2.18$$

$$\bar{X}_n = 2v \quad 2.19$$

$$\bar{X}_n = v \quad 2.20$$

$$\bar{M}_n = M_{su} \bar{X}_n \quad 2.21$$

Copolymerization

Copolymerization is a process that produces a polymer using two types of monomers. The properties of the polymer product can be influenced by both polymers derived from each monomer. However, the properties of the copolymer product are dependent on the ratio of each monomer in the polymer chain. The properties of the copolymer product may resemble those of the homopolymer product produced from the monomer with a higher ratio in the chain.

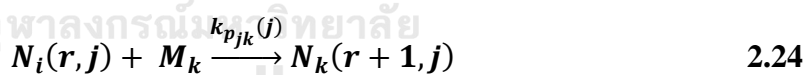
Polyethylene is one of the polymer products that can be produced through copolymerization. In this process, ethylene and 1-butene are used as the monomer and comonomer, respectively. The catalyst and cocatalyst employed in this process are $TiCl_4$ and $AlEt_3$, respectively. In copolymerization, only the last molecule in the live chain is considered.

To develop a numerical model for copolymerization mechanisms, the terminal model is commonly utilized. In this model, the kinetic rate of the reaction occurring in the system is dependent on the molecule at the end of the chain. Live chains with the same end molecule are considered equivalent, despite having different structures.

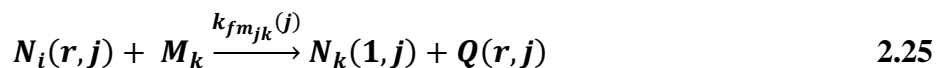
Catalyst activation



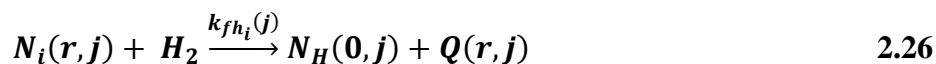
Propagation



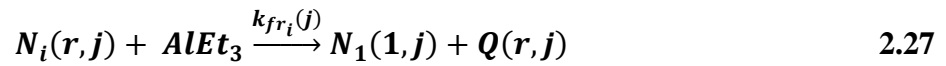
Transfer to monomer



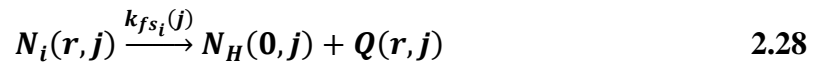
Transfer to hydrogen



Transfer to co-catalyst



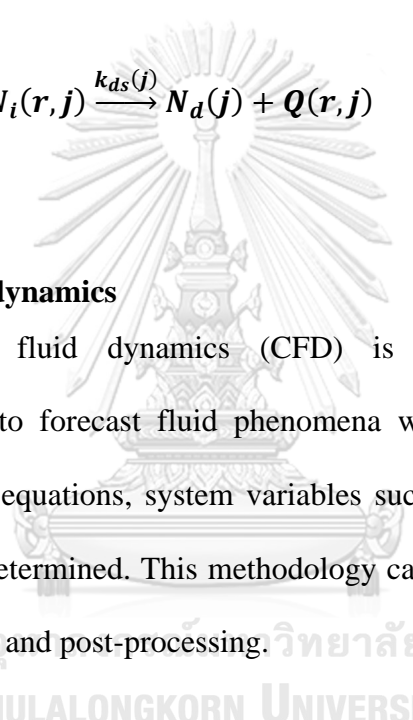
Spontaneous transfer



Deactivation reaction



Computational fluid dynamics

Computational fluid dynamics (CFD) is a technique that employs mathematical models to forecast fluid phenomena within a specified system. By solving the governing equations, system variables such as velocity, temperature, or mass fraction can be determined. This methodology can be divided into three stages: preprocessing, solving, and post-processing. 

During the preprocessing phase, the problem is defined, and the computational domain is established by setting system boundaries. In CFD, the finite volume method is utilized, which involves dividing the computational domain into small regions for 2D simulations or small volumes for 3D simulations. The boundary types are specified to accurately represent the real system.

CFD problems are solved based on the principles derived from the Navier-Stokes equations, which govern the motion of viscous fluids. These equations are mathematical representations that describe the physical properties of the fluid. Fluids,

regardless of whether they are liquids or gases, possess various crucial properties that determine their characteristics, such as density and viscosity.

Conservation of mass, or continuity equation

$$\frac{\partial \rho}{\partial t} + \nabla \cdot (\rho \vec{v}) = S_m \quad 2.30$$

Conservation of momentum

$$\frac{\partial}{\partial t}(\rho \vec{v}) + \nabla \cdot (\rho \vec{v} \vec{v}) = -\nabla p + \nabla \cdot (\bar{\bar{\tau}}) + \rho \vec{g} + \vec{F} \quad 2.31$$

Conservation of energy

$$\frac{\partial}{\partial t}(\rho E) + \nabla \cdot (\vec{v}(\rho E + p)) = \nabla \cdot \left(k_{\text{eff}} \nabla T - \sum_j h_j \vec{J}_j + (\bar{\bar{\tau}}_{\text{eff}} \cdot \vec{v}) \right) + S_h \quad 2.32$$

Species transport equation

$$\frac{\partial}{\partial t}(\rho Y_i) + \nabla \cdot (\rho \vec{v} Y_i) = -\nabla \cdot \vec{J}_i + R_i + S_i \quad 2.33$$

Scalar equation for additional equation

$$\frac{\partial \rho \phi_k}{\partial t} + \frac{\partial}{\partial x_i}(\rho u_i \phi_k - \Gamma_k \frac{\partial \phi_k}{\partial x_i}) = S_{\phi_k} \quad k = 1, \dots, N \quad 2.34$$

In the solving process, the governing equations, which encompass the continuity equation, momentum equation, energy equation, and species equation, are solved simultaneously. To simplify the calculations, the derivative equations are discretized using discretization methods. The choice of discretization method is

critical, as an improper selection can lead to imprecise solutions or instability of the solver.

Discretization method

In computational fluid dynamics (CFD), discretization methods play a crucial role in solving the governing equations that describe fluid flow phenomena. CFD deals with complex fluid flow problems that cannot be solved analytically, and numerical discretization techniques are employed to convert the partial differential equations (PDEs) representing fluid flow into algebraic equations that can be solved using computers. One of the discretization methods is finite volume method (FVM).

FVM is commonly used in solving problems involving conservation laws, such as fluid flow and heat transfer. The continuous domain is divided into control volumes or cells, and the governing equations are integrated over these volumes to obtain conservation equations. The method focuses on the conservation of mass, momentum, and energy within each control volume.

Method of moment

Indeed, the method of moments is a powerful tool for modeling polymerization processes. It involves utilizing moments to characterize and model the behavior of a polymerization system, where moments represent statistical measures of the distribution of molecular weights in the polymer chains.

In the context of polymerization modeling, the method of moments allows for the simplification of an infinite number of mass balance equations into a finite set of equations, which makes the modeling process more computationally feasible. By considering various moments of the molecular weight distribution, such as the mean,

variance, and higher order moments, this method provides a comprehensive understanding of the polymerization system.

To determine the moments, a system of differential or algebraic equations is solved, describing the evolution of the molecular weight distribution over time. These equations are derived based on assumptions and simplifications specific to the particular polymerization mechanism being investigated.

Overall, the method of moments offers a flexible and efficient approach to model polymerization processes and gain insights into the behavior of the resulting polymer products.

The method of moments indeed offers the advantage of simplifying an infinite number of mass balance equations for chain species into a smaller and more manageable set of equations. This simplification allows for a more efficient computational approach to modeling polymerization processes.

However, it is important to note that the method of moments has certain limitations. One of these limitations is that it does not consider the chain length dependence of reaction rate constants. In reality, the reaction rates may vary depending on the length of the polymer chains, but this aspect is not accounted for in the method of moments.

Regarding the definitions of the i^{th} moments for propagating radical and dead polymer in radical polymerization, they are represented by the variables Y and X , respectively, as given in Equations (35) and (36).

$$Y(n, j) = \sum_{r=1}^{\infty} r^n \{N_1(r, j) + N_2(r, j) + \dots\} \quad 2.35$$

$$X(n, j) = \sum_{r=1}^{\infty} r^n Q(r, j) \quad 2.36$$

Indeed, in the context of polymerization modeling using the method of moments, the zeroth order moment corresponds to the concentration of polymer chains in the system. It represents the overall abundance or concentration of polymer chains formed during the polymerization process.

On the other hand, the first order moment represents the concentration of monomeric units that have been incorporated into the polymer chains. It provides information about the extent of monomer consumption and incorporation into the growing polymer chains.

$$\bar{M}_n = \frac{\bar{m} \sum_{j=1}^{NS} \{X(1, j) + Y(1, j)\}}{\sum_{j=1}^{NS} \{X(0, j) + Y(0, j)\}} \quad 2.37$$

$$\bar{M}_w = \frac{\bar{m} \sum_{j=1}^{NS} \{X(2, j) + Y(2, j)\}}{\sum_{j=1}^{NS} \{X(1, j) + Y(1, j)\}} \quad 2.38$$

literature review

McAuley et al. [2] proposed the method to establish the mathematical model representing the copolymerization reaction of ethylene and 1-butene over a Ziegler-Natta catalyst in the fluidized bed reactor as shown in the Figure 2.1.

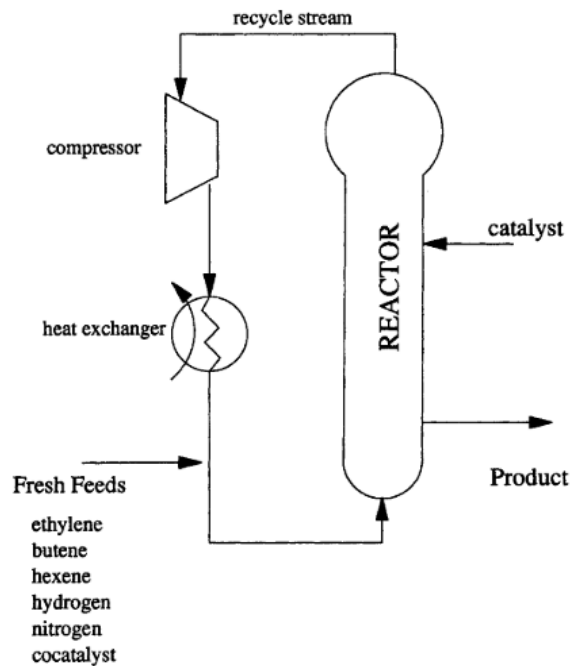


Figure 2.5 Industrial fluidized bed polymerization reactor

This model considered the system as a well-mixed gas in equilibrium with a solid phase. In this study, the copolymerization reaction mechanism consisted of basically reaction of polymerization reaction as formation and initiation, propagation, chain transfer, deactivation and reaction with poisons. Method of moment was used to develop kinetic model. Applying this method for copolymerization was different from the one for homopolymer. In case of copolymerization, total concentrations of monomer and copolymer were used in the mole balance equations; moreover, kinetic rate constant was pseudokinetic rate constant that was depending on the composition of monomer in the system and fraction of active site type of catalyst. To simplify the model calculation, this model was solved under steady state condition. The calculation results such as molecular weight, melt index and comonomer fraction in the chain were compared with actual plant data. The results showed a good agreement between calculation data and actual plant data. In addition, this model could predict the effect of carbon monoxide gas in the system that caused decreasing of production rate. However, there was an inaccurate data in the model due to unmodeled phenomena and catalyst variability.

Fernandes and Lona [3] proposed the mathematical model representing copolymerization reaction of ethylene and 1-butene in the fluidized bed reactor. This

model was 3 phases model consisted of gas bubble phase (representing excess gas flow through the bed as bubble), gas emulsion phase (representing consumed gas in the reaction) and solid emulsion phase (representing polymer particle). The phase diagram of this study is shown in the Figure 2.2.

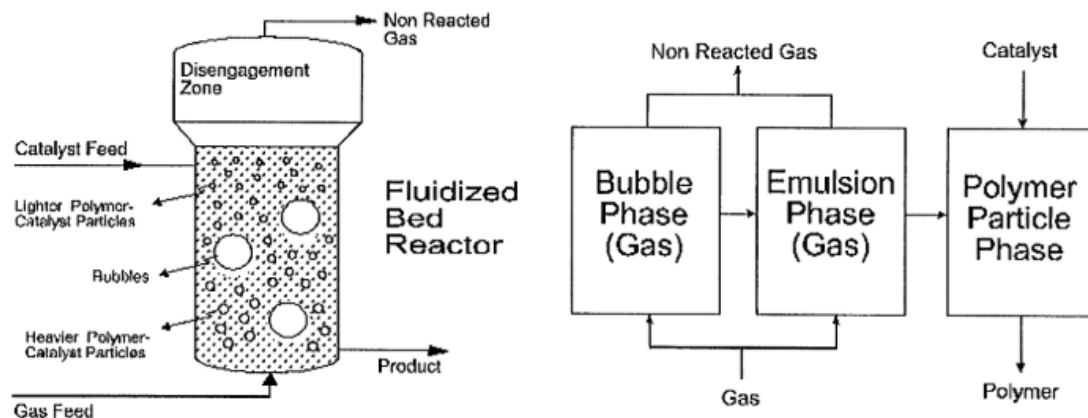


Figure 2.6 Fluidized bed reactor and phase diagram

In this study, plug flow reactor was used to represent the emulsion phase of gas and solid and CSTR was used to represent bubble phase of gas. Moreover, polymer particle segregating throughout the bed according to size and weight was included. The polymerization kinetic model was developed through method of moment. Calculation step that reduced the time require to solve the model was proposed. First, the system was solved without bubble phase. Then, gas emulsion phase was accounted into the calculation after that the bubble phase was accounted. At last, the energy balances were introduced into the calculation. The calculation results showed the rapidly increasing of molecular weight at the beginning of the reaction period. The predicted molecular weight was around 80000 g/mol as expected for these operating conditions; moreover, polymer production rate was 15 ton/h as expected for this reactor design. The result approved that this model could be used to predict the copolymerization in the fluidized bed reactor.

Kiashemshaki et al. [4] developed mathematical model of copolymerization reaction of ethylene and 1-butene over a Ziegler-Natta catalyst with two catalyst sites in the fluidized bed reactor. A gas-solid model was divided into reactor model and reaction model. The reactor model was used to predict the hydrodynamic. This model

used tank-in-series model to represent the fluidized bed reactor. The reaction model was developed from 7 elementary reactions through method of moment approach. According to the real production, melt index (MI) and density of polymer were easy to do on-line measurement thus MI and density were used to validate the model. Commonly, MI and density were the function of molecular weight (MW) and comonomer mole fraction, respectively. However, the relationship of MI and density with the operating condition and feed composition were proposed. The computational results of MI and density calculating from MW, operating condition and commercial software (CONGAR) were compared with the experimental results. In case of MI, MI from commercial software was closest to experimental data and MI from operating condition function was close to commercial software. However, all three calculation density values were satisfactory agreement with experimental data.

Alizadeh et al. [5] developed mathematical model of copolymerization reaction of ethylene and 1-butene over a Ziegler-Natta catalyst with two catalyst sites in the fluidized bed reactor. A gas-solid model composed of hydrodynamics model and kinetic model. The hydrodynamics model was developed through tank-in-series model. The reactor was separated into several CSTRs in series where the number of CSTRs depending on the fitting of outlet experimental data and computational data. The schematic diagram of the modeling structure compare with industrial fluidized-bed reactor is shown in the Figure 2.3.

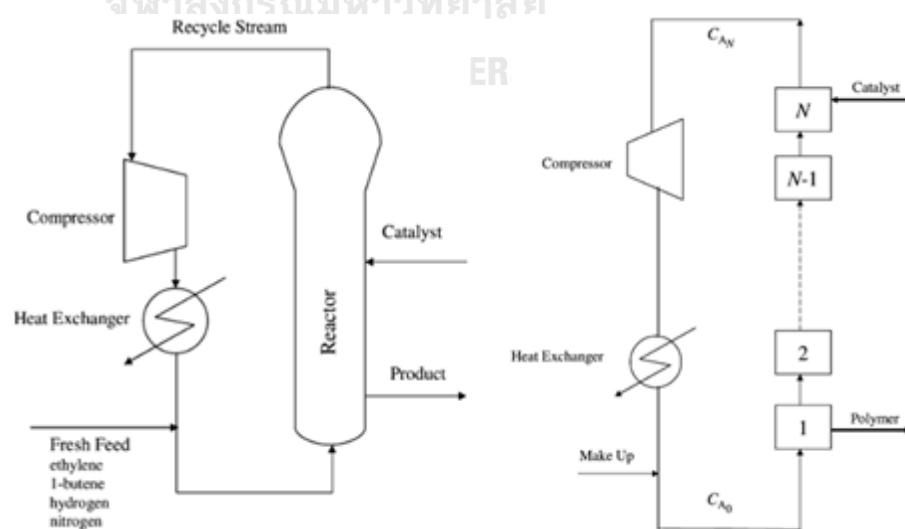


Figure 2.7 Industrial fluidized bed reactor and schematic diagram of the modeling structure

For realistic of simulation, the solid was contained in both bubble and emulsion phases where the solid concentration in each phase was depended on gas velocity. The kinetic model was developed through method of moment approach that could predict polymer product characteristic data. The calculation results showed a good agreement of melt index with actual plant data. In addition, the calculation results were consistent with the theory such as monomer conversion increased along the reactor height, and molecular weight increased rapidly at the beginning of the reaction. Those results approved that this method could be used to predict the polymerization reaction in the fluidized bed reactor.

Kiashemshaki et al. [6] developed mathematical model of copolymerization reaction of ethylene and 1-butene over a Ziegler-Natta catalyst with two catalyst sites in the fluidized bed reactor. A gas-solid model was divided into reactor model and reaction model. The reactor model was used to predict the hydrodynamics, this model divided fluidized bed reactor into 4 segments in series along the reactor height as shown in the Figure 2.4. The polymerization occurred in both bubble and emulsion phases; moreover, the bubble phase was represented by plug flow reactor and emulsion phase was represented by CSTRs. Those models were different from previous Kiashemshaki et al. [4] study that . The reaction model was developed with 7 elementary reactions through method of moment approach This method could predict the characteristics of product such as MW, PDI, density and MI as well as the other useful information such as production rate, monomer conversion and active site information. The computational results showed that 20% of polymer production was occurred in the bubble phase. Moreover, the results showed higher production rate when compared with solid-free model and showed more satisfactory agreement of MW distribution, PDI, temperature and production rate when comparing with experimental data.

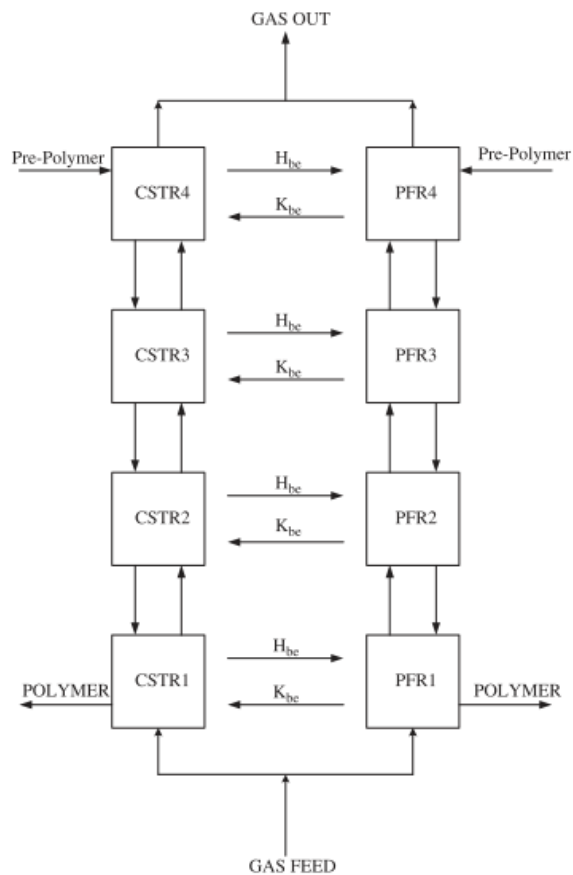


Figure 2.8 Schematic diagram of the modeling structure

Patel et al. [7] used CFD model to study effect of impeller speed, the input-output location and residence time on monomer conversion and hydrodynamics of the system. Multiple reference frames (MRF) was used to represent the rotation of the impeller. This study was focused on styrene polymerization reaction in the CSTR, three elementary reactions were used to develop kinetic model which were thermal initiation, propagation and termination. A steady state hypothesis was used to create the reaction source term. The calculation results showed the same trend of monomer conversion when comparing with CSTR model and experimental data. Due to the non-homogeneity of system, the monomer conversion from CFD model were between CSTR model and experimental data as shown in the Figure 2.5. Thus, the CFD model prediction was more realistic. With increasing impeller speed, the styrene was pushed from rich zone to vicinity of the reactor exit. The conversion of monomer decreased due to short-circuit effect of unreacted monomer. Input-output location was investigated. The results showed that mixing quality improved when input was placed

against the impeller. Improving mixing quality led to the independence of monomer conversion from impeller speed.

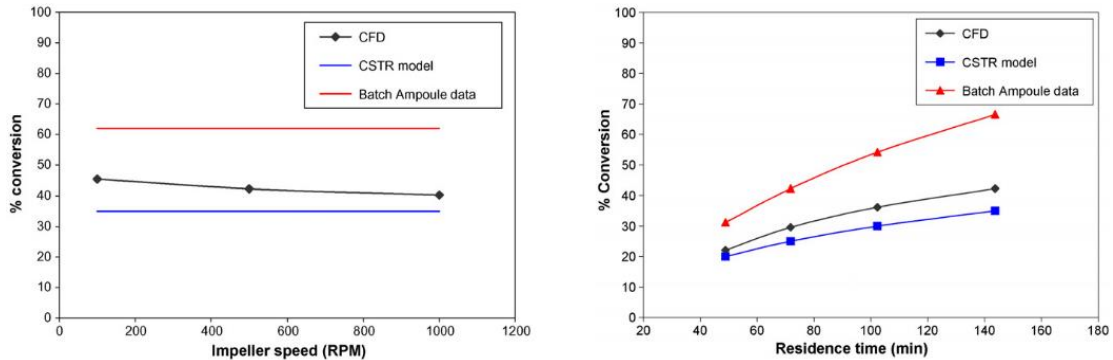


Figure 2.9 The monomer conversion from CFD model

Roudsari et al. [8] used CFD model to study polymerization reaction of methyl methacrylate (MMA) in a lab-scale stationary CSTR. This model consisted of transport model and a polymerization kinetic model. The transport model contained continuity, momentum, energy and species equations. Multiple reference frame (MRF) was included to transport model to represent rotating of the impeller. To develop the polymerization kinetic model, 6 elementary reactions including gel effect were used to develop the model through a steady-state hypothesis. Both transport model and polymerization kinetic rate model were solved under steady state condition with laminar flow regime. Since the computational results of monomer conversion showed the same trend as experimental data, thus, the model could be used to study the polymerization reaction in the CSTR. Moreover, increasing of temperature or initial monomer concentration increased monomer conversion. The homogeneity of the system was also increased as increasing impeller speed as shown in the Figure 2.6.

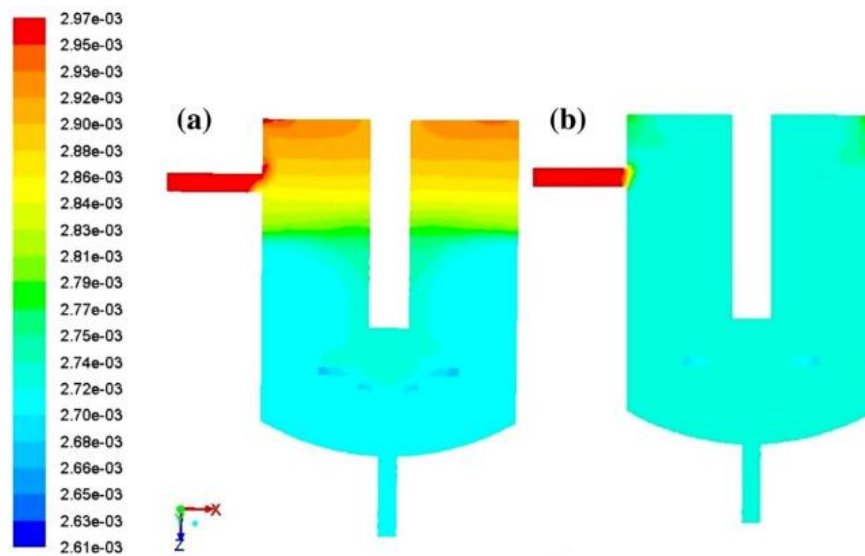


Figure 2.10 Contours of initiator mass fraction at impeller speeds of:
(a) 50 rpm, (b) 500 rpm

Mastan and Zhu [9] proposed the creating method of the mathematical model representing homopolymerization reaction through method of moment. The advantage of this method was simplifying a theoretically infinite number of the mass balance equations into a smaller set of equations. This method could predict the average value of polymer product characteristic data such as MW and PDI. However, when the distribution type was known, the average data could be used to construct the full distribution. In other hand, this method did not account for chain length dependence of reaction rate constant. In this study, the method of moment in difference reaction mechanism for all reaction mechanism was proposed. The method started with defined the elementary reaction occurred in the system the wrote the mole balance of the possible component in the system. After that, the mole balance equations were derived into the moment balance equation through the relationship between polymer concentration and moment. This study proposed that the second-order moment equation was enough to calculate the molecular weight and polydispersity index of polymer product.

Xu et al. [10] used CFD model couple with method of moment to study a polymerization reaction of styrene in a CSTR. The governing equation of CFD model which were continuity, momentum, energy and species equation including multiple reference model were solved under steady state condition. The moment equations

were included into the CFD model through user-defined scalar transport equation. To develop the moment equation, 4 elementary reactions as initiation, propagation chain transfer to monomer and termination by combination were used to create the mole balance equations where derived into moment equations that was a function of polymer concentration. The monomer conversion, molecular weight and polydispersity index were calculated. The monomer conversion data from model was a good agreement with literature data. The calculation results showed that the increasing of impeller speed increased the degree of homogeneity while decreased the monomer conversion and molecular weight due to the monomer dilution effect. Moreover, the residence time only affected the monomer conversion, but did not affect the molecular weight of the polymer.

To investigate effect of impeller speed, impeller type and feeding position on macroscopic (temperature, concentration) and microscopic (product molecular weight, polydispersity index) flow fields. Xie et. al [11] developed computational fluid dynamic (CFD) model coupling with method of moment to simulate the atom transfer radical copolymerization of methyl methacrylate and 2-(tri-methylsilyl) ethyl methacrylate in the CSTR. The CFD model was used to describe the macroscopic flow field; moreover, multiple reference model (MRF) was used to represent the rotation of reactor impeller. The method of moment was used to develop the polymerization kinetic equation to describe the microscopic flow field. This model was solved under unsteady state condition to validate the results and solved under steady state condition to study the parameters. The computational results of molecular weight and polydispersity index were in good agreement with the experimental data. The computational results showed that increasing of impeller speed decreased monomer conversion, molecular weight but increased polydispersity index. A dual state 45° pitch blade turbine impeller gave the most uniform temperature and reactant concentration distribution as shown in the Figure 2.7. Moreover, the results showed that the middle feeding mode improved temperature, reactant concentration distribution; nevertheless, bottom feeding mode promoted uniformity of molecular weight and polydispersity index distribution.

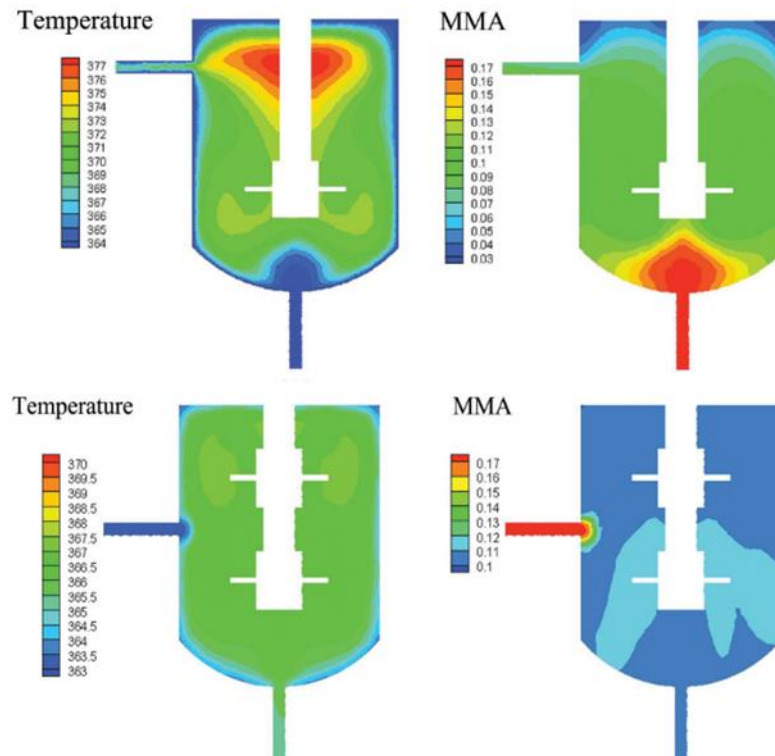


Figure 2.11 Contour of temperature and monomer distribution in the reactor

In the context of power plant applications, the fluidized bed reactor plays a crucial role in the combustion process of the boiler. Known as a fluidized bed combustor (FBC), this reactor is designed to efficiently burn coal and biomass fuels, accommodating a wide range of solid particle sizes. Typically, sand is used as the inert bed material in the FBC.

One of the key advantages of the fluidized bed reactor is its ability to achieve excellent mixing of solid particles within the system. This leads to effective heat transfer between gas-solid particles and solid-solid particles. Consequently, the temperature in the FBC reactor remains lower compared to conventional processes, while maintaining comparable combustion efficiency. The lower process temperature also results in reduced issues of slagging and fouling caused by ash-fusion, as well as decreased NOX emissions.[12]

The FBC reactor usually uses mixed-solid fuel that will affect the solid particle mixing in the system. Therefore, the solid particle behavior investigation is the key step to improve the FBC reactor. In the literature, the solid particle behavior in the FBC reactor was studied by many researchers [13-21], which focused on improving mixing behavior and solid segregation behavior. The multistage fluidized bed reactor was developed to improve the gas-solid particle mixing behavior. Wu et al. [13] studied the multistage fluidized bed in the desulfurization application. The multistage fluidized bed was developed by integrating two enlarged sections into the fluidized bed. The results showed that in the enlarged zone, the gas-solid particle mixing was enhanced. In addition, the back-mixing of the solid particle occurred at the lower cone zone. Kersten et al. [14] studied the multistage fluidized bed for the biomass gasification application. Two opposite cones were built up as a segment, and seven segments were integrated into the riser. The results showed that no back-mixing of gas and solid particles between the segments. Since a higher ratio between the solid residence time and the gas residence time than a normal fluidized bed, the carbon conversion and gasification efficiency were improved.

In a multistage countercurrent fluidized bed reactor, desulfurization and denitration were studied by Li et al. [15]. The distributor separated each stage in this multistage fluidized bed reactor with an overflow standpipe. Their multistage fluidized bed reactor provided a weak back-mixing of solid particles and high gas-solid particle contact time. Increasing the number of stages from 1 stage to 4 stages led to an increasing of the NO conversion while SO₂ was completely removed at the first stage. Davarpanah et al. [16] studied the adsorption of 1,2,4-trimethylbenzene on activated carbon in the multistage countercurrent fluidized bed adsorber. In similar to Li et al.,

the results showed the increasing of stages led to the increasing of removal efficiency. However, after adding two more stages from four to six stages, the removal efficiency decreased to 3.4% due to slow kinetics and the small concentration differences between the adsorbate and the adsorbent sites. For coal pyrolysis with char gasification application, Chen et al. [17] also studied a couple of those reactions in the same type of fluidized bed. As the stage numbers increased, the temperature gradient could be established. Moreover, carbon conversion, gas yield and tar yield were increased by increasing the number of the stages. On the other hand, some researchers improved the gas-solid particle mixing behavior by insert the baffle into the reactor. Yang et al. [18] used the perforated plates as the baffles and gas redistributors to study the flow characteristics of the bubbling fluidized beds. They found that average solid velocity was lower than that in the freely bubbling fluidized bed; moreover, solid particle back-mixing was prevented by the addition of baffle.

Hyun et al. [19] investigated mixing-segregation behavior in the fluidized bed reactor of a binary system of solid particles with different densities. The first solid particle was sand as jetsam, and the second one was Polymethylmethacrylate (PMMA). The results showed the effect of superficial gas velocity on segregation behavior. Increasing inlet velocity led to decreasing segregation degrees. Zhang et al. [20] studied the effect of exit geometries on the segregation of binary solid particles in the circulating fluidized bed system. Three exit geometries were studied, such as C-shape, T-shape and L-shape. In line with Hyun et al., Zhang et al. found that increasing the superficial gas velocity reduced the solid segregation. At the same time, T-shape and L-shape caused more coarse solid particles in the riser. Park et al. [21] studied the effect of column shape on the segregation behavior of char and sand. Circular, square

and rectangular columns were studied. Their study showed that the maximum segregation was observed at the ratio between superficial gas velocity and minimum fluidization velocity of 1.14. In the mixing region, column shape affected the mass fraction of char at the top of the bed. The char mass fractions were 0.53, 0.60 and 0.45 for the circular, rectangular and square shapes. The rectangular shape gave the smallest mixing index.



Chapter 3

Hydrodynamic model and segregation study

3.1 Introduction

To investigate the polymerization fluidized reactor using computational fluid dynamics (CFD) model, a simplified model was typically established first to study the hydrodynamics of the system. Therefore, in this study, the simplified model without the polymerization model was used to examine the fluid behavior in the fluidized reactor.

3.2 Model development

Computational domain

The computational domain used in this study was constructed based on the dimensions of the fluidized bed reactor reported in [22-24], which had a height of 33.9 meters and a diameter of 5 meters, with a reaction zone height of 20.5 meters. Figure 3.1 illustrates the computational domain that was employed in this study. To ensure a consistent flow rate of the gas phase, this model utilized the concept of the equivalent diameter [25] to define the reference depth of the model. The equivalent diameter in this model was 5 meters.

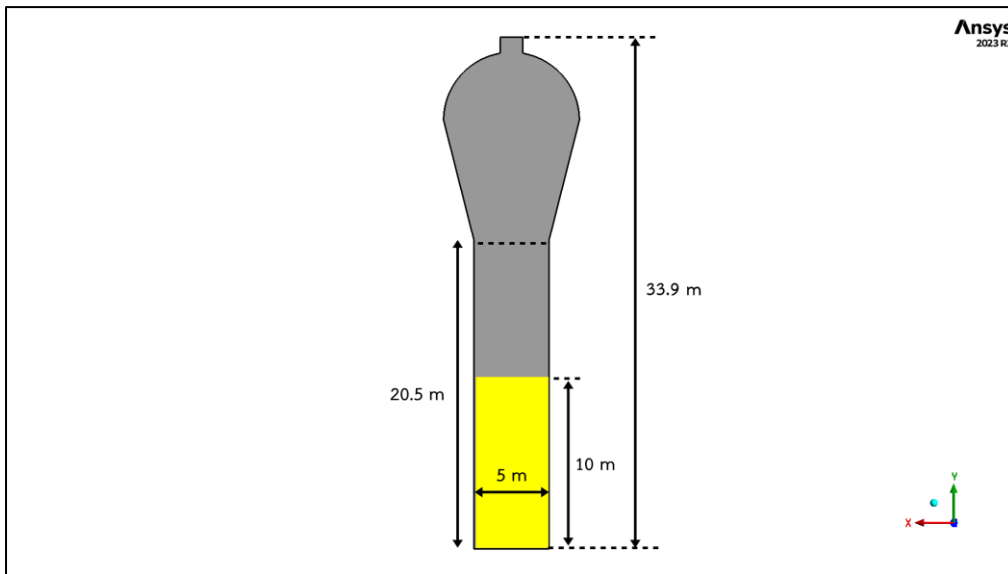


Figure 3.1 Illustration of computational domain

Mesh construction

To generate a mesh for the computational domain, a uniform size rectangular mesh shape was applied as shown in Figure 3.2.

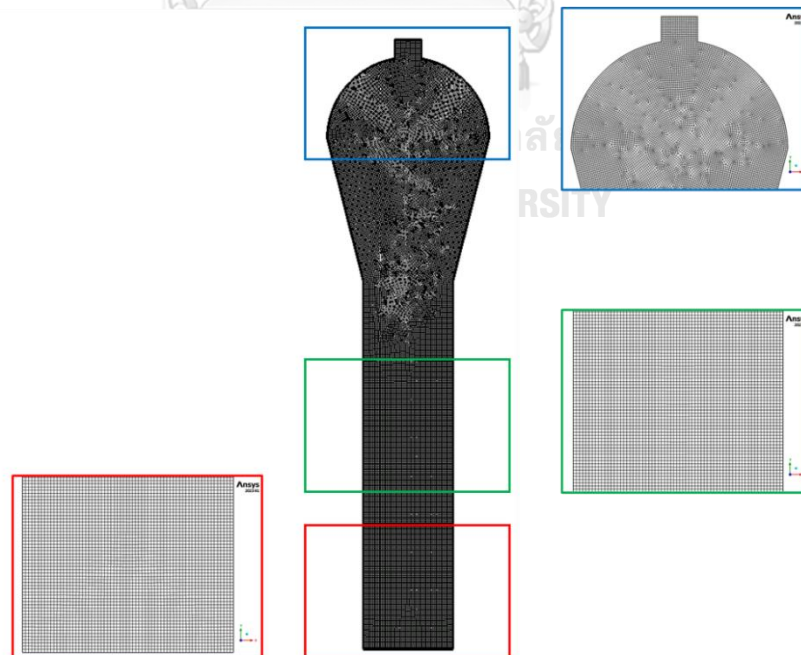


Figure 3.2 Illustration of the computational domain with a uniform size rectangular mesh shape

Grid sizes of 0.10, 0.075, and 0.05 meters were used in this study, resulting in grid numbers of 19,225 (coarse grid), 34,128 (medium grid), and 76,581 (fine grid), respectively. To ensure the accuracy and stability of the numerical simulations, the courant number, N_c , was also taken into consideration. This dimensionless number was calculated based on the time step size, mesh size, and inlet velocity, as described in previous works [26, 27]. The equation was.

$$N_c = U \frac{dt}{dx} \quad 3.1$$

The suggested range for the courant number is between 0.03 and 0.30 [27]. Within this range, the simulation results had no effect from mesh, time step and convergence criteria. Therefore, the courant numbers were 0.031, 0.042, and 0.062 for the coarse, medium, and fine grid sizes, respectively.

By carefully selecting appropriate grid sizes and ensuring that the Courant number remained within acceptable limits, the model was able to provide reliable and accurate numerical results for the simulations.

Mathematical model

In this chapter presents a study on the hydrodynamics of gas and particles in a reactor, utilizing a transient computational fluid dynamics model. A two-dimensional model with the Euler-Euler approach was employed to simulate this complex, multi-fluid system. The model consisted of conservation of mass and conservation of momentum equations, which were instrumental in analyzing the system's behavior.

The mass conservation equation for multiphase flow [28]

$$\frac{\partial}{\partial t}(\alpha_q \rho_q) + \nabla \cdot (\alpha_q \rho_q \vec{v}_q) = \sum_{p=1}^n (\dot{m}_{pq} - \dot{m}_{qp}) + S_q \quad 3.2$$

Where \vec{v}_q is the velocity of phase q and \dot{m}_{pq} characterizes the mass transfer from the p^{th} to q^{th} phase, and \dot{m}_{qp} characterizes the mass transfer from phase q^{th} to p^{th} phase.

The momentum conservation equation for multiphase flow [28]

$$\begin{aligned} \frac{\partial}{\partial t}(\alpha_q \rho_q \vec{v}_q) + \nabla \cdot (\alpha_q \rho_q \vec{v}_q \vec{v}_q) &= -\alpha_q \nabla p + \nabla \cdot \bar{\tau}_q + \alpha_q \rho_q \bar{g} \\ &+ \sum_{p=1}^n (\bar{R}_{pq} + \dot{m}_{pq} \vec{v}_{pq} - \dot{m}_{qp} \vec{v}_{qp}) \\ &+ (\bar{F}_q + \bar{F}_{lift,q} + \bar{F}_{wl,q} + \bar{F}_{vm,q} + \bar{F}_{td,q}) \end{aligned} \quad 3.3$$

where $\bar{\tau}_q$ is the q^{th} phase stress-strain tensor

$$\bar{\tau}_q = \alpha_q \mu_q \left(\nabla \vec{v}_q + \nabla \vec{v}_q^T \right) + \alpha_q \left(\lambda_q - \frac{2}{3} \mu_q \right) \nabla \cdot \vec{v}_q \bar{I} \quad 3.4$$

Where μ_q and λ_q are the shear and bulk viscosity of phase q , \vec{F}_q is an external body force, $\vec{F}_{lift,q}$ is a lift force, $\vec{F}_{wl,q}$ is a wall lubrication force, $\vec{F}_{vm,q}$ is a virtual mass force, and $\vec{F}_{td,q}$ is a turbulent dispersion force (in the case of turbulent flows only). \bar{R}_{pq} is an interaction force between phases, and p is the pressure shared by all phases. \vec{v}_{pq} is the interphase velocity.

According to the literature [24], three solid particle sizes (385, 765, and 1520 microns) were chosen to represent a wide range of particle size distribution (385-1520 microns), reflecting the real conditions of an industrial-scale gas-phase polymerization reactor. Therefore, to simulate the system's dynamic behavior, a four-

phase model was employed, comprising one gas phase and three solid particle phases. Each solid particle phase represented a different particle sizes (385, 765, and 1520 microns). Due to a good agreement between model data and actual data, Gidaspow drag model was used to handle interphase momentum exchange.

In this study, the model was solved using the commercial CFD package, ANSYS FLUENT 2023R1. The Phase Coupled SIMPLE algorithm [29] was employed to handle pressure-velocity coupling. Various spatial discretization schemes were used in the different equations in this model. To ensure stability in the four-phase model calculations, the first-order discretization, which generally yields better stability than the second order [30], was used. The first-order upwind scheme was employed to discretize the volume fraction. Moreover, the Third-Order MUSCL Scheme [28], applicable to arbitrary meshes, was used to discretize other equations to obtain more accuracy. An under-relaxation factor of 0.3 was adopted for all the variables. The convergence criterion used was 10^{-4} for continuity and 10^{-3} for other variables. The time step size was set to 0.01 seconds with a maximum of 30 iterations per time-step. The calculations were performed on a personal computer with an Intel Core i7 CPU.

Boundary condition

Three boundary conditions applied to the model consisted of the inlet, outlet, and wall. The system inlet was located at the bottom of the reactor. The system outlet was at the top of the reactor. Each boundary condition was as follows:

- For the inlet boundary condition, only gas was fed into the reactor with 0.312 m/s. The density and viscosity of mixture gas (C_2H_4 , C_4H_8 , O_2 , and N_2) at 2000 kPa were constant at 20 kg/m^3 and $1.2 \times 10^{-5} \text{ Pa.s}$, respectively.
- For the outlet boundary condition, constant pressure was set as the pressure outlet. Pressure at the outlet was set to 2000 kPa.
- For the wall boundary condition, the gas phase was set as a no-slip condition. All solid particle phases were set as the partially slip condition.

For the initial condition, the well-mixed particles were filled into 10 meters height from the bottom of the reactor with a volume fraction of 0.23 for each solid particle size. However, those initial conditions were obtained after adjusting the solid amount in the system and were validated with literature data.

3.3 Model validation

Grid independency test

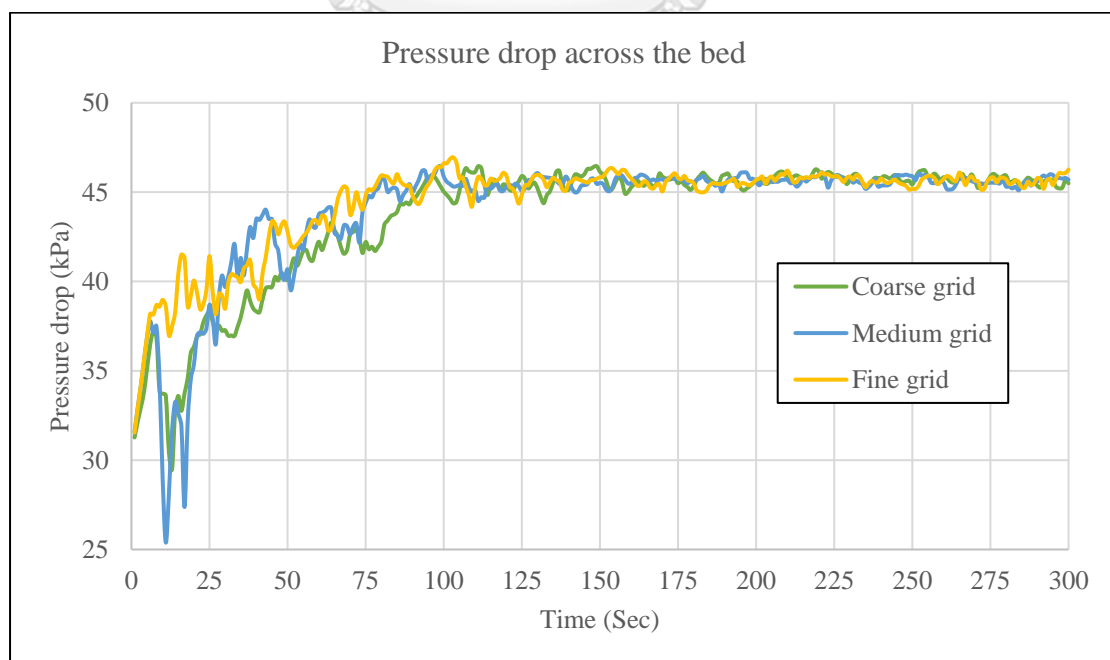


Figure 3.3 Pressure drop across the bed

Figure 3.3 showed transient pressure drop in the system of each grid size. The results showed that pressure drop was closed together for all grid size and reached quasi-steady state after 150 seconds of simulation time.

Table 3.1 Average pressure drop and the Courant number of each grid number.

Grid size (m)	Grid number	Courant number	Pressure drop (kPa)	%Difference
0.10	19225	0.031	13.81	-
0.075	34128	0.046	13.74	0.52
0.05	76581	0.052	13.67	0.47

In addition, the courant numbers were investigated by comparing the value of average pressure drop calculated from 200 to 250 seconds. The averaged pressure drop and the courant number of each grid size are shown in Table 3.1. From the table, the pressure drop decreased 0.52% when the grid number increased from 19,225 to 34,128. It further decreased 0.47% when the grid number increased from 34,128 to 76,581. As stated before, all grid numbers gave the courant number in the range of 0.03 to 0.30. It meant that the simulation results were independent of mesh, time-step and convergence criteria. Thus, to save computational resources, 34,128 grid number was an appropriate grid number to use further in this study.

Model adjustment

In order to verify the accuracy of the developed model, the pressure drop and bed height were compared to literature data reported by Akbari et al. [22-24], which were obtained from real industrial operation data. According to the literature, the

pressure drop of the reactor was approximately 58.8 kPa and the final bed height was 20 meters.

After adjusting the drag modification factor and initial solid volume fraction, the developed hydrodynamic model was validated by comparing the pressure drop and solid bed height. Figure 3.4 illustrates the comparison of the pressure drop between the model and the literature data. The calculated pressure drop was found to be almost 58.4 kPa, with only a 0.70% deviation from the literature data. In addition, the bed height obtained from the model was consistent with the literature data, as demonstrated in Figure 3.5. The results confirmed that the model accurately represents the hydrodynamics of the fluidized bed reactor system.

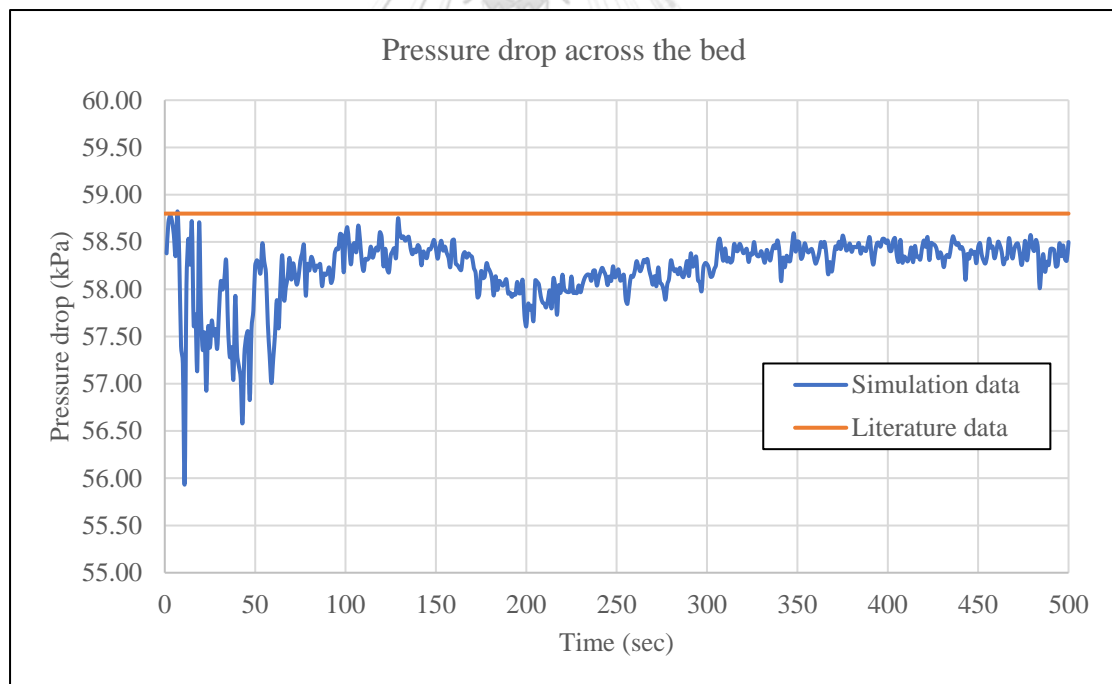


Figure 3.4 Pressure drop across the bed comparison

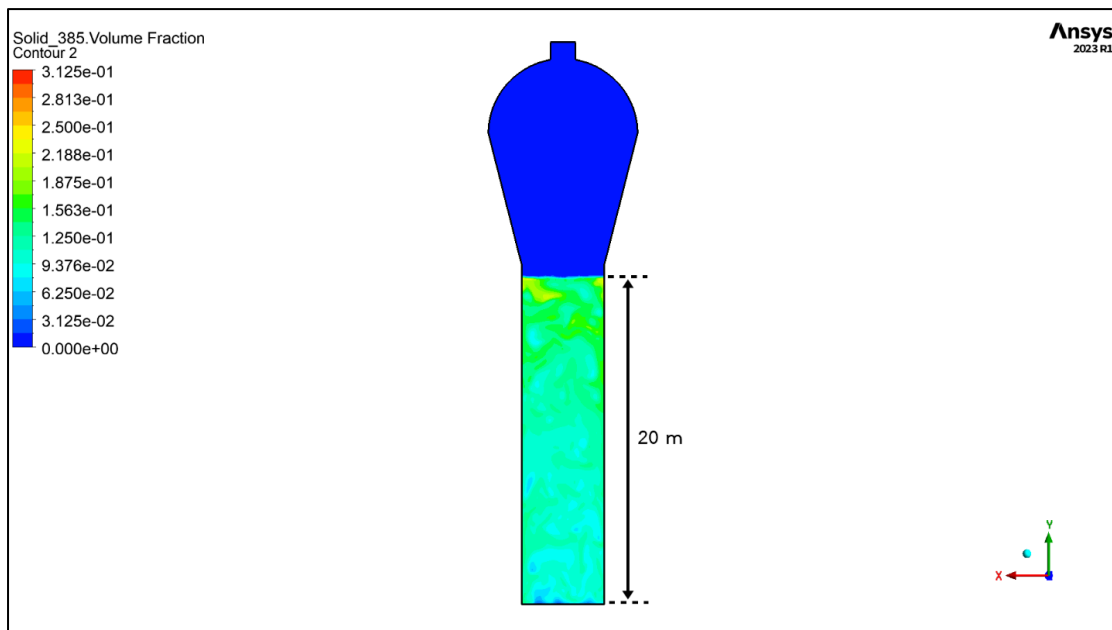


Figure 3.5 Smallest particle bed height

3.4 Segregation investigation

Segregation behavior

In this study, the segregation behavior was observed after a simulation time of 200 seconds. The results are presented in Figure 3.6 and Figure 3.7, which illustrate the contour of solid volume fraction of small and large particles, respectively, at different time intervals ranging from 50 to 500 seconds. The simulation results revealed that the small particles tended to accumulate at the top of the bed, while the large particles tended to accumulate at the bottom. This behavior indicates that the system had undergone segregation. The segregation behavior reduced the mixing of particles in the fluidized bed reactor, which, in turn, decreased the heat transfer between gas-particles and solid-particles, potentially leading to hot spots in the system. In the case of the polymerization fluidized bed reactor, the accumulation of

small particles, such as catalysts and co-catalysts, at the top of the bed could lead to a decrease in the polymerization reaction within the reactor.

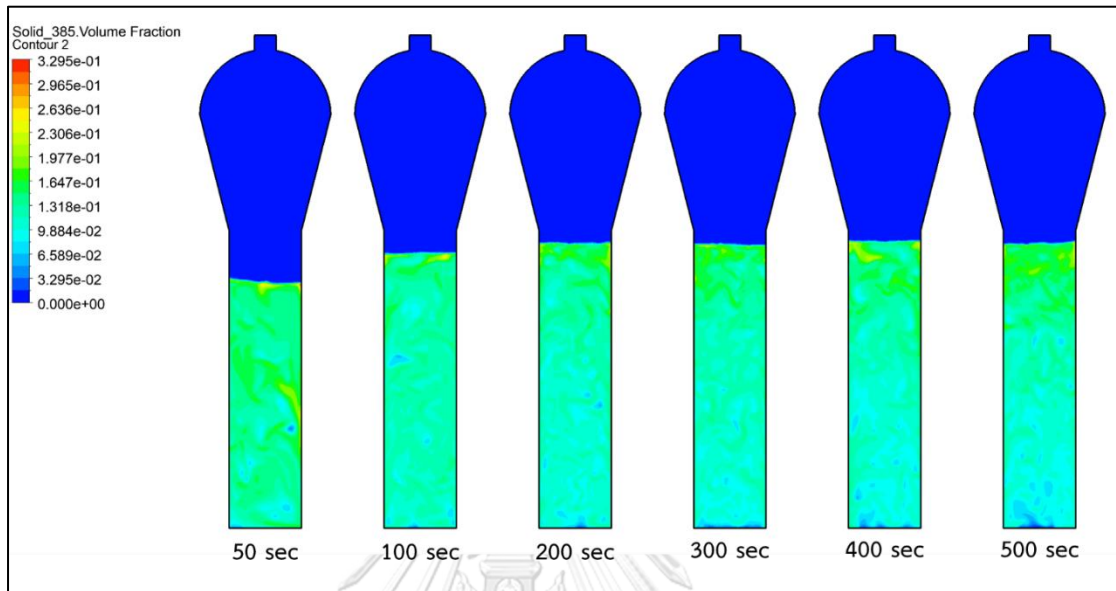


Figure 3.6 Contour of smallest particle volume fraction

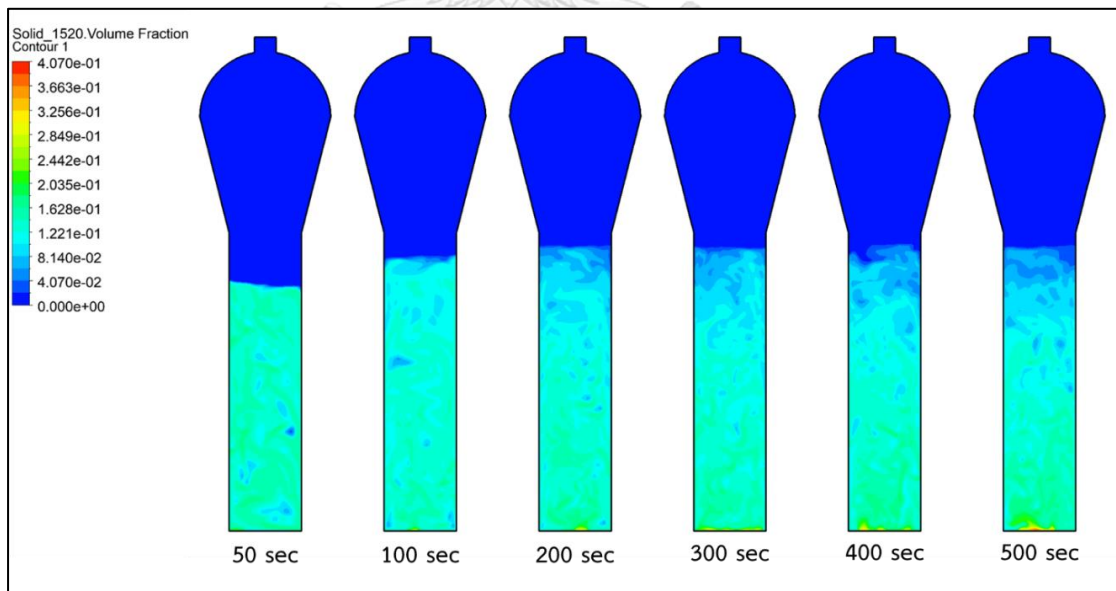


Figure 3.7 Contour of smallest particle volume fraction

In this study, the baffle as shown in Figure 3.8 was inserted into the computational domain to investigate the fluidized bed reactor with different baffle angles, arrangements, and numbers. The segregation behavior for each case was compared by calculating the relative segregation rate of the system.

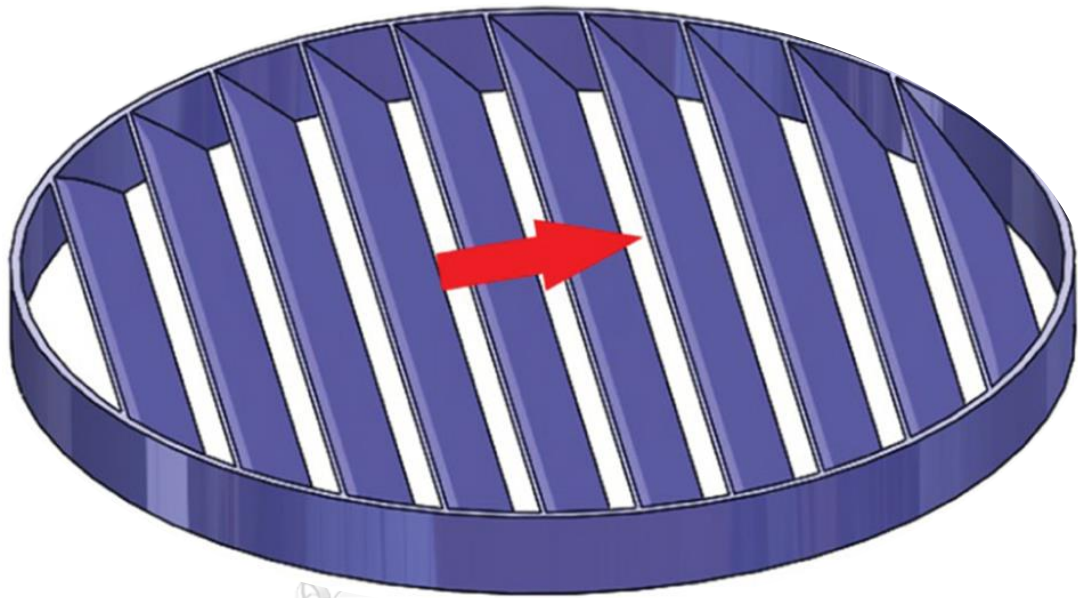


Figure 3.8 Illustration of the baffle^[31]

จุฬาลงกรณ์มหาวิทยาลัย

CHULALONGKORN UNIVERSITY

Relative segregation rate

To properly examine the impact of various parameters on the segregation behavior within the system, it was necessary to establish a response parameter that could effectively measure the degree of segregation. This parameter would serve as a quantitative indicator to assess the extent of segregation occurring in the system under different conditions.

Relative segregation rate was developed from digital image analysis method [32]. The fluidized bed system image was divided into small cells similar to the

computational fluid dynamics technique. The data within each cell was used to determine the average height of the particles within the fluidized bed from:

$$\langle h_i \rangle = \frac{\sum_k^{N_{Cells}} x_i \varepsilon_{si,k} h_k V_k}{\sum_k^{N_{Cells}} x_i \varepsilon_{si,k} V_k} \quad 3.5$$

Where $\langle h_i \rangle$ was average particle high of particle size i

x_i was mass fraction of particle size i in the cell

$\varepsilon_{si,k}$ was particle volume fraction of particle size i in the cell

h_k was height of cell

V_k was volume of cell

Then average particle heigh of small and large particle were used to calculate the relative segregation rate from:

$$S = \frac{S-1}{S_{max}-1} \quad 3.6$$

where $S = \langle h_{small} \rangle / \langle h_{large} \rangle$ and $S_{max} = \frac{2-x_{small}}{1-x_{small}}$

The relative segregation rate has the value between 0 and 1. When it is equal to 0, the particles are perfectly mixed on the other hand it is equal to 1 when the particles are completely segregated.

Effect of baffles on segregation behavior

In order to investigate the impact of baffles on the segregation of particles within the reactor, the validated model from the previous section was used to examine the fluid hydrodynamics in the system. Baffles with a width and height of 0.1 and 0.7 meters, respectively, were inserted at the midpoint of the reaction zone, situated at a

height of 10 meters. Two different baffle angles of 45 and 90 degrees were studied, as illustrated in Figures 3.9 and 3.10, respectively.

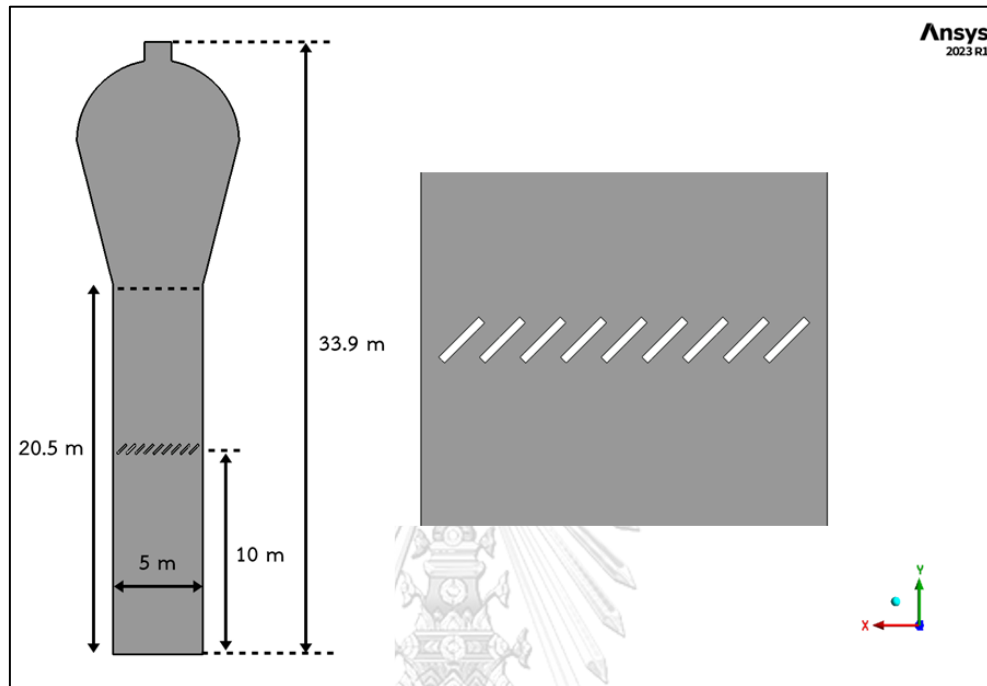


Figure 3.9 Computation domain of the reactor with 45-degree baffles

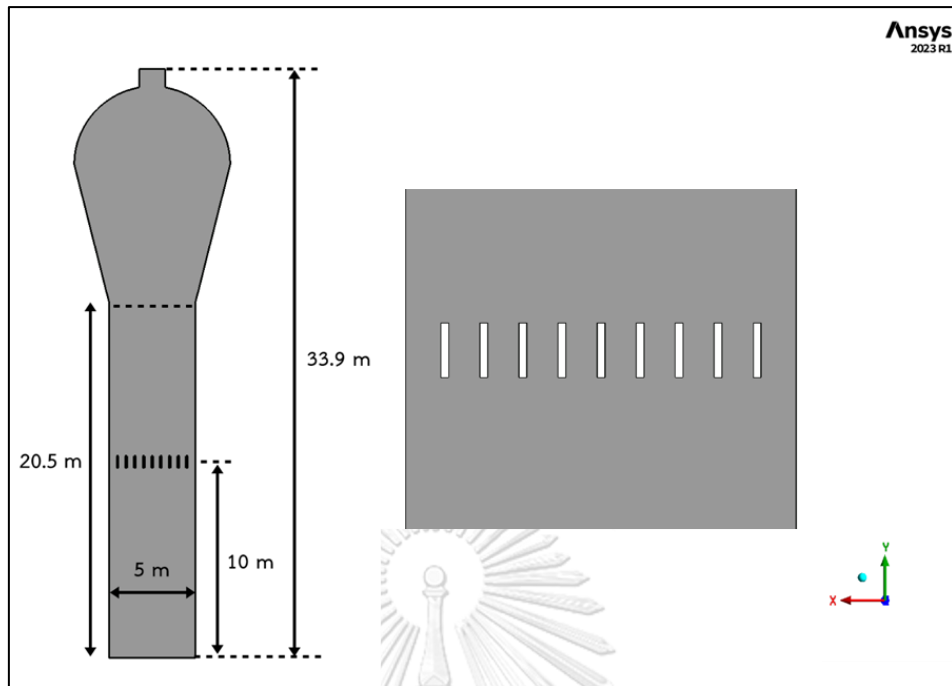


Figure 3.10 Computation domain of the reactor with 90-degree baffles

Results and discussion

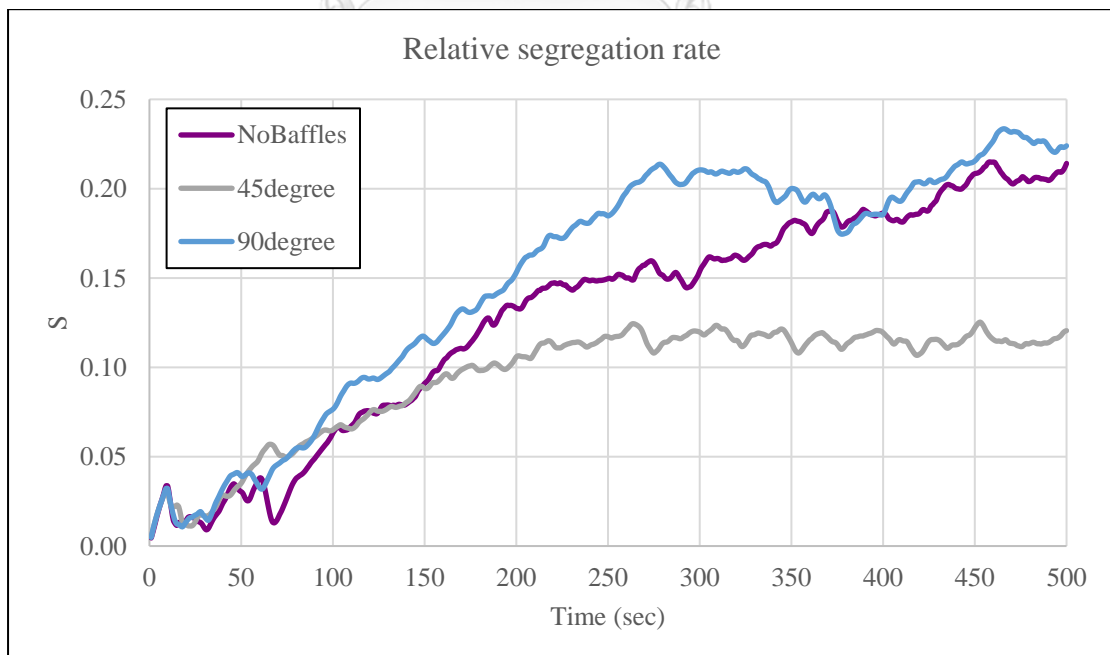


Figure 3.11 Relative segregation rate of the reactor without baffles, reactor with 45-degree and 90-degree baffles.

The Figure 3.11 showed the relative segregation rates of three cases: no baffles, 45-degree baffles and 90-degree baffles. The insertion of 90-degree baffles at the middle of the reaction zone had no significant effect on solid behavior, moreover; the relative segregation rate was close to that observed in the no baffles case. On the other hand, the insertion of 45-degree baffles resulted in a significant decrease in the relative segregation rate and led to better mixing of the particles in the system.

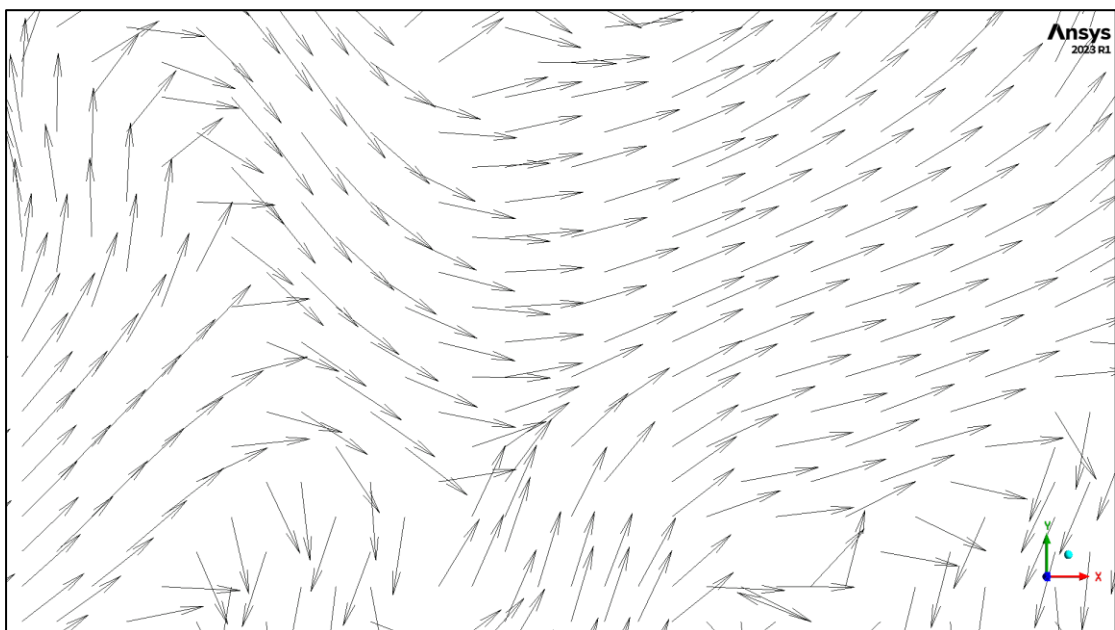


Figure 3.12 Solid velocity vector within the no-baffles reactor

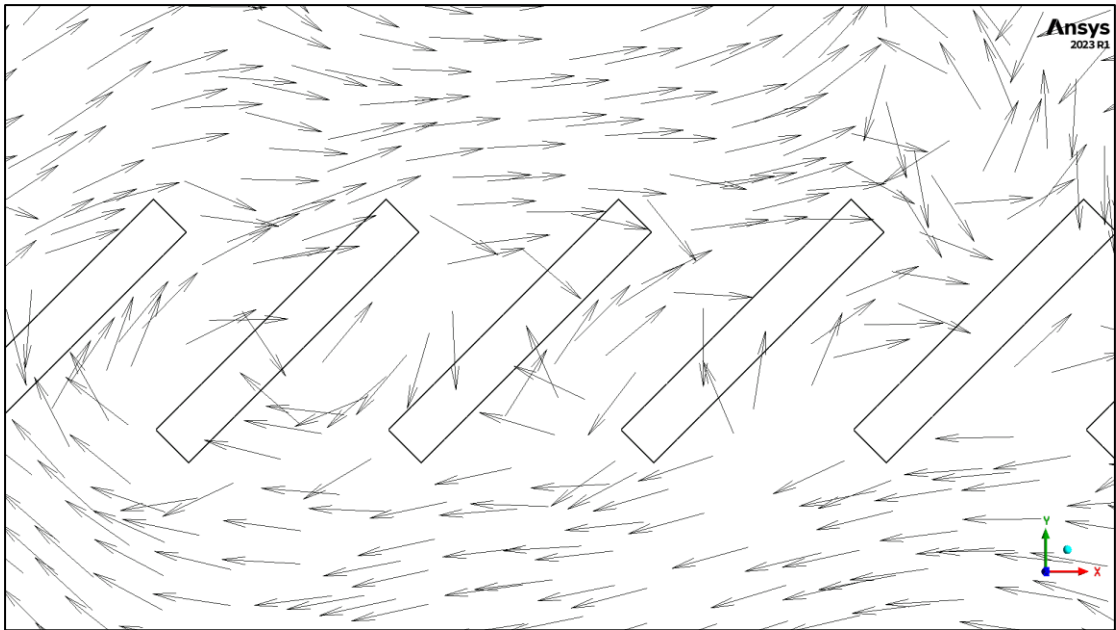


Figure 3.13 Solid velocity vector within the 45-degree baffles reactor

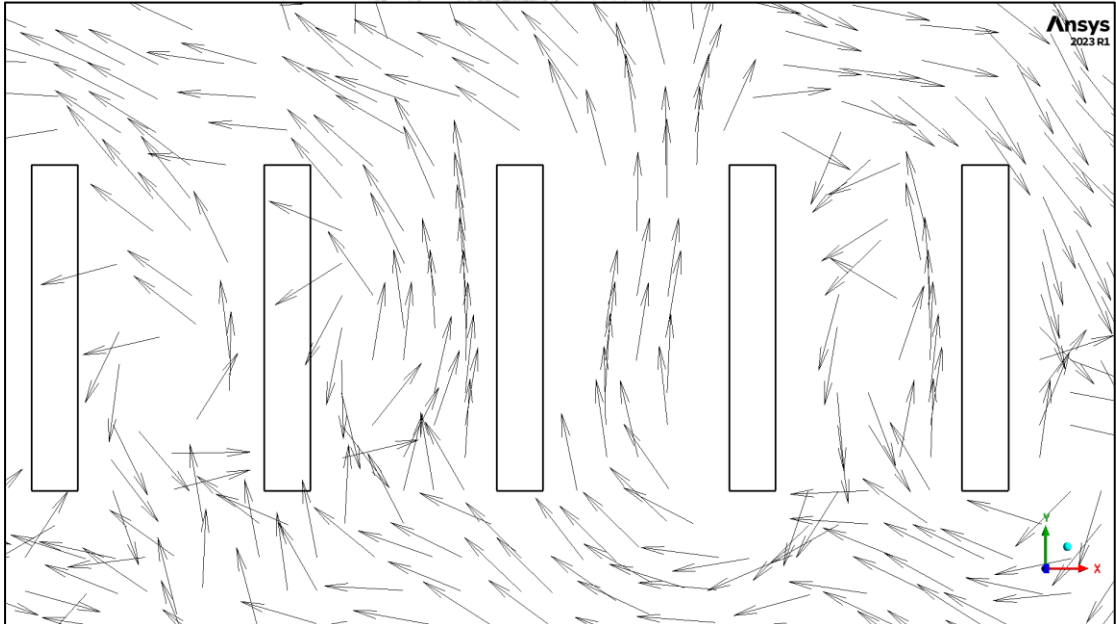


Figure 3.14 Solid velocity vector within the 90-degree baffles reactor

To study the behavior of the solid particle in the system, solid velocity vector was considered. Figure 3.12-3.14 illustrates the velocity vectors of the smallest particles for three cases: no baffles, 45-degree baffles and 90-degree baffles. The results show that solids in a system without baffles and with 90-degree baffles could move freely upward to the top of the bed. However, in the system with 45-degree baffles, the movement of solids through the baffles was hindered due to the angled structure of the baffles. The flow pattern in this case becomes more complex, introducing additional resistance that makes it difficult for solids to pass through the baffles. Most particles were blocked and forced to move horizontally parallel to the baffles' layout. Additionally, some particles collided with the baffles and were redirected towards the baffles' wall, eventually passing through the baffles' gap and entering the reaction zone above the baffles. Both behaviors of particles led to decreasing velocity in y direction through the baffles that are illustrated in Figure 3.15.

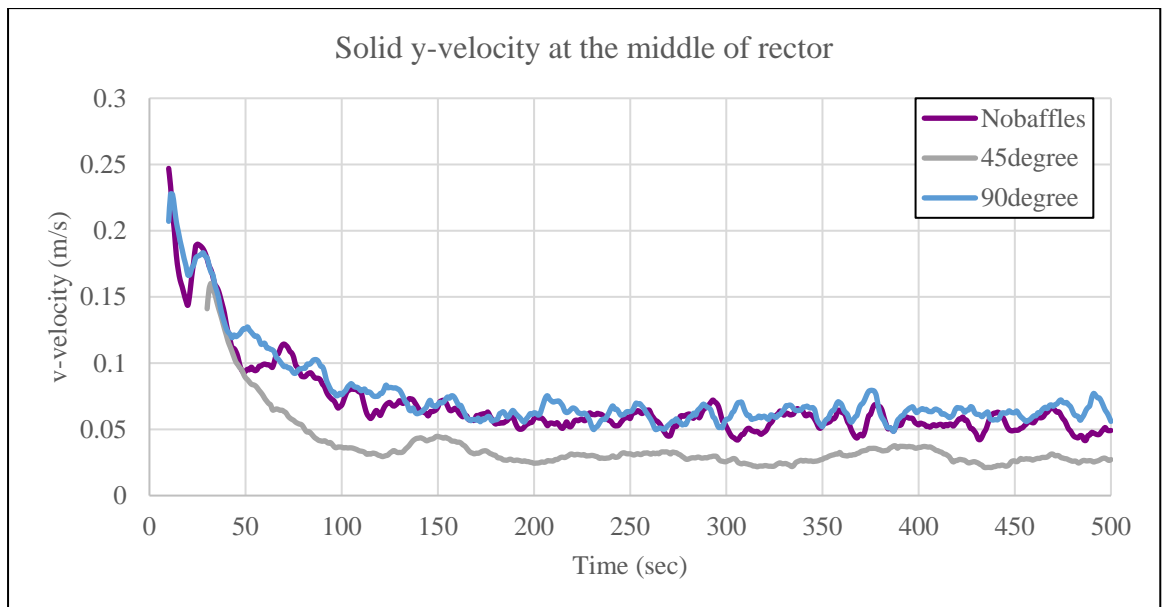


Figure 3.15 Solid y-velocity at the middle of reactor comparison

To further investigate the impact of 45-degree baffles on the system, it would be beneficial to analyze the overall solid volume fraction along the bed height, as illustrated in Figure 3.16.

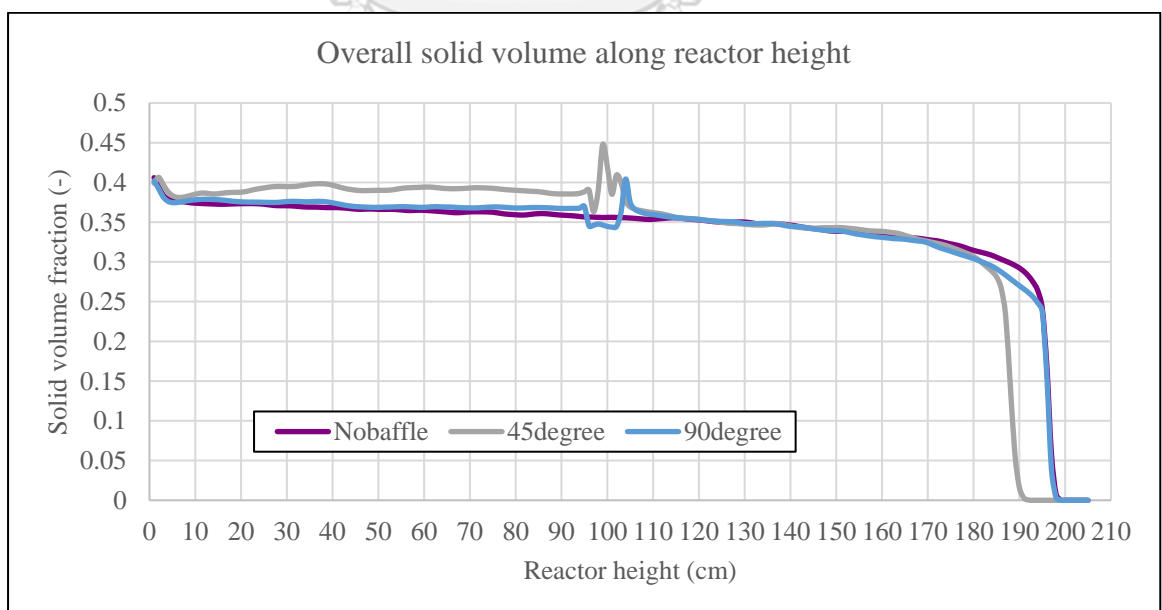


Figure 3.16 Overall solid volume fraction along reactor height comparison

The results from Figure 3.16 show that the solid volume fraction under the 45-degree baffle was the highest, which could be attributed to the solid hindering effect of the baffles. However, the solid volume fraction over the baffles was similar to the other cases. Since the initial mass of the solid was equal in all cases, which resulted in a lower solid bed height for the 45-degree baffle case.

When consider the volume fraction of the smallest particles separated from the largest particles, the effect of 45-degree baffles on segregation behavior would be observed clearly. As shown in the Figures 3.17 - 3.20, the smallest particles volume fraction increased at the bottom of the bed while bed height and volume fraction at the top of the bed decreased. On the other hand, the largest particle volume fraction decreased at the bottom of the bed. However, at the top of the bed, the largest particles volume fraction was not significantly different from the other case.

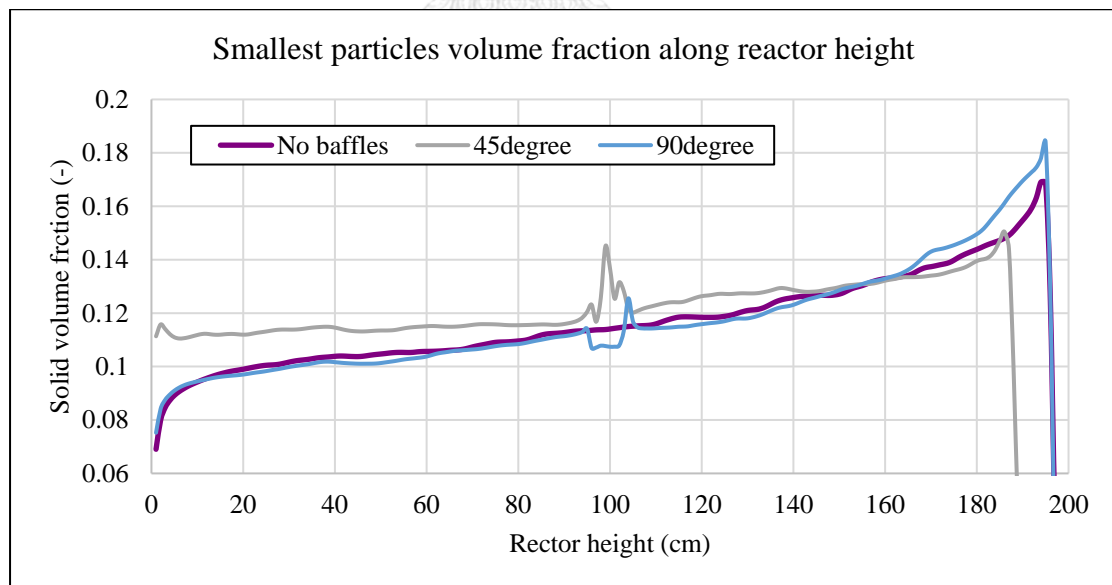


Figure 3.17 Smallest particles volume fraction along reactor height comparison

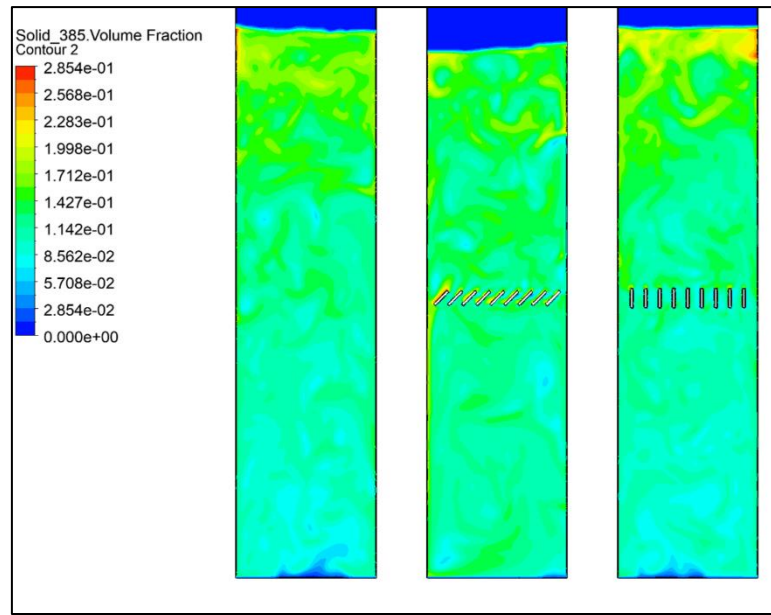


Figure 3.18 Contour of smallest particles volume fraction comparison

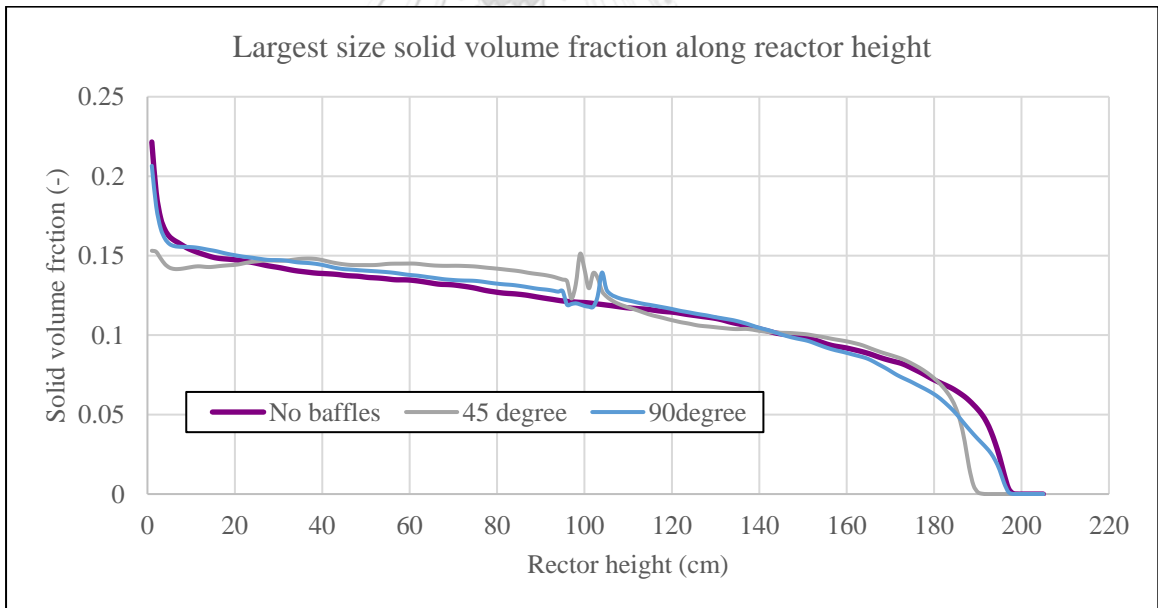


Figure 3.19 Largest particles volume fraction along reactor height comparison

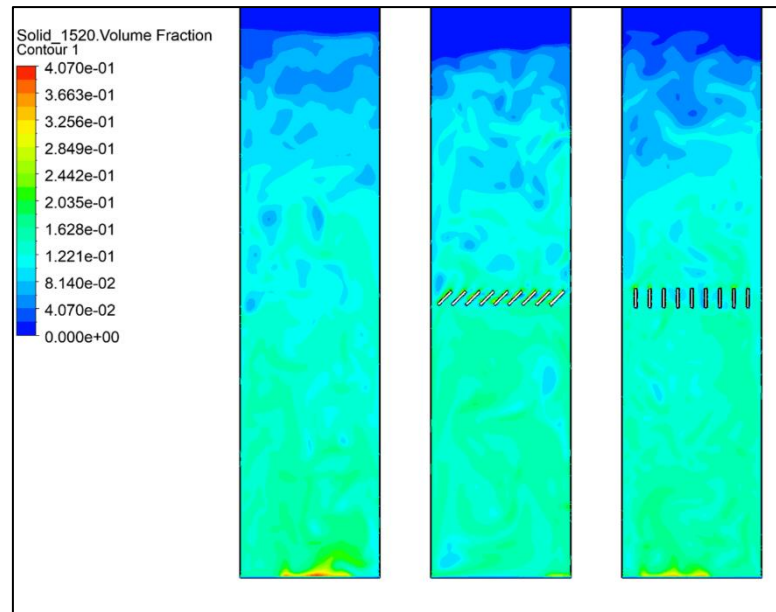


Figure 3.20 Contour of largest particles volume fraction comparison

Effect of baffles angle

In addition to the previous section, the effects of 30-degree and 60-degree baffles on the segregation of solid particles within the reactor were also studied. These baffles were inserted at the same location and using the same dimensions as previously mentioned, and their impact on fluid hydrodynamics was evaluated using the validated model. The results of these additional investigations were analyzed and compared with those from the previous section to provide a more comprehensive understanding of the system's behavior. The computational domains were shown in Figures 3.21 and 3.22 and relative segregation rate with difference angle was shown in Figure 3.23.

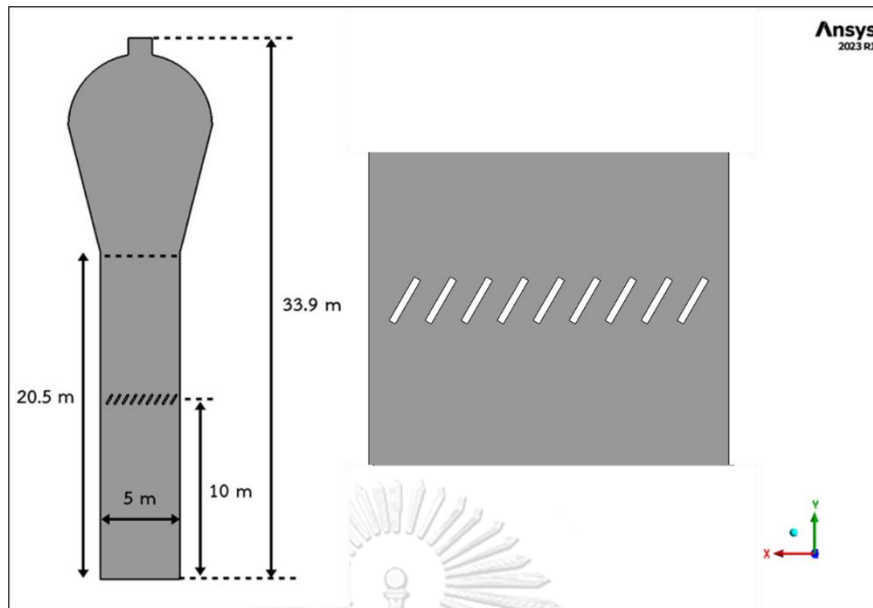


Figure 3.21 Computation domain of the reactor with 30-degree baffles

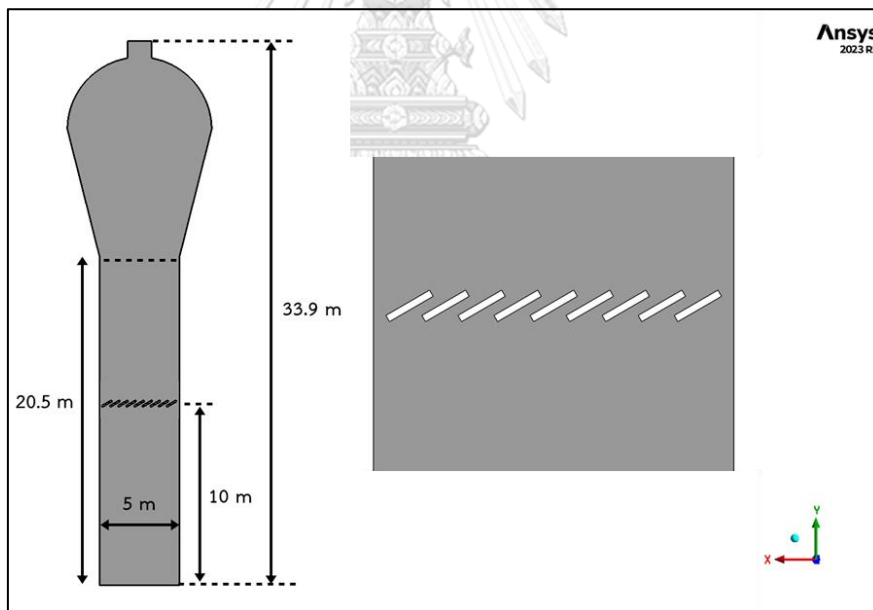


Figure 3.22 Computation domain of the reactor with 60-degree baffles

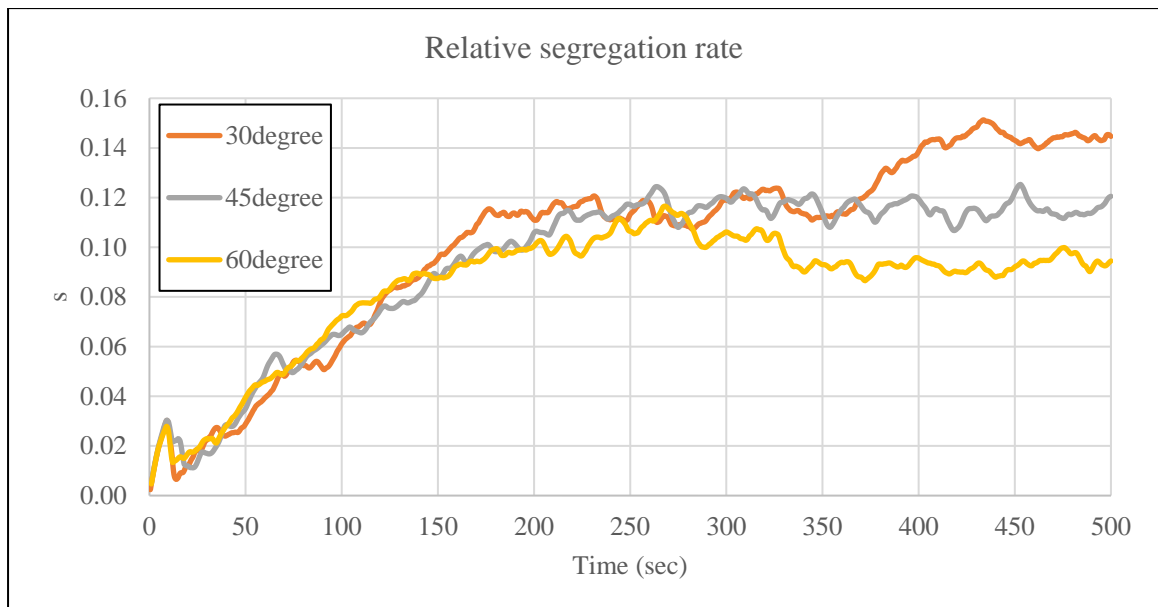


Figure 3.23 Relative segregation rate of the reactor with difference baffles angle

According to the relative segregation rate illustrated in Figure 3.23, it can be observed that the 60-degree baffles resulted in the lowest relative segregation rate, while the 45-degree and 30-degree baffles resulted in higher relative segregation rates, in that order. The smallest particle volume fraction along reactor height and contour of smallest particle volume fraction were shown in the figure 3.24 and 3.25, respectively. From both figures, it was found that at the top of the bed smallest particle volume fraction decreased while angle of the baffles was increased. Moreover, particle volume fraction above the 60-degree baffles was more uniform than other case.

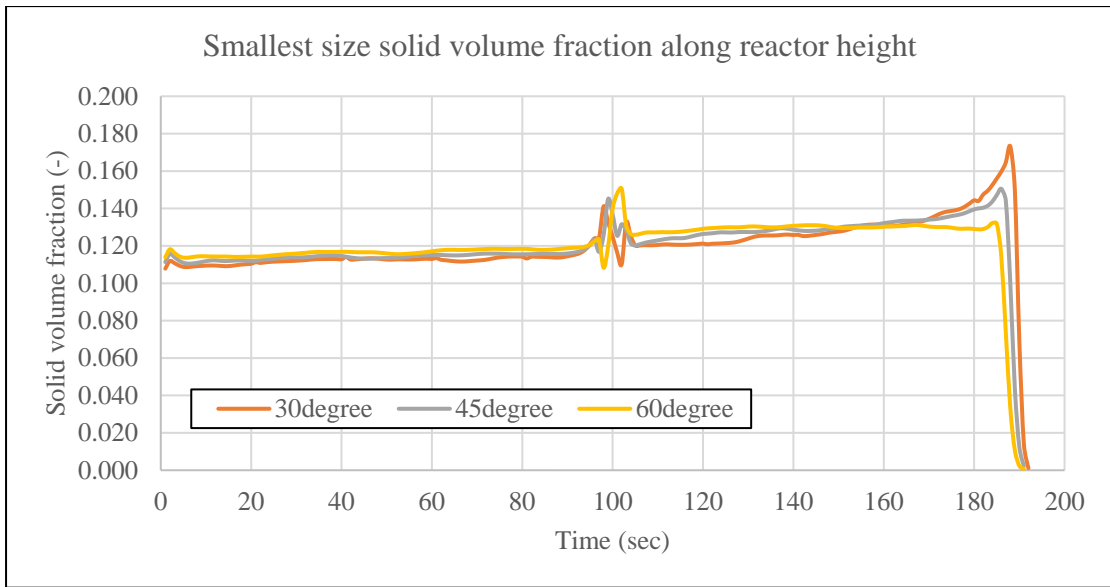


Figure 3.24 Smallest particles volume fraction along reactor height comparison

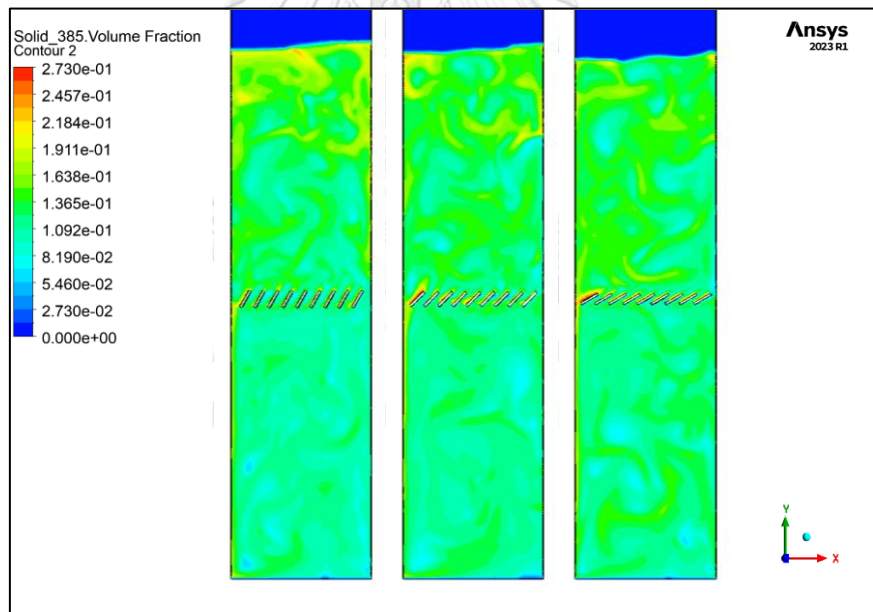


Figure 3.25 Contour of the smallest particles volume fraction comparison

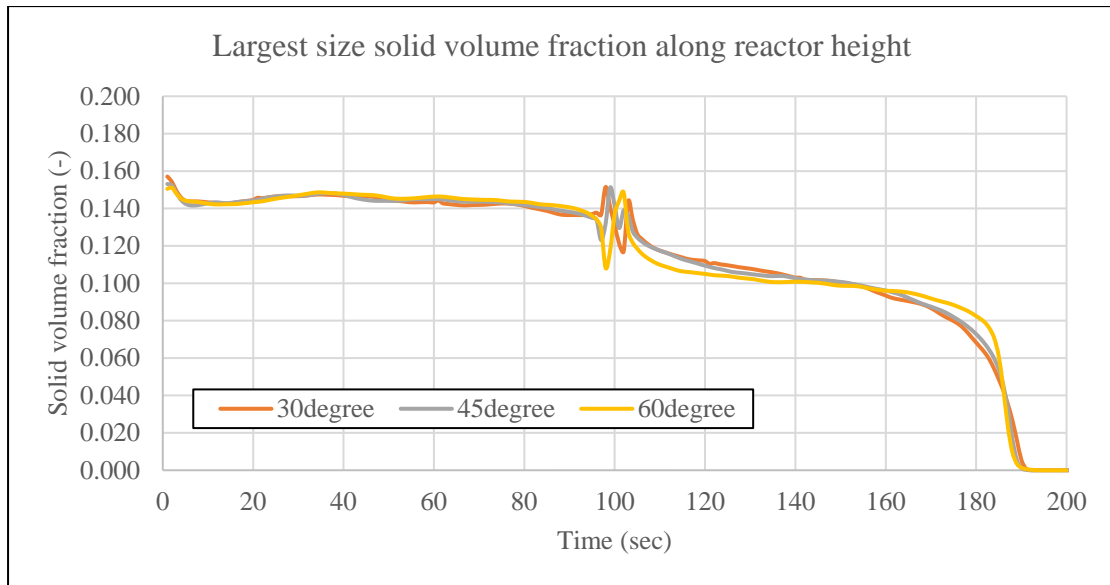


Figure 3.26 Largest particles volume fraction along reactor height comparison

Effect of stage number and arrangement

To investigate the effect of stage number and its arrangement on the segregation of solid particles in the reactor, one baffle stage consisting of 9 baffles with a 45-degree angle was utilized. A total of 1 and 2 stages were employed, and the stage arrangements comprised three types. The first arrangement, referred to as the "above arrangement" and illustrated in Figure 3.27(a), involved inserting an additional baffle stage above the base stage at a height of 15 meters from the bottom of the reactor. The second arrangement, defined as the "below arrangement" and shown in Figure 3.27(b), entailed inserting an additional baffle stage below the base stage at a height of 5 meters from the bottom of the reactor. The third arrangement, illustrated in Figure 3.27(c) and known as the "expand arrangement," entailed the removal of the base stage from the system, while 2 additional stages were inserted above and below the base stage position.

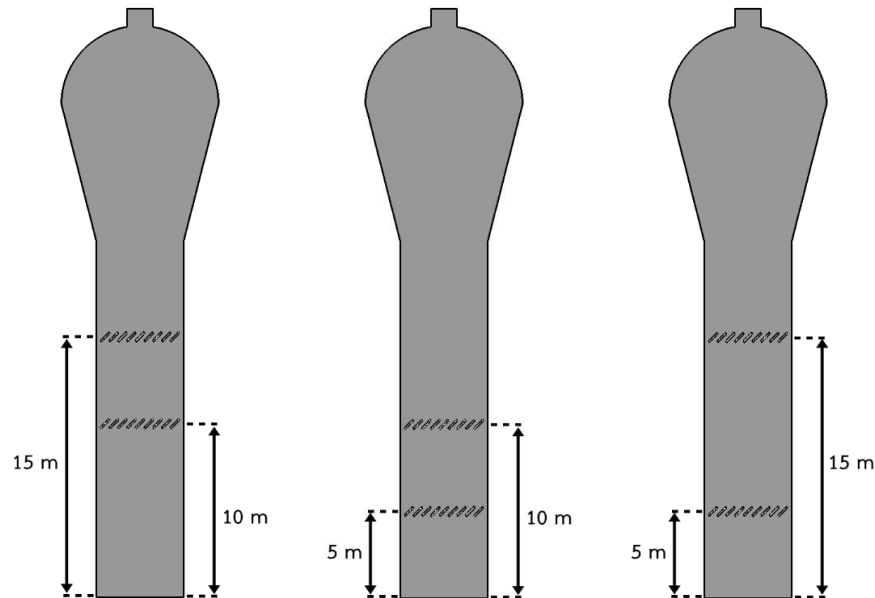


Figure 3.27 Computation domain of the reactor of difference case (a) above case (b) below case and (c) expand case.

Effect of stage number

The segregation behavior in the system was confirmed to be reducible by the additional baffle stage through the relative segregation rate chart in Figure 3.28. It was observed that the relative segregation rate of the single stage was higher than that of the two-stage baffles with any arrangement. Furthermore, the lowest relative segregation rate was observed in the above arrangement, followed by the expand and below arrangements, respectively. To facilitate clear observation, the 45-degree baffles case was considered a single-stage baffle and compared to the above case, which was a two-stage baffle.

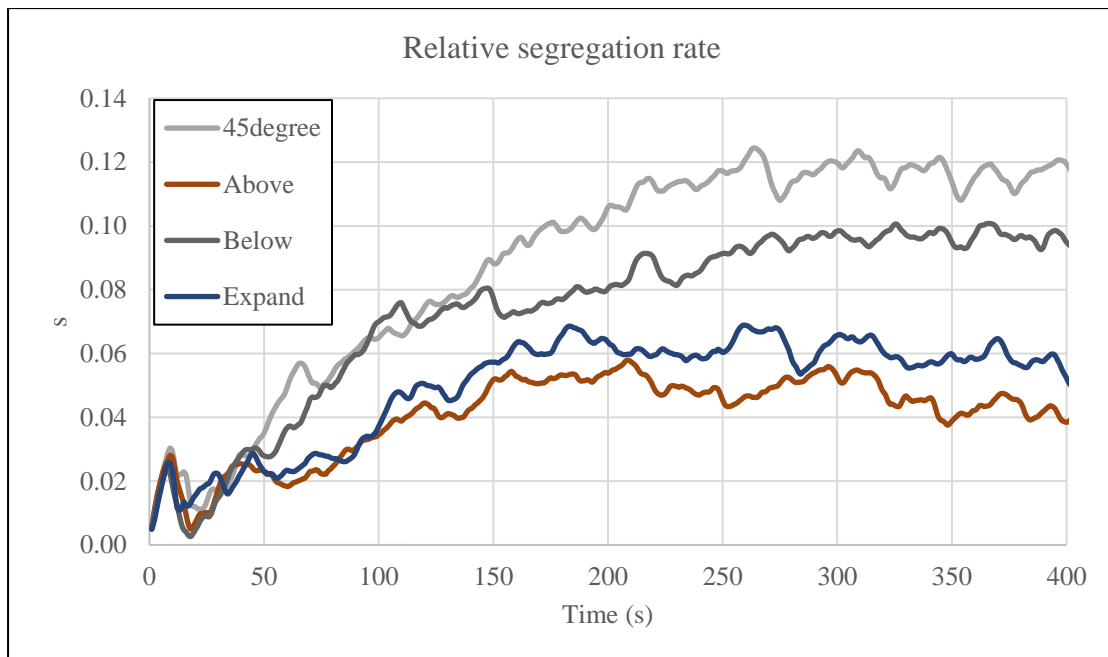


Figure 3.28 Relative segregation rate of the reactor with difference arrangement.

Based on the results shown in Figure 3.29, the single-stage baffle exhibited a lower volume fraction of the smallest particles below the first stage compared to the above arrangement, while both cases showed a similar trend. However, when a second stage was added above the base stage, it hindered particle flow and caused swirling and accumulation between the first and second stages, as shown in Figure 3.30, which led to a higher volume fraction.

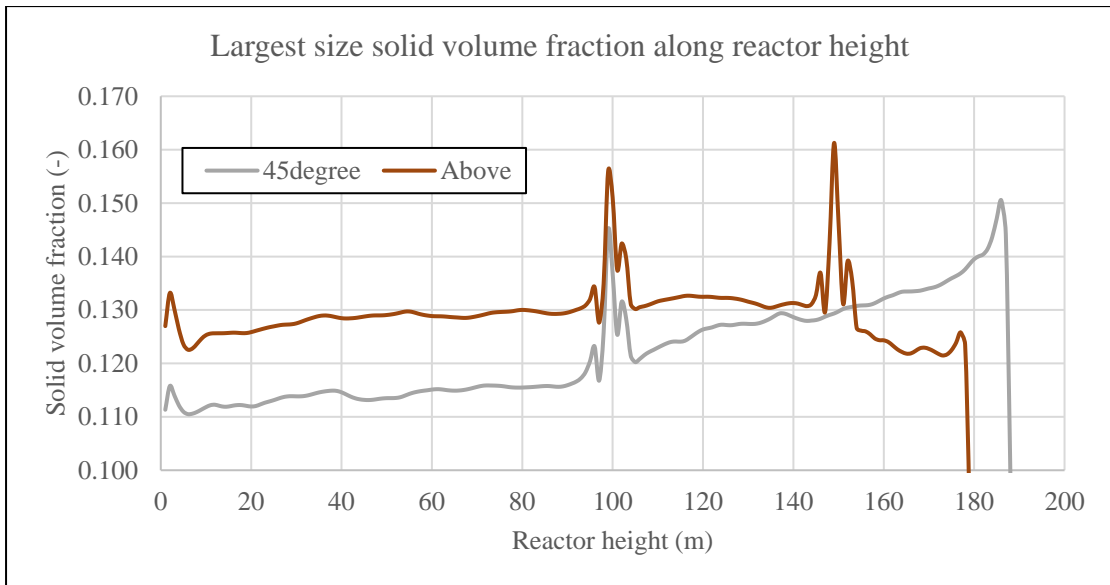


Figure 3.29 Relative segregation rate of the reactor with difference arrangement.

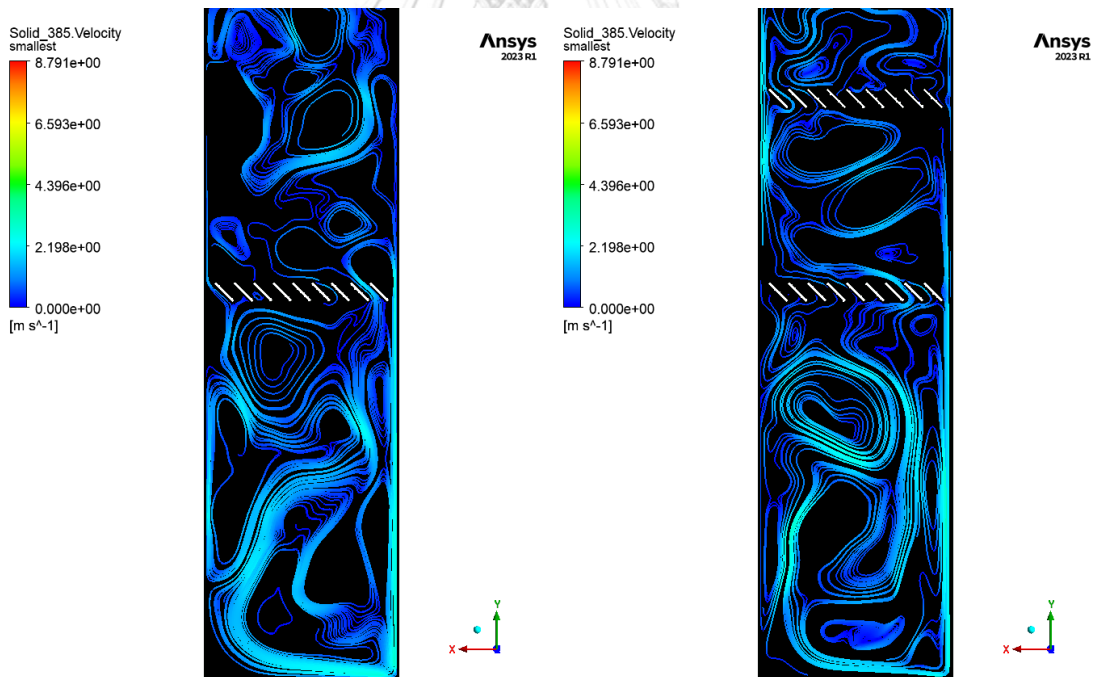
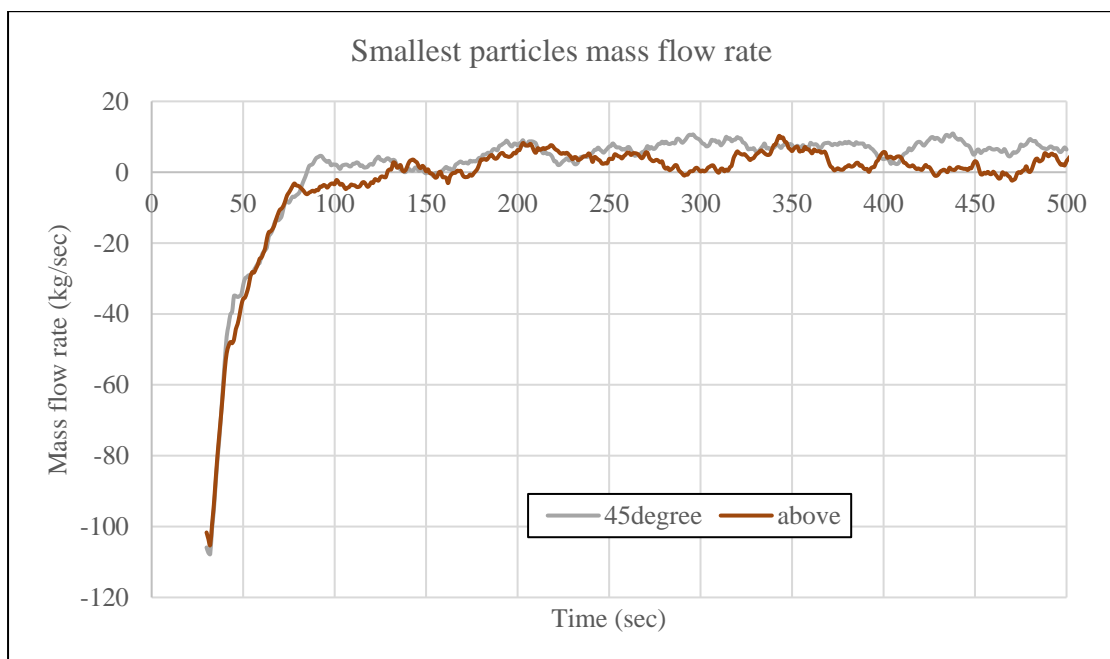


Figure 3.30 Smallest particle streamline of single stage and 2 stages case

The swirling particles also hindered particle flow, resulting in a lower flow rate of the smallest particles through the first stage, as illustrated in Figure 3.31. This caused a higher volume fraction of the smallest particles below the first stage. Furthermore, the volume fraction of the smallest particles above the second stage was lower than in the other zones and in the single-stage case, due to the second stage and the hindrance caused by the swirling particles.



CHULALONGKORN UNIVERSITY

Figure 3.31 Smallest particle mass flow rate through the first stage

Similar to its effect on the behavior of the smallest particles, the addition of a second stage baffle also caused swirling of the largest particles, as shown in Figure 3.32. This led to a higher volume fraction of the largest particles, as illustrated in Figure 3.33. Consequently, the presence of the second stage hindered particle flow, resulting in a lower volume fraction of the smallest particles and a higher volume

fraction of the largest particles at the top of the bed, which in turn led to a reduction in the segregation rate of the system.

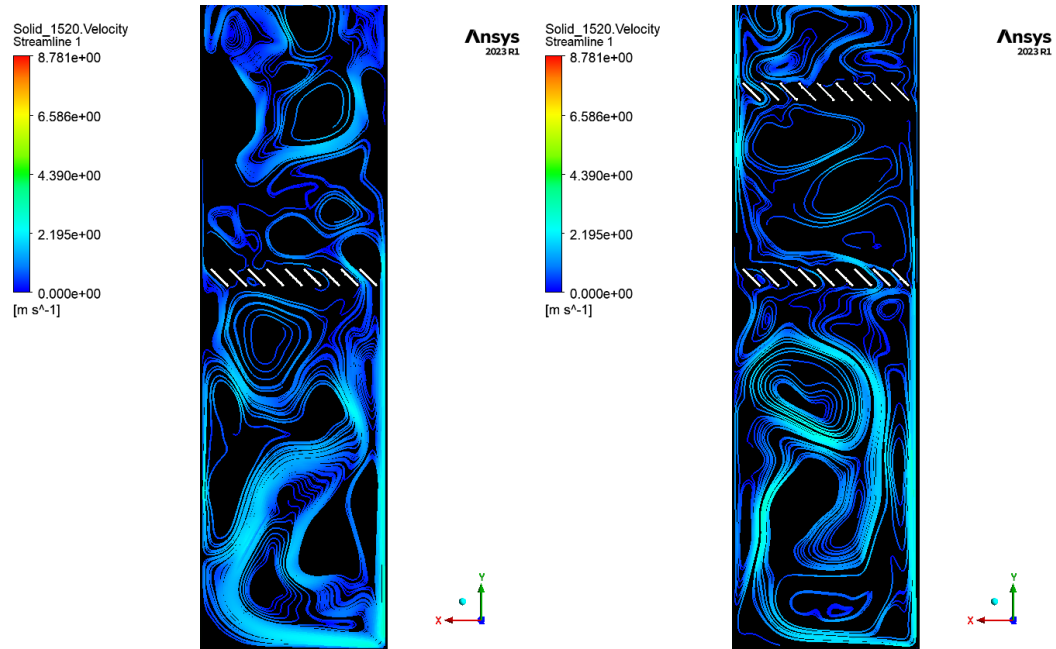


Figure 3.32 Smallest particle streamline of single stage and 2 stages cases.

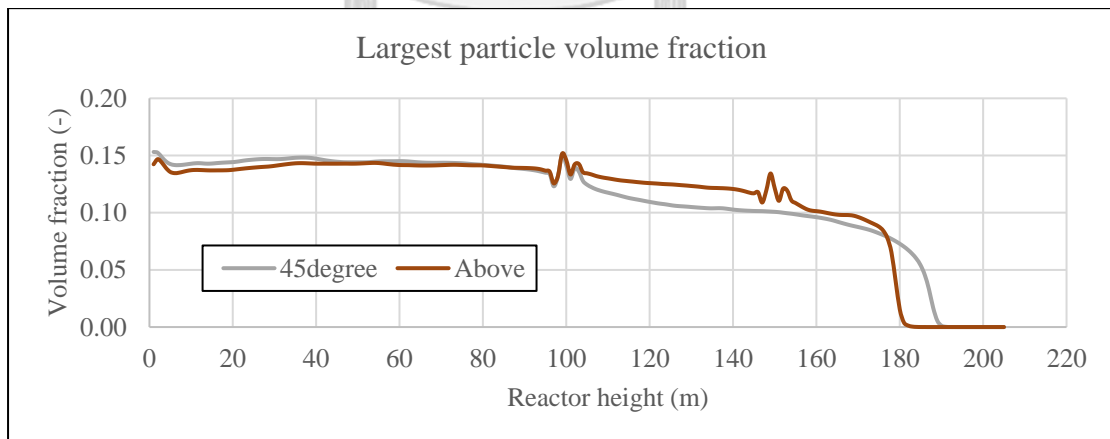


Figure 3.33 Largest particles volume fraction along reactor height comparison

Effect of stage arrangement

From the relative segregation rate chart in Figure 3.28, it can conclude that segregation behavior in the system was reduced due to inserting second baffles stage. Inserting second stage baffles affected both smallest and largest particle size, resulted in difference smallest and largest particle volume fraction in the system as show in the Figures 3.34 and 3.35, respectively.

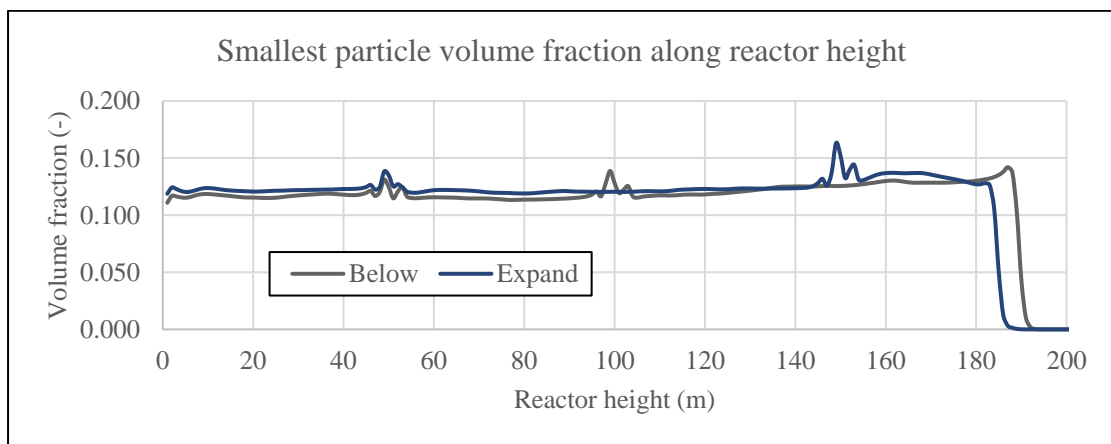


Figure 3.34 Smallest particles volume fraction along reactor height comparison

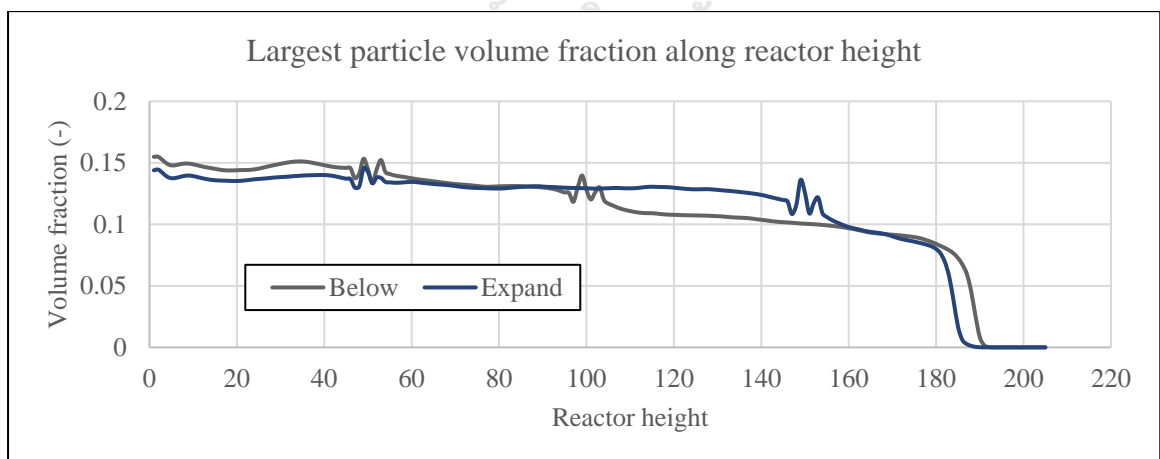


Figure 3.35 Smallest particles volume fraction along reactor height comparison

In order to investigate the effect of stage arrangement on segregation behavior in the fluidized bed reactor, a comparison was made between the 'below' and 'expand' cases. Both cases had the same first stage located below the base stage, but the second stage was allocated differently in each case. The first baffle stage hindered the particles movement and caused swirling of the largest particles under the stage that show in the Figure 3.36.

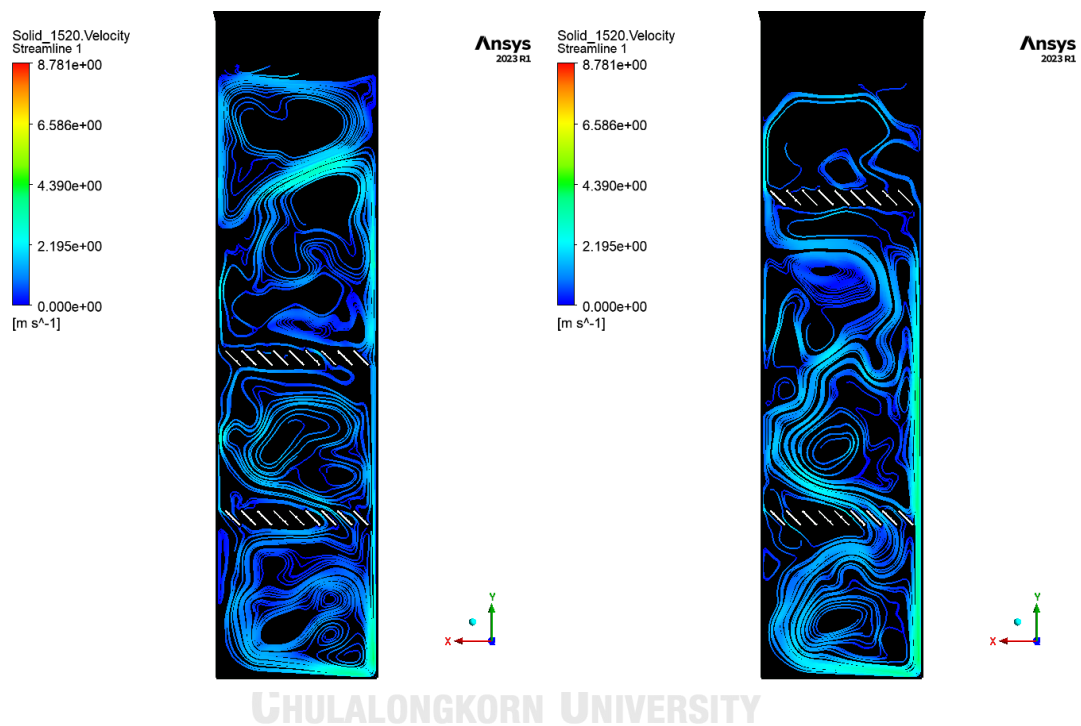


Figure 3.36 Smallest particle streamline of below and expand case

In the 'below' case, the second stage was located closer to the first stage than in the 'expand' case. This proximity caused the largest particles to accumulate and swirl in most of area between the two stages, impeding their movement through the first stage. As a result, the mass flow rate of the largest particles was reduced, as seen in Figure 3.37. This swirling behavior led to a higher volume fraction of the largest particles under the first stage.

In contrast, in the 'expand' case with a larger area between the first and second baffles, particles could move upward more easily, resulting in a more uniform particle volume fraction in this zone. However, the second baffle stage still caused swirling and hindered particle movement, resulting in a lower particle volume fraction at the top of the bed.

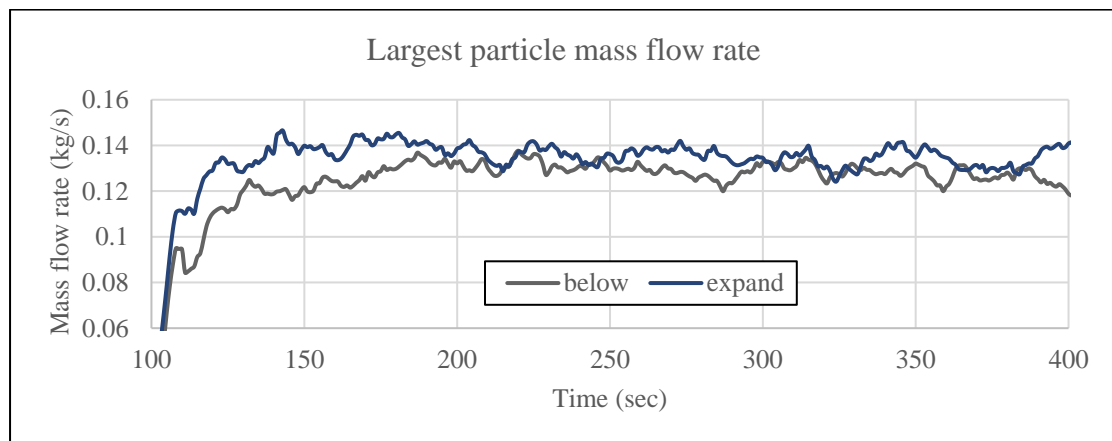


Figure 3.37 Largest particle mass flow rate through the first stage

In the case of the smallest particles, Figure 3.38 displays the particle volume fraction along the reactor height. Due to the nature of the smallest particles, they tend to migrate towards the top of the bed when segregation occurs. The insertion of baffles may reduce this behavior by hindering the particles and decreasing their accumulation at the top of the bed. Comparing the 'below' and 'expand' cases, the first baffle stage caused particle hindering and resulted in a high particle volume fraction, which was in line with the behavior of the largest particles.

However, segregation behavior of the smallest particles could be observed when they flowed through the second stage in the 'below' case, which behaves similarly to a single stage baffle. In contrast, in the 'expand' case, the smallest

particles accumulated above the second stage. Similar to the largest particles, the smaller particles were able to move more easily in a larger area between the first and second baffles, resulting in a higher y-axis velocity and consequently a higher mass flow rate through the second stage, as illustrated in Figure 3.38.

Therefore, due to the more uniform particle volume fraction distribution resulting from the appropriate second stage arrangement, the 'expand' case exhibited a lower relative segregation rate, indicating a more significant reduction in segregation behavior than the 'below' case.

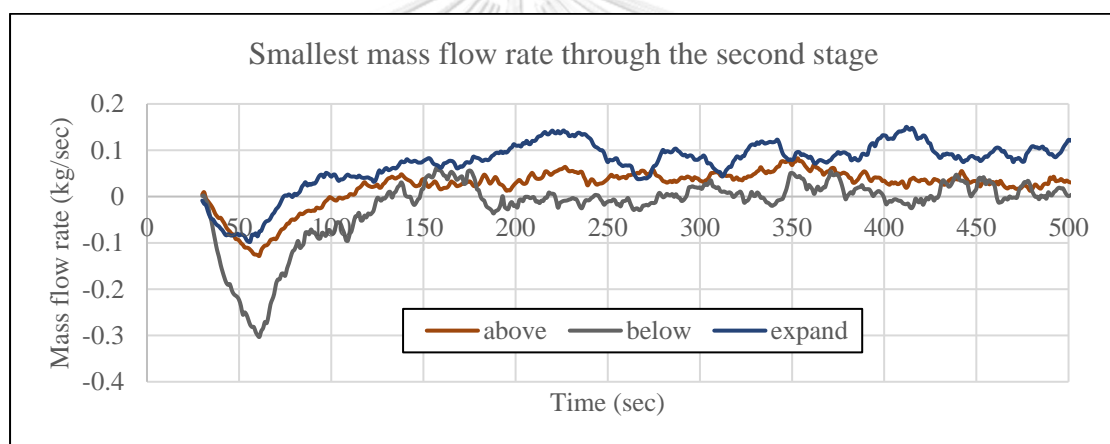


Figure 3.38 Smallest particle mass flow rate through the second stage

The 'above' case was found to be the most effective arrangement in this study. In this case, the first stage was inserted at the base stage while the second stage was located at the same height level as the 'expand' case, where the first stage was added below the base stage.

To examine the impact of stage arrangement, the behavior of the smallest and largest particles was analyzed. The largest particles tended to accumulate at the

bottom of the reactor, and their y-velocity increased along the reactor height until they were affected by the first stage, after which it decreased similarly to the 'expand' case. Both behaviors resulted in a more uniform distribution of the largest particle volume under the first stage. However, the narrow gap between the first and second stages hindered particle movement, resulting in a lower volume fraction of the largest particles in the gap and above the second stage, and a decrease in bed height. Conversely, the volume fraction above the second stage was higher than in the 'expand' case.

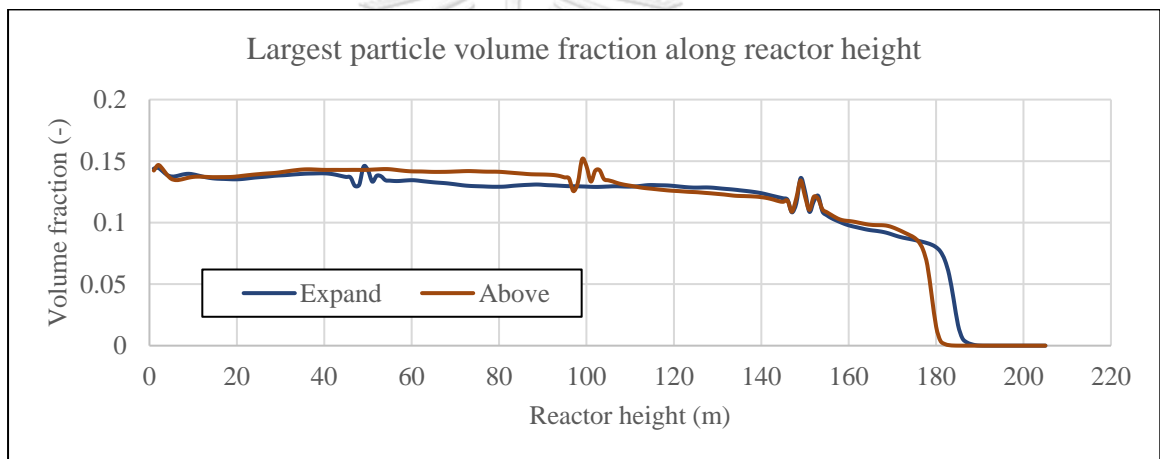


Figure 3.39 Largest particle volume fraction along reactor height

For the smallest particles, due to their higher y-axis velocity compared to the largest particles and y-axis velocity increased along the height, the particle volume fraction increased along the height. However, the first stage baffles hindered particle movement and caused swirling under the stage, as shown in Figure 3.41. Moreover, in the 'above' case, the narrow gap between stages caused swirling in the area, resulting in a higher particle volume fraction. However, this behavior was similar to the 'below'

case and resulted in lower particle volume fraction above the second stage due to particle hindering.

Therefore, the appropriate second stage arrangement in the 'above' case led to a more uniform particle volume fraction distribution, a higher largest particle volume fraction and a lower smallest particle volume fraction at the top of the bed, resulting in a lower relative segregation rate and a more significant reduction in segregation behavior than the 'expand' case.

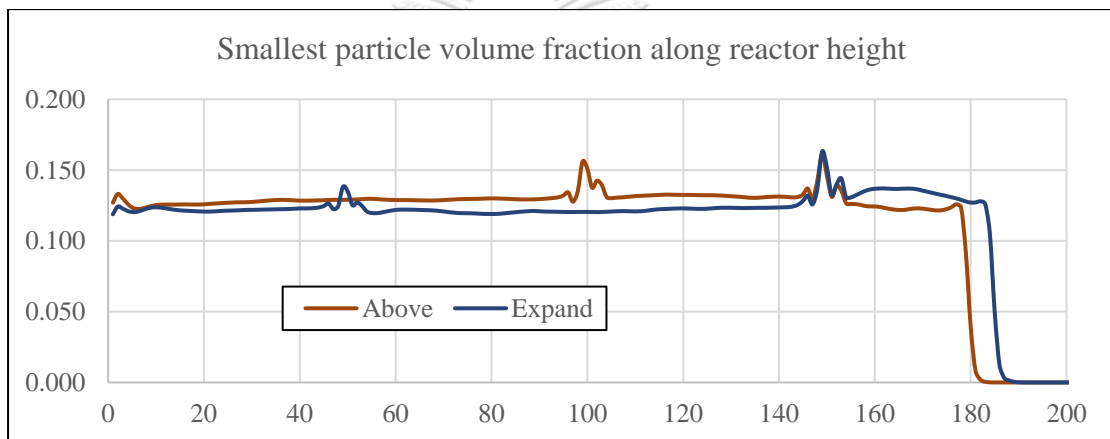


Figure 3.40 Smallest particle volume fraction along reactor height

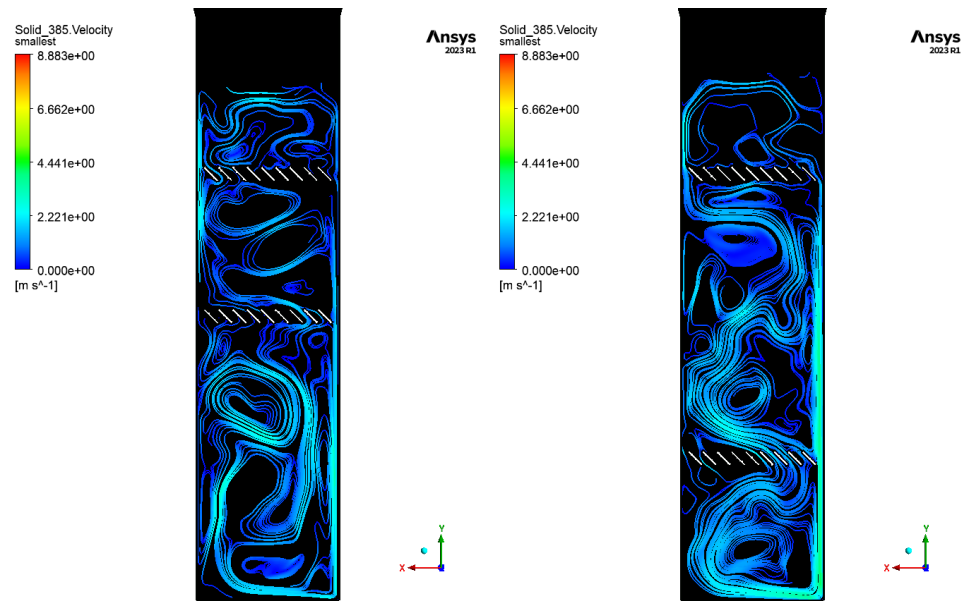


Figure 3.41 Smallest streamline of above and expand case

Effect of baffle number

To investigate the effect of the number of baffles on segregation behavior in the system, four baffles were inserted in the middle of the reaction zone instead of the previous nine, as shown in Figure 3.42. As illustrated in the figure, a lower number of baffles resulted in a higher gap area between them.

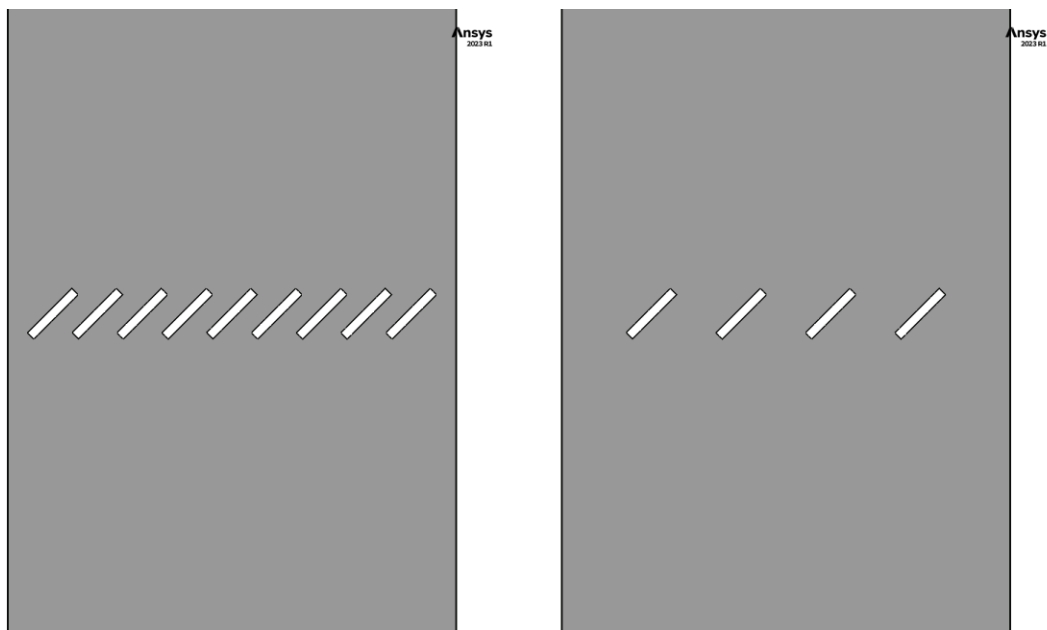


Figure 3.42 Comparison of computational domain between 9 and 4 baffles

Particle velocity vectors, as depicted in Figures 3.43 and 3.44, showed that solid particles were still hindered even with a lower number of baffles, being forced to move horizontally parallel to the baffles' layout. However, compared to the case with nine baffles, there were some particles that circulated and moved downward to the reaction zone below the baffles in the gap between the four baffles, resulting in fluctuation of mass flow rate through the baffles.

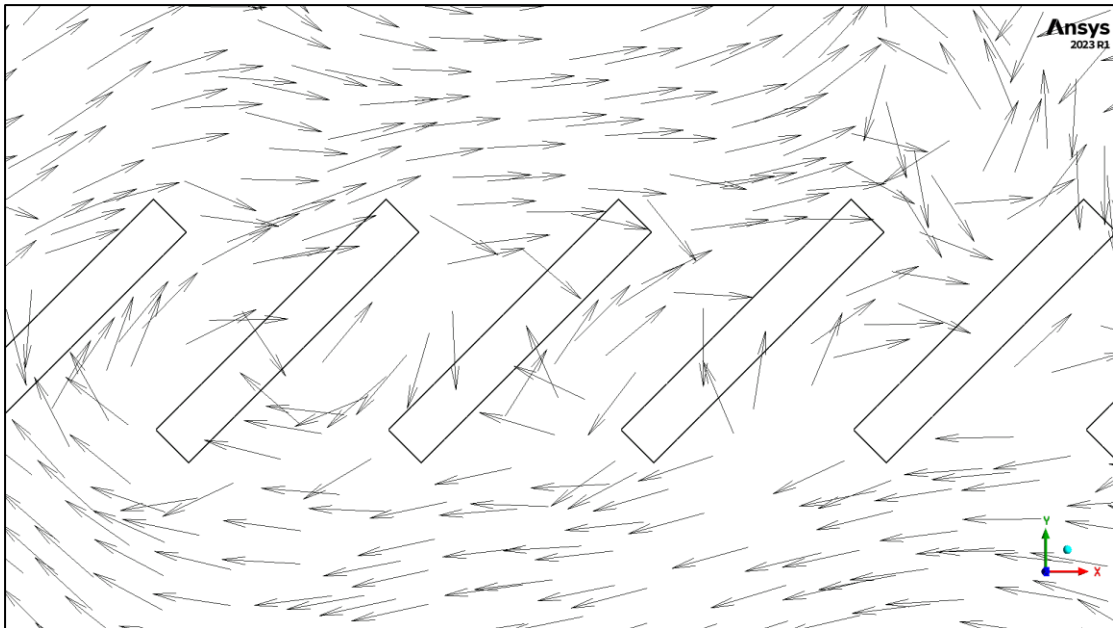


Figure 3.43 Solid velocity vector within the 9 baffles reactor

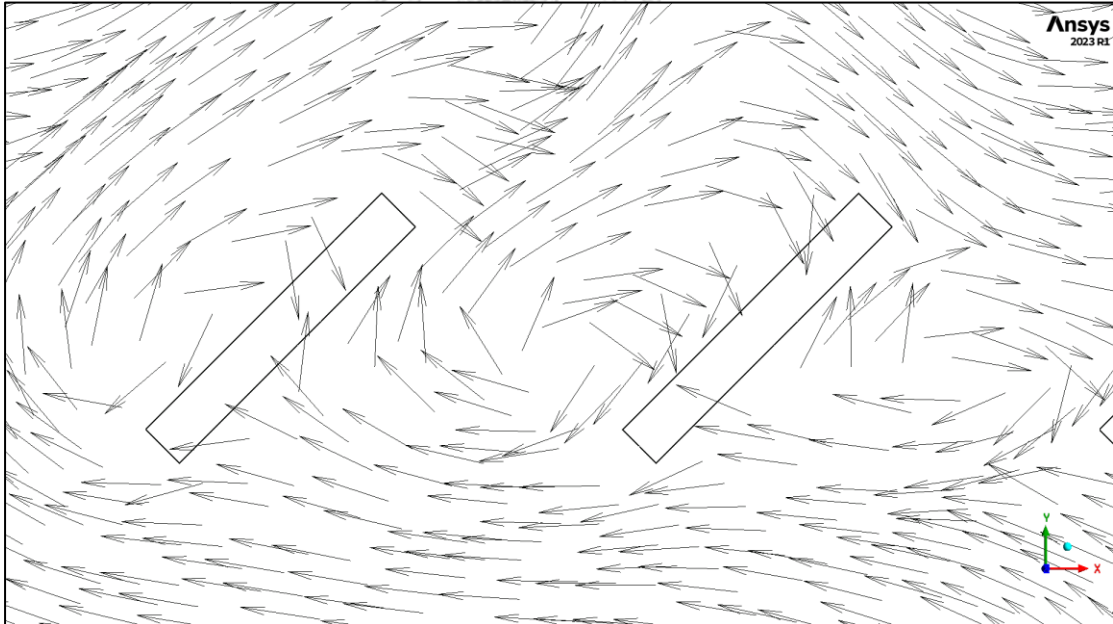


Figure 3.44 Solid velocity vector within the 4 baffles reactor

This behavior was confirmed by calculating the mass flow rate through the area above the baffles, as shown in Figure 3.45, which was located 10.5 meters above the bottom of the reactor. Figures 3.46 and 3.47 show the mass flow rate above the baffles for the smallest and largest particles, respectively, in both cases of 4 and 9 baffles. The figures confirm that decreasing the number of baffles from 9 to 4 resulted in a fluctuation of the mass flow rate above the baffles due to particles behavior in the gap between baffles; moreover, negative mass flow rates indicating the downward movement of particles were observed more frequently.

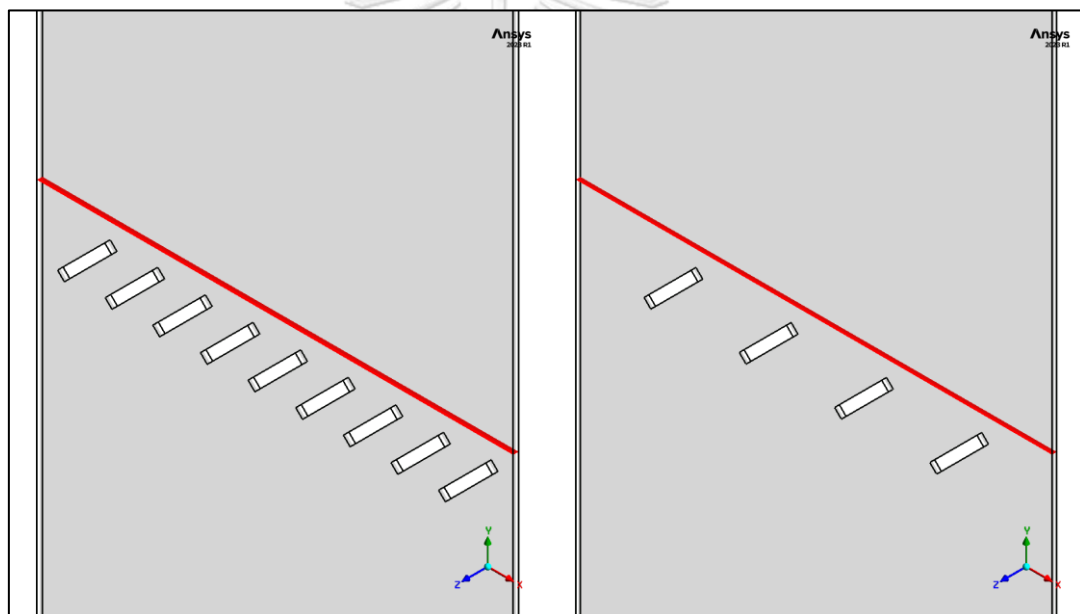


Figure 3.45 Area using to calculate mass flow rate through the baffles

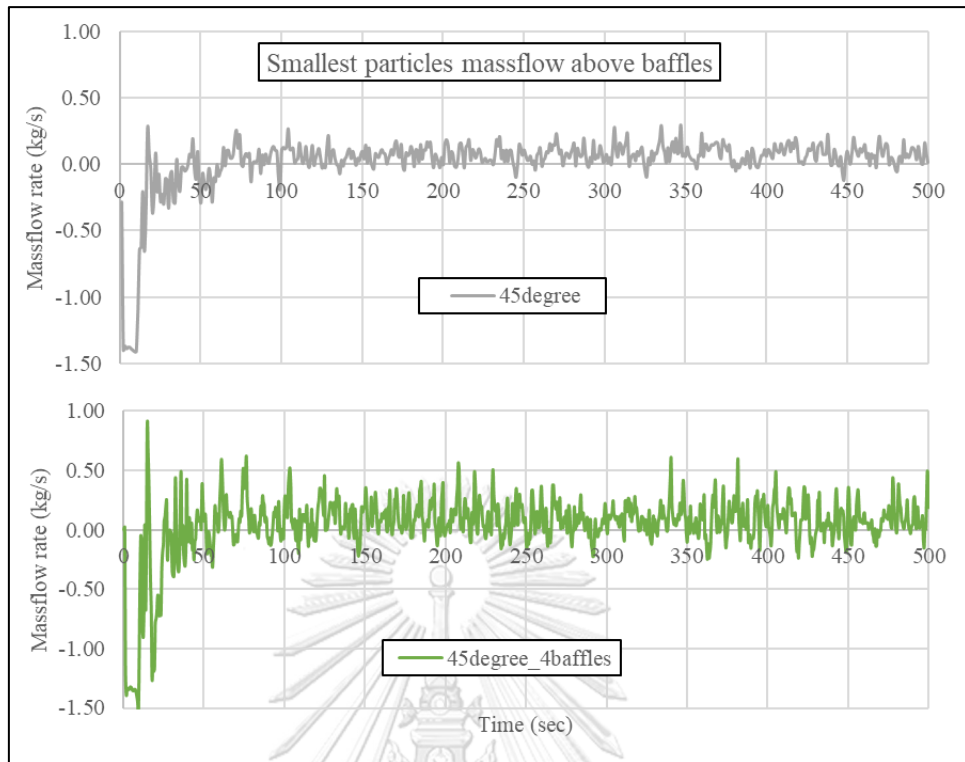


Figure 3.46 Mass flow rate above the baffles for the smallest particles

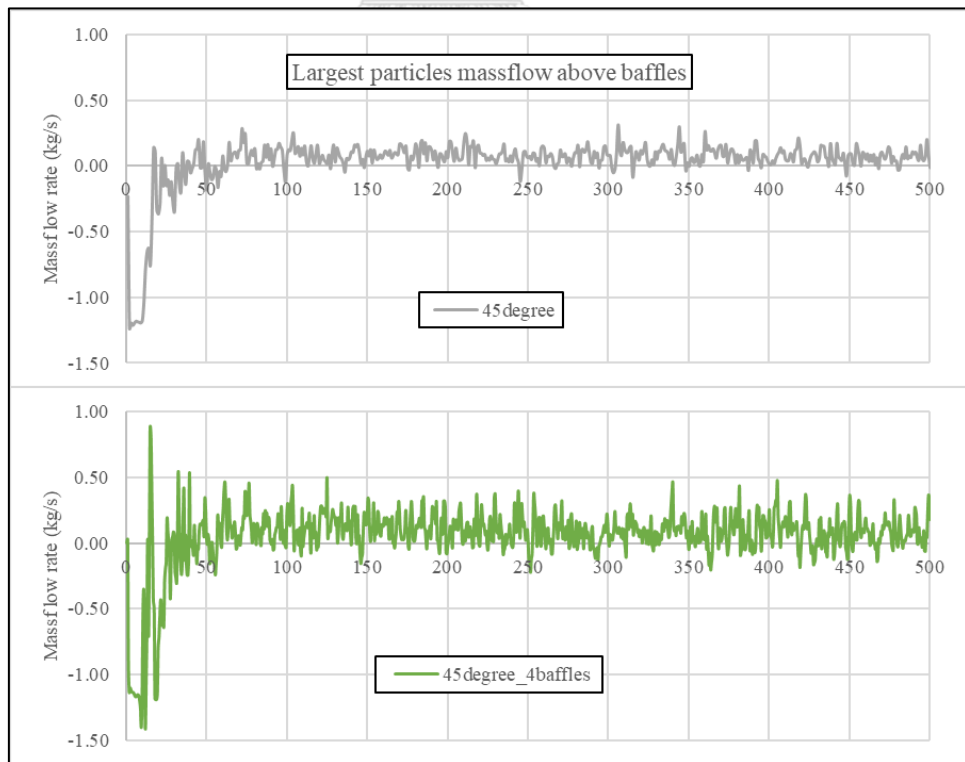


Figure 3.47 Mass flow rate above the baffles for the largest particles

However, Figures 3.48 and 3.49 demonstrate the total mass of smallest and largest particles above the baffles, respectively. Figure 3.48 indicates that the smallest particles accumulated closely together in the upper zone for both cases. In contrast, Figure 3.49 shows the difference in the accumulated mass of the largest particles in the upper zone. Due to the larger gap between baffles, the largest particles could move through the baffles more easily. As a result, in the reactor with 4 baffles, the largest particles accumulated more in the upper zone than in the case with 9 baffles.

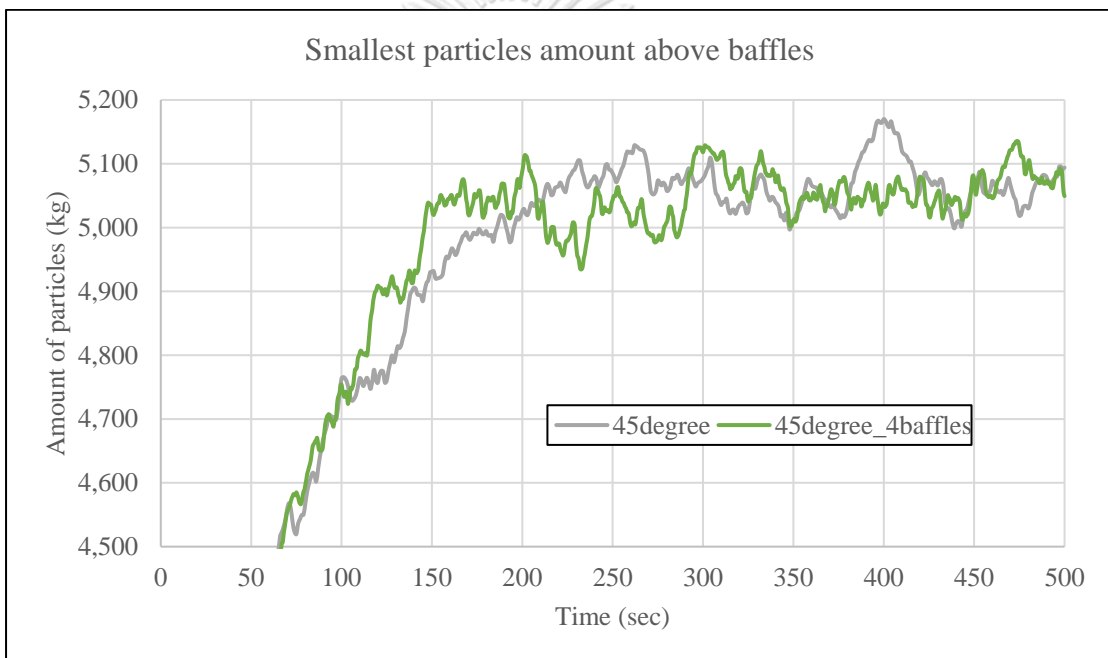


Figure 3.48 Amount of the smallest particle above the baffles

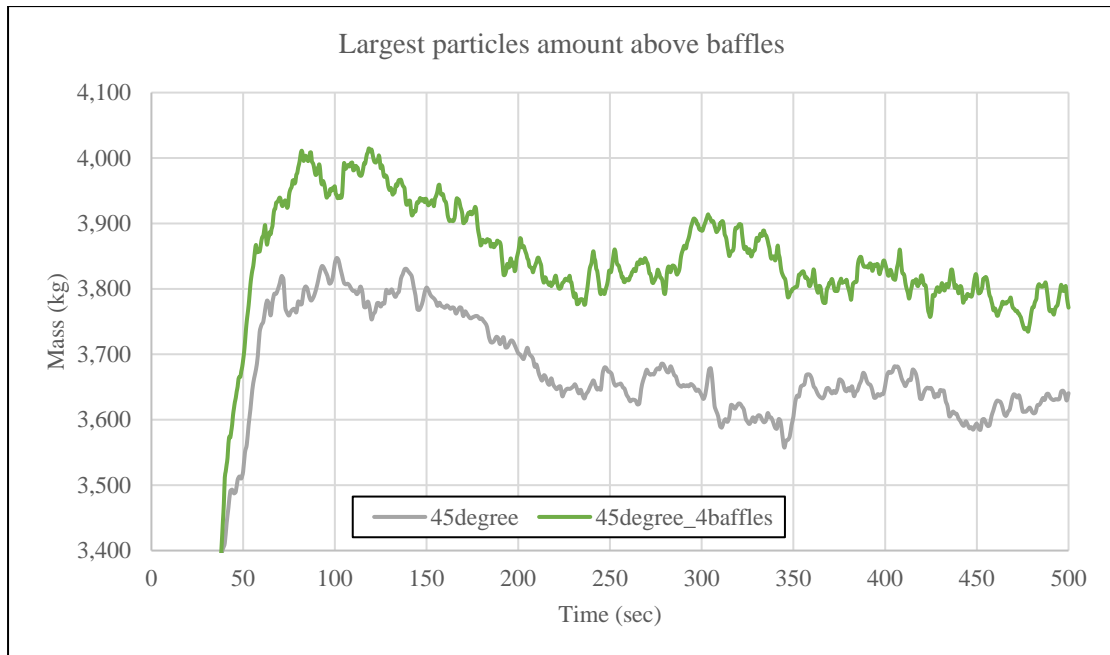


Figure 3.49 Amount of the smallest particle above the baffles

Consistent with the total mass accumulation, the volume fraction of the largest particles above the baffles was higher in the 4-baffles case than in the 9-baffles case, as illustrated in Figure 3.50. However, due to the constant total particle mass in each case, the volume fraction of the largest particles in the lower zone was lower in the 4-baffles case than in the 9-baffles case. Figure 3.51 shows the volume fraction of the smallest particles along the reactor height. Due to the higher accumulation of the largest particles and the close accumulation of the smallest particles, the smallest particle volume fraction was lower in the 4-baffles case than in the 9-baffles case.

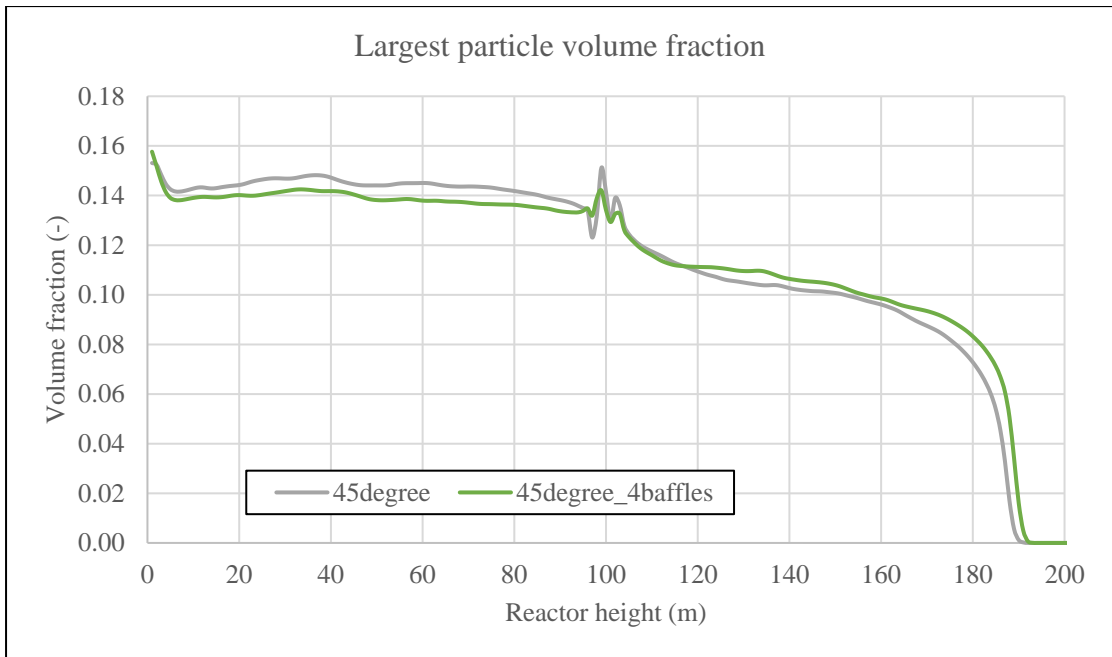


Figure 3.50 Largest particle volume fraction along reactor height

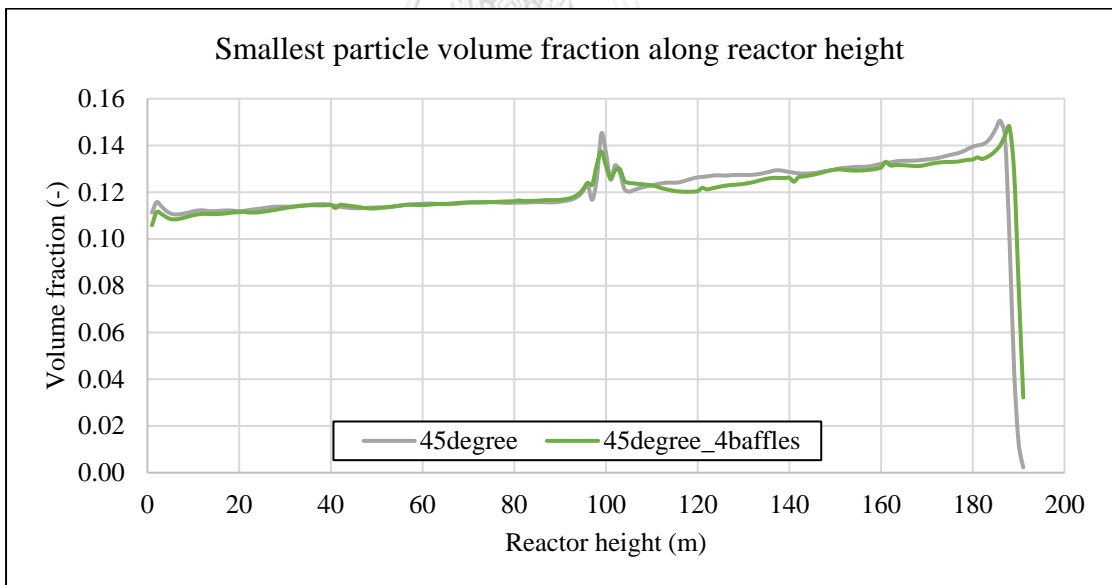


Figure 3.51 Smallest particle volume fraction along reactor height

Finally, the relative segregation rate was calculated for both cases, as shown in Figure 3.52. The results indicated that reducing the baffles number to 4 led to a decrease in segregation behavior in the system. This was due to the change in solid behavior, which led to differences in particle accumulation, as previously described.



Figure 3.52 Relative segregation rate

Chapter 4

Computational fluidized dynamics model of ethylene-butene copolymerization reaction in fluidized bed reactor

4.1 Introduction

In an industrial-scale setting, polyethylene is produced through the polymerization of ethylene in a fluidized bed reactor. Modifying these reactors is crucial for increasing production capacity. However, it is necessary to investigate the effects of reactor modifications on the quality of the polymer product before implementing any changes. In this study, a CFD model coupled with the method of moments was used to examine the copolymerization of ethylene and 1-butene in a fluidized bed reactor. The study aimed to investigate the influence of operational parameters on the quality of the polymer product.

4.2 Model Development

Computational Domain

In this chapter, computational domain was a part of the computational domain in chapter 3. The computational domain had a height of 14 meters and a diameter of 4.8 meters. Figure 4.1 illustrates the computational domain that was employed in this study.

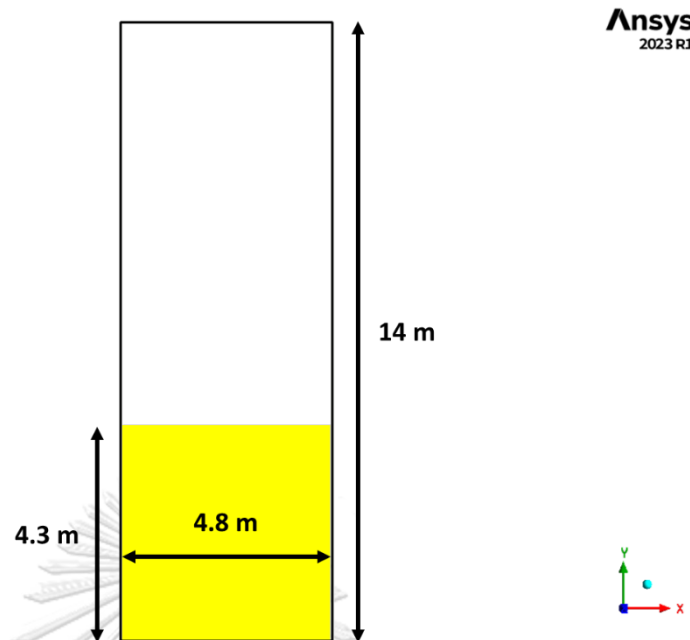


Figure 4.1 Illustration of computational domain

Mesh Construction

Since the computational domain in this chapter is a part of the one discussed in Chapter 3, the grid size used remains the same to ensure grid independence. In the grid independence test conducted in Chapter 3, it was shown that grid sizes of 0.075 and 0.05 meters gave similar results. However, a grid size of 0.075 meters was chosen in Chapter 3 to reduce computation costs. Since this chapter includes more equations compared to Chapter 3, a smaller grid size was found to be more suitable. Consequently, a grid size of 0.05 meters was determined. This grid size yielded grid independence, resulting in a total of 26,880 grid cells as illustrated in Figure 4.2.

Additionally, the Courant number was considered in this chapter to maintain the accuracy and stability of the numerical simulations. In this chapter, the velocity inlet was set to 0.6 meters per second, and the time step size was set to 0.005 seconds.

The Courant number in this chapter was determined to be 0.06, which remained within an acceptable range of 0.03 to 0.30.

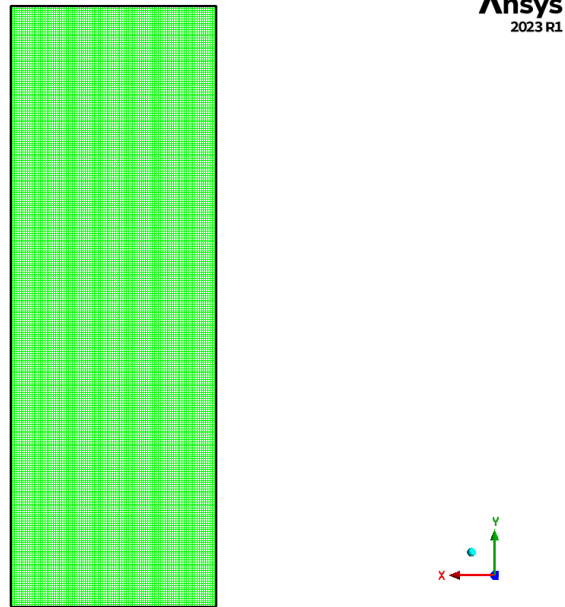


Figure 4.2 Illustrator of computational grid

Mathematical Model

In this section, a model was developed to simulate polymerization in a fluidized bed reactor by building upon the model discussed in chapter 3 and incorporating additional governing equations. The model included the conservation of mass and momentum equations, along with the conservation of species and energy equations. However, the polymerization fluidized bed reactor system was considered as an isothermal system. A two-dimensional transient computational fluid dynamics model with Euler-Euler approach was utilized to simulate the system, with the number of calculation phases reduced to two: the primary gas phase and the secondary solid phase, in order to simplify the complexity of the model. In this model,

gas and solid phase contained fluid species such as C₂H₄, C₄H₈, H₂ and N₂ for gas phase while solid phase consisted of catalyst, co-catalyst, active species, polymer chain and catalyst support as an inert.

Conservation of species^[28]

$$\frac{\partial}{\partial t}(\rho Y_i) + \nabla \cdot (\rho \vec{v} Y_i) = -\nabla \cdot \vec{J}_i + R_i + S_i \quad 4.1$$

Conservation of energy^[28]

$$\frac{\partial}{\partial t}(\rho E) + \nabla \cdot (\vec{v}(\rho E + p)) = \nabla \cdot \left(k_{eff} \nabla T - \sum_j h_j \vec{J}_j + (\vec{\tau}_{eff} \cdot \vec{v}) \right) + S_h \quad 4.2$$

Where

ρ was a fluid density (kg/m³)

Y_i was a mass fraction of component i

\vec{v} was a fluid velocity (m/s)

\vec{J}_i was the diffusion flux of species i (kg/m.s)

R_i was the net rate of production of species by chemical reaction

S_i was the rate of creation by addition from the dispersed phase plus any user-defined sources

E was a total energy (J)

p was a pressure (Pa)

k_{eff} was an effective conductivity (w/m.K)

h_j was a species enthalpy (energy/mass)

$\bar{\tau}_{eff}$ was an effective stress tensor (Pa)

S_h was an energy source term (W/m^3)

Model assumption

To simplify the model, certain assumptions were made in its development.

These assumptions consisted of

- The system was isothermal, and heat generation through the reaction was neglected. [5]
- The catalyst in the system was 2-site type catalyst. [2-4, 6, 33, 34]
- Particle size in the system was kept constant, and the growth rate of the polymer chain was neglected. [5]
- A pseudo-kinetic rate was used to simplify the various kinetic rate constants into one variable. [2-4, 6, 33-35]

Polymerization model

The polymerization reaction is a complex process that involves three main steps: initiation, propagation, and termination. During the propagation step, monomers and co-monomers react with the live polymer chains, resulting in the growth of the polymer chains and the formation of longer polymer chains. The number of reactions that occur during the propagation step is dependent on the length of the polymer chains and can therefore vary greatly.

The method of moments approach was employed to develop a numerical model for investigating polymerization reactions due to its ability to consider a large number of reactions involved in the propagation step, which is responsible for the growth of the polymer chain. Furthermore, this approach is capable of providing

information about the average molecular weight of the polymer chain in the system, which is a crucial parameter for determining the physical and chemical properties of the resulting polymer. Therefore, the method of moments approach is a suitable and powerful tool for developing a numerical model to investigate polymerization reactions.

To develop a polymerization model, the first step was to determine the elementary reactions involved in the process. Once the elementary reactions were identified, mole balance equations were created for each species involved in the reactions. In this study, the elementary reactions and the corresponding species mole balance equations were presented in Table 4.1. This set of equation was used in various study[2-6, 33, 34, 36]. The rate constant of each reaction with different site type were obtained from various literatures[2, 4, 6, 33, 34, 36] and shown in Table 4.2.

Table 4.1 Elementary equation and species mole balance equation used in the model.

Reaction	Mole balance equation
Formation reaction	$\frac{d}{dt} N^*(j) = -k_f(j)[N^*(j)]$ 4.3
$N^*(j) \xrightarrow{k_f(j)} N(\mathbf{0}, j)$	$\frac{d}{dt} N(\mathbf{0}, j) = k_f(j)[N^*(j)]$ 4.4
Initiation reaction	$\frac{d}{dt} N(\mathbf{0}, j) = -k_{i_1}(j)N(\mathbf{0}, j)[M_i]$ 4.5
$N(\mathbf{0}, j) + M_i \xrightarrow{k_{i_1}(j)} N_i(\mathbf{1}, j)$	$\frac{d}{dt} M_i = -k_{i_1}(j)N(\mathbf{0}, j)[M_i]$ 4.6
	$\frac{d}{dt} N_i(\mathbf{1}, j) = k_{i_1}(j)N(\mathbf{0}, j)[M_i]$ 4.7
Propagation reaction	$\frac{d}{dt} N_i(r, j) = -k_{p_{ik}}(j)N(r, j)[M_k]$ 4.8
$N_i(r, j) + M_k \xrightarrow{k_{p_{jk}}(j)} N_k(r+1, j)$	$\frac{d}{dt} [M_k] = -k_{p_{ik}}(j)N(r, j)[M_k]$ 4.9
	$\frac{d}{dt} N_k(r+1, j) = k_{p_{ik}}(j)N(r, j)[M_k]$ 4.10
Chain transfer to monomer reaction	$\frac{d}{dt} N_i(r, j) = -k_{p_{ik}}(j)N(r, j)[M_k]$ 4.11
$N_i(r, j) + M_k \xrightarrow{k_{fm_{jk}}(j)} N_k(\mathbf{1}, j) + Q(r, j)$	$\frac{d}{dt} [M_k] = -k_{p_{ik}}(j)N(r, j)[M_k]$ 4.12
	$\frac{d}{dt} N_k(\mathbf{1}, j) = k_{p_{ik}}(j)N(r, j)[M_k]$ 4.13
	$\frac{d}{dt} Q(r, j) = k_{p_{ik}}(j)N(r, j)[M_k]$ 4.14
Chain transfer to hydrogen reaction	$\frac{d}{dt} N_i(r, j) = -k_{fh_i}(j)N(r, j)[H_2]$ 4.15
$N_i(r, j) + H_2 \xrightarrow{k_{fh_i}(j)} N_H(\mathbf{0}, j) + Q(r, j)$	$\frac{d}{dt} [H_2] = -k_{fh_i}(j)N(r, j)[H_2]$ 4.16
	$\frac{d}{dt} N_H(\mathbf{0}, j) = k_{fh_i}(j)N(r, j)[H_2]$ 4.17
	$\frac{d}{dt} Q(r, j) = k_{fh_i}(j)N(r, j)[H_2]$ 4.19
Chain transfer to co-catalyst reaction	$\frac{d}{dt} N_i(r, j) = -k_{fr_i}(j)N(r, j)[AlEt_3]$ 4.20
$N_i(r, j) + AlEt_3 \xrightarrow{k_{fr_i}(j)} N_1(\mathbf{1}, j) + Q(r, j)$	$\frac{d}{dt} [AlEt_3] = -k_{fr_i}(j)N(r, j)[AlEt_3]$ 4.21
	$\frac{d}{dt} N_1(\mathbf{1}, j) = k_{fr_i}(j)N(r, j)[AlEt_3]$ 4.22
	$\frac{d}{dt} Q(r, j) = k_{fr_i}(j)N(r, j)[AlEt_3]$ 4.23

Reaction	Mole balance equation
Spontaneous transfer	$\frac{d}{dt} N_i(r, j) = -k_{fs_i}(j) N_i(r, j)$ 4.24
$N_i(r, j) \xrightarrow{k_{fs_i}(j)} N_H(0, j) + Q(r, j)$	$\frac{d}{dt} N_H(0, j) = k_{fs_i}(j) N_i(r, j)$ 4.25
	$\frac{d}{dt} Q(r, j) = k_{fs_i}(j) N_i(r, j)$ 4.26
Deactivation reaction	$\frac{d}{dt} N_i(r, j) = -k_{ds}(j) N_i(r, j)$ 4.27
$N_i(r, j) \xrightarrow{k_{ds}(j)} N_d(j) + Q(r, j)$	$\frac{d}{dt} N_d(j) = k_{ds}(j) N_i(r, j)$ 4.28
	$\frac{d}{dt} Q(r, j) = k_{ds}(j) N_i(r, j)$ 4.29

Where

$N^*(j)$ was an inactive catalyst of site j

$N(0, j)$ was an active catalyst of site j

$N_i(1, j)$ was a live polymer chain of length 1 which terminal monomer i attached to the catalyst site-type j

$N_i(r, j)$ was a live polymer chain of length r which terminal monomer i attached to the catalyst site-type j

$N_H(0, j)$ was an active catalyst of site j

$N_d(j)$ was dead catalyst of site j

$Q(r, j)$ was a dead polymer chain of length r attached to the catalyst site-type j

M_i was a monomer type i

$AlEt_3$ was a co-catalyst (triethyl aluminum)

- $k_f(j)$ was a kinetic rate constant for the formation reaction
- $k_f(j)$ was a kinetic rate constant for the formation reaction
- $k_{i_1}(j)$ was a kinetic rate constant for the initiation reactions
- $k_{p_{jk}}(j)$ was a kinetic rate constant for the propagation reaction of monomer M_k reacted with an active center of type j , bonded to a terminal monomer M_i
- $k_{fm_{jk}}(j)$ was a kinetic rate constant for the chain transfer to monomer reaction
- $k_{fh_i}(j)$ was a kinetic rate constant for the chain transfer to hydrogen reaction
- $k_{fr_i}(j)$ was a kinetic rate constant for the chain transfer to co-catalyst reaction
- $k_{fs_i}(j)$ was a kinetic rate constant for the spontaneous transfer reaction
- $k_{ds}(j)$ was a kinetic rate constant for the deactivation reaction

Table 4.2 Kinetic rate constant of elementary reaction

Reaction	Rate constant	Unit	Site type 1	Site type 2
Formation	$k_f(j)$	s^{-1}	1	1
Initiation	$k_{i_1}(j)$	$L \text{ kmol}^{-1} s^{-1}$	1	1
	$k_{i_2}(j)$	$L \text{ kmol}^{-1} s^{-1}$	0.14	0.14
	$k_{h_1}(j)$	$L \text{ kmol}^{-1} s^{-1}$	1	1
	$k_{h_2}(j)$	$L \text{ kmol}^{-1} s^{-1}$	0.1	0.1
	$k_{h_r}(j)$	$L \text{ kmol}^{-1} s^{-1}$	20	20
Propagation	$k_{p_{11}}(j)$	$L \text{ kmol}^{-1} s^{-1}$	85	85
	$k_{p_{12}}(j)$	$L \text{ kmol}^{-1} s^{-1}$	2	15
	$k_{p_{21}}(j)$	$L \text{ kmol}^{-1} s^{-1}$	64	64
	$k_{p_{22}}(j)$	$L \text{ kmol}^{-1} s^{-1}$	1.5	6.2
Chain transfer	$k_{fm_{11}}(j)$	$L \text{ kmol}^{-1} s^{-1}$	0.0021	0.0021
	$k_{fm_{12}}(j)$	$L \text{ kmol}^{-1} s^{-1}$	0.006	0.11
	$k_{fm_{21}}(j)$	$L \text{ kmol}^{-1} s^{-1}$	0.0021	0.001
	$k_{fm_{22}}(j)$	$L \text{ kmol}^{-1} s^{-1}$	0.006	0.11
	$k_{fh_1}(j)$	$L \text{ kmol}^{-1} s^{-1}$	0.088	0.37
	$k_{fh_2}(j)$	$L \text{ kmol}^{-1} s^{-1}$	0.088	0.37
	$k_{fr_1}(j)$	$L \text{ kmol}^{-1} s^{-1}$	0.024	0.12
	$k_{fr_2}(j)$	$L \text{ kmol}^{-1} s^{-1}$	0.048	0.24
	$k_{fs_1}(j)$	$L \text{ kmol}^{-1} s^{-1}$	0.0001	0.0001
	$k_{fs_2}(j)$	$L \text{ kmol}^{-1} s^{-1}$	0.0001	0.0001
Deactivation	$k_{ds}(j)$	s^{-1}	0.0001	0.0001
	$k_{di}(j)$	$L \text{ kmol}^{-1} s^{-1}$	2000	2000

To develop the model using the method of moments, the live polymer chains (chains capable of further growth) and dead polymer chains (chains without the ability to grow further) were considered separately. The generally moment equations for the live and dead polymer chains were presented in Equations 4.30 and 4.31, respectively.

Live polymer moment equation

$$Y(n, j) = \sum_{r=1}^{\infty} r^n \{N_1(r, j) + N_2(r, j) + \dots\} \quad 4.30$$

Dead polymer equation

$$X(n, j) = \sum_{r=1}^{\infty} r^n Q(r, j) \quad 4.31$$

Where

$Y(n, j)$ was a n^{th} -order moment of live polymer of site-type j

$X(n, j)$ was a n^{th} -order moment of dead polymer of site-type j

r was a chain length

In this study, a copolymerization system with two monomers and a two-site catalyst was considered, and zeroth to second-order moments were taken into account. Therefore, moment equations for live and dead polymer chains with any type of catalyst site in this study were presented in equations 4.32-4.37.

Live polymer moment equation for any catalyst site type

$$Y(0, j) = \sum_{r=1}^{\infty} \{N_1(r, j) + N_2(r, j)\} \quad 4.32$$

$$Y(1, j) = \sum_{r=1}^{\infty} r \{N_1(r, j) + N_2(r, j)\} \quad 4.33$$

$$Y(2, j) = \sum_{r=1}^{\infty} r^2 \{N_1(r, j) + N_2(r, j)\} \quad 4.34$$

Dead polymer moment equation for any catalyst site type

$$X(0, j) = \sum_{r=1}^{\infty} Q(r, j) \quad 4.35$$

$$X(1, j) = \sum_{r=1}^{\infty} rQ(r, j) \quad 4.36$$

$$X(2, j) = \sum_{r=1}^{\infty} r^2 Q(r, j) \quad 4.37$$

To introduce the moment equation into the computational fluid dynamics model, each moment equation was modified into the transient form by differentiating both sides of the equation with respect to time.

Derivative live polymer moment equation for any catalyst site type

$$\frac{d}{dt} Y(0, j) = \sum_{r=1}^{\infty} \left\{ \frac{d}{dt} N_1(r, j) + \frac{d}{dt} N_2(r, j) \right\} \quad 4.38$$

$$\frac{d}{dt} Y(1, j) = \sum_{r=1}^{\infty} r \left\{ \frac{d}{dt} N_1(r, j) + \frac{d}{dt} N_2(r, j) \right\} \quad 4.39$$

$$\frac{d}{dt} Y(2, j) = \sum_{r=1}^{\infty} r^2 \left\{ \frac{d}{dt} N_1(r, j) + \frac{d}{dt} N_2(r, j) \right\} \quad 4.40$$

Derivative dead polymer moment equation for any catalyst site type

$$\frac{d}{dt} X(0, j) = \sum_{r=1}^{\infty} \frac{d}{dt} Q(r, j) \quad 4.41$$

$$\frac{d}{dt} X(1, j) = \sum_{r=1}^{\infty} r \frac{d}{dt} Q(r, j) \quad 4.42$$

$$\frac{d}{dt} X(2, j) = \sum_{r=1}^{\infty} r^2 \frac{d}{dt} Q(r, j) \quad 4.43$$

The right-hand side of the live and dead polymer chain derivative was replaced by the mole balance equation and rewritten into the moment form. Examples of the equations are shown in equations 4.44-4.49.

$$\begin{aligned} \frac{d}{dt}Y(0,j) &= [M_T]\{ki_T(j)N(0,j) + kh_T(j)N_H(0,j)\} + kh_r(j)N_H(0,j)[AlEt_3] \\ &\quad - Y(0,j)\{kfh_T(j)[H_2] + kfs_T(j) + kds(j)\} \end{aligned} \quad 4.44$$

$$\begin{aligned} \frac{d}{dt}Y(1,j) &= [M_T]\{ki_T(j)N(0,j) + kh_T(j)N_H(0,j)\} + kh_r(j)N_H(0,j)[AlEt_3] + [M_T]kp_{TT}(j)Y(0,j) \\ &\quad + \{Y(0,j) - Y(1,j)\}\{kfm_{TT}(j)[M_T] + kfh_T(j)[AlEt_3]\} \\ &\quad - Y(1,j)\{kfh_T(j)[H_2] + kfs_T(j) + kds(j)\} \end{aligned} \quad 4.45$$

$$\begin{aligned} \frac{d}{dt}Y(2,j) &= [M_T]\{ki_T(j)N(0,j) + kh_T(j)N_H(0,j)\} + kh_r(j)N_H(0,j)[AlEt_3] \\ &\quad + [M_T]kp_{TT}(j)\{2Y(1,j) - Y(0,j)\} \\ &\quad + \{Y(0,j) - Y(2,j)\}\{kfm_{TT}(j)[M_T] + kfh_T(j)[AlEt_3]\} \\ &\quad - Y(2,j)\{kfh_T(j)[H_2] + kfs_T(j) + kds(j)\} \end{aligned} \quad 4.46$$

$$\begin{aligned} \frac{d}{dt}X(0,j) &= \{Y(0,j) - N_T(1,j)\}\{kfm_{TT}(j)[M_T] + kfh_T(j)[AlEt_3] + kfh_T(j)[H_2] + kfs_T(j) \\ &\quad + kds(j)\} \end{aligned} \quad 4.47$$

$$\begin{aligned} \frac{d}{dt}X(1,j) &= \{Y(1,j) - N_T(1,j)\}\{kfm_{TT}(j)[M_T] + kfh_T(j)[AlEt_3] + kfh_T(j)[H_2] \\ &\quad + kfs_T(j) + kds(j)\} \end{aligned} \quad 4.48$$

$$\begin{aligned} \frac{d}{dt}X(2,j) &= \{Y(2,j) - N_T(1,j)\}\{kfm_{TT}(j)[M_T] + kfh_T(j)[AlEt_3] + kfh_T(j)[H_2] \\ &\quad + kfs_T(j) + kds(j)\} \end{aligned} \quad 4.49$$

The live and dead polymer chain derivative were introduced into the computational fluid dynamics through scalar equation. The ordinary scalar equation[28] was

$$\frac{d}{dt}\alpha_l\rho_l\phi_l^k + \nabla \cdot (\alpha_l\rho_l\vec{v}_l\phi_l^k - \alpha_l\Gamma_l^k\nabla\phi_l^k) = S_l^k \quad 4.50$$

The ordinary equation was modified into this equation.

$$\frac{d}{dt} \phi_i^k = S_i^k \quad 4.51$$

Where

α_l was a volume fraction

ρ_l was a physical density (kg/m³)

\vec{v}_l was a velocity (m/s)

Γ_l^k was the diffusion coefficient (m²/s)

S_l^k was the scalar source term (unit/m³.s)

The right-hand side of each moment derivative equation was introduced into the computational fluid dynamics model through source term of the modified scalar equation and using a user-defined function in the commercial program ANSYS FLUENT. The flow diagram of coupling model was shown in Figure 4.3.

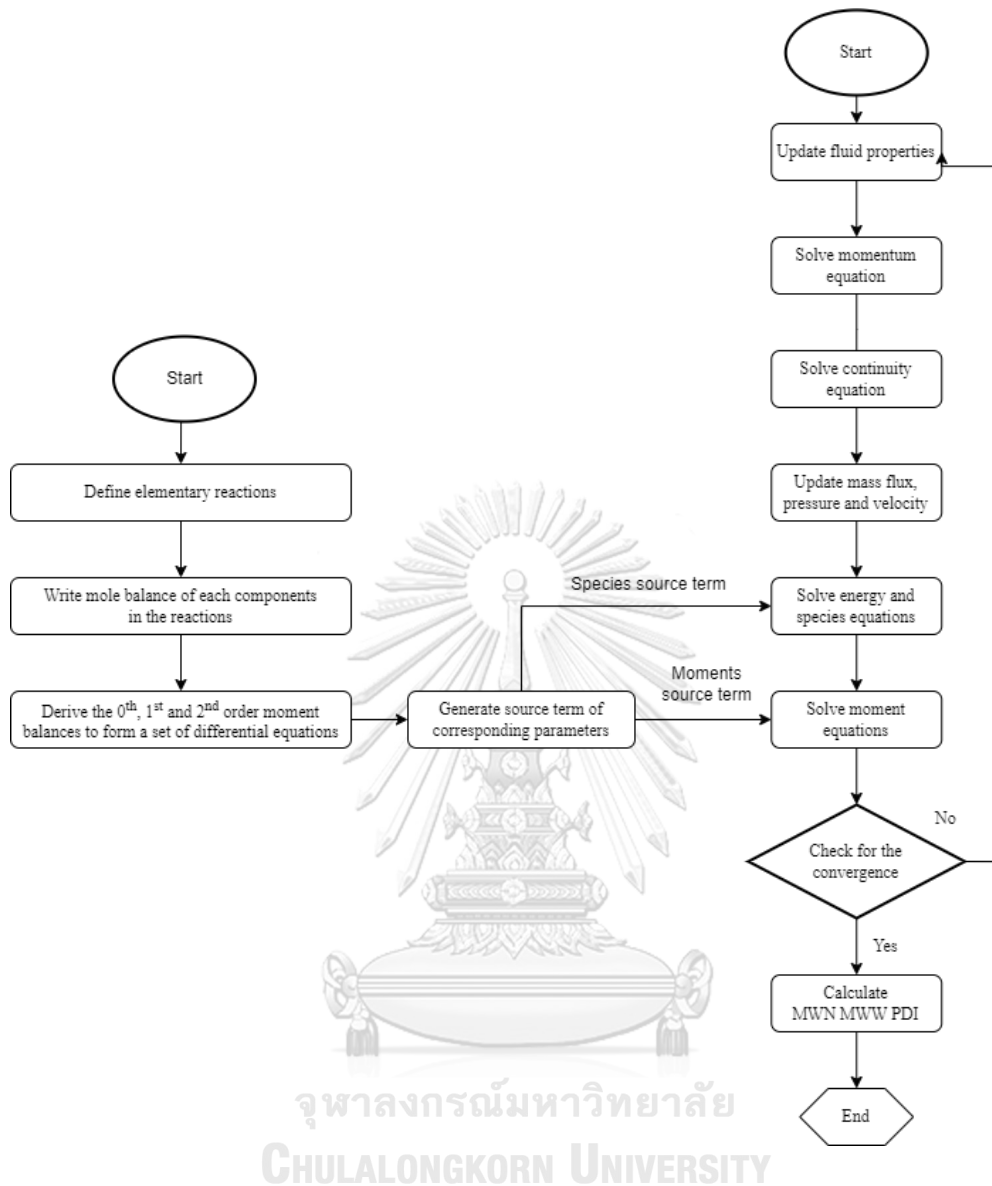


Figure 4.3 Flow diagram of the coupling model^[9, 28]

Boundary Condition

As in chapter 3, this chapter considers three boundary conditions applied to the model: the inlet, outlet, and wall. The inlet was located at the bottom of the reactor, while the outlet was positioned at the top. Each of these boundary conditions is described in detail below.

- For the inlet boundary condition, only gas was fed into the reactor with 0.6 m/s and 349.15 K. The density and viscosity of mixture gas (C₂H₄, C₄H₈, H₂, and N₂) at 2000 kPa were constant at 20 kg/m³ and 1.2×10⁻⁵

Pa.s, respectively. The mole fraction of C_2H_4 , C_4H_8 , H_2 , and N_2 were 0.4, 0.17, 0.09 and 0.34, respectively.

- For the outlet boundary condition, constant pressure was set as the pressure outlet. Pressure at the outlet was set to 2000 kPa.
- For the wall boundary condition, the gas phase was set as a no-slip condition. All solid particle phases were set as the partially slip condition.

Initial conditions

- In this chapter, the initial condition of solid particles was changed from chapter 3. According to the literature [36], well-mixed particles were filled into a 4.3-meter height from the bottom of the reactor with a volume fraction of 0.33 for solid particles.
- The solid species initially existed with mass fractions of catalyst site types 1 and 2, and cocatalyst fractions of 0.3, 0.3, and 0.399, respectively. Moreover, to increase the stability of the simulation in the early stages, the mass fraction of the polymer product was set to 0.001. With this fraction, the cocatalyst was in excess for reacting with the catalyst to form an active catalyst.
- The gas species initially existed with a mole fraction equal to the inlet conditions.
- The system temperature was set to 345 K.

4.3 Model Validation

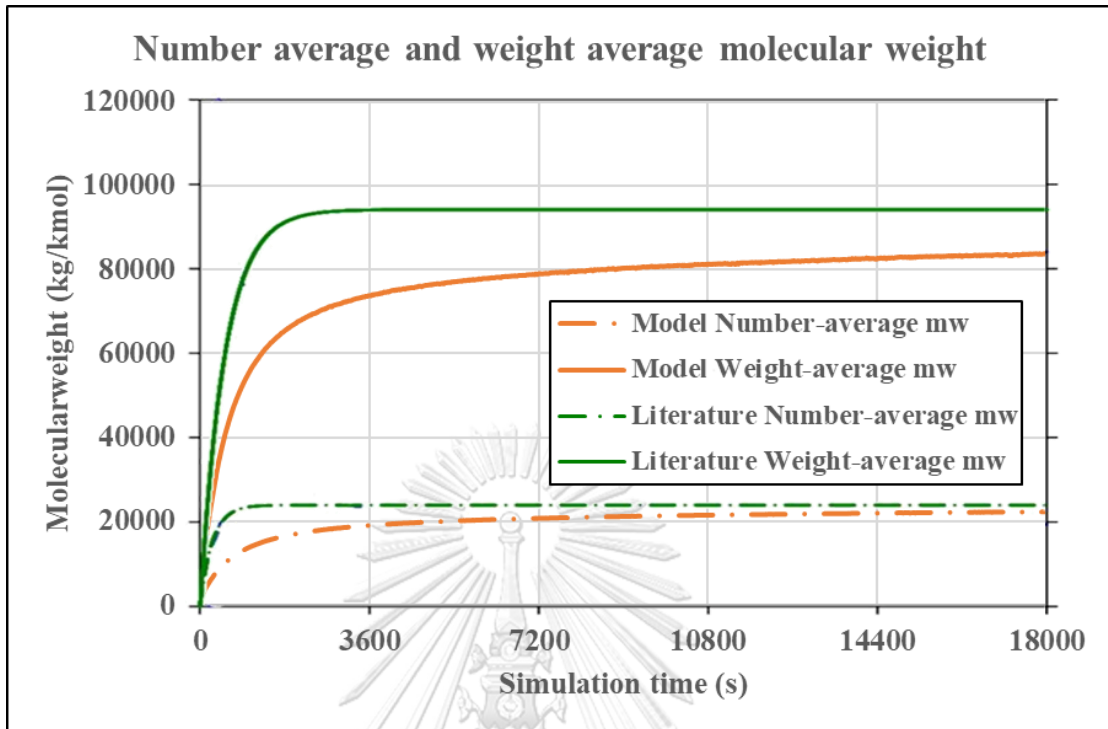


Figure 4.4 Comparison of weight-average and number-average molecular weight between literature data [28] and simulation model

To validate the model, weight-average and number-weight molecular weights were compared with literature data [36]. The results, illustrated in Figure 4.4, showed that both molecular weights were close to the literature data as the simulation time increased. At 18000 seconds of simulation time, the error of the number-average was approximately 15%. This error occurred due to the difference between the numerical model used in this study, which employed a CFD model, and the lump system model used in the literature.

The main difference between the literature model and this model was the system homogeneity. As shown in Figure 4.5, the literature model separated the system into several segments and used CSTR and plug flow reactor represented

emulsion phase and bubble phase, respectively. When the CSTR represents the emulsion phase, it indicates a complete mixing of the solid and gas phases. Additionally, in the literature model, it was assumed that radial concentration and temperature gradients in the reactor were negligible.

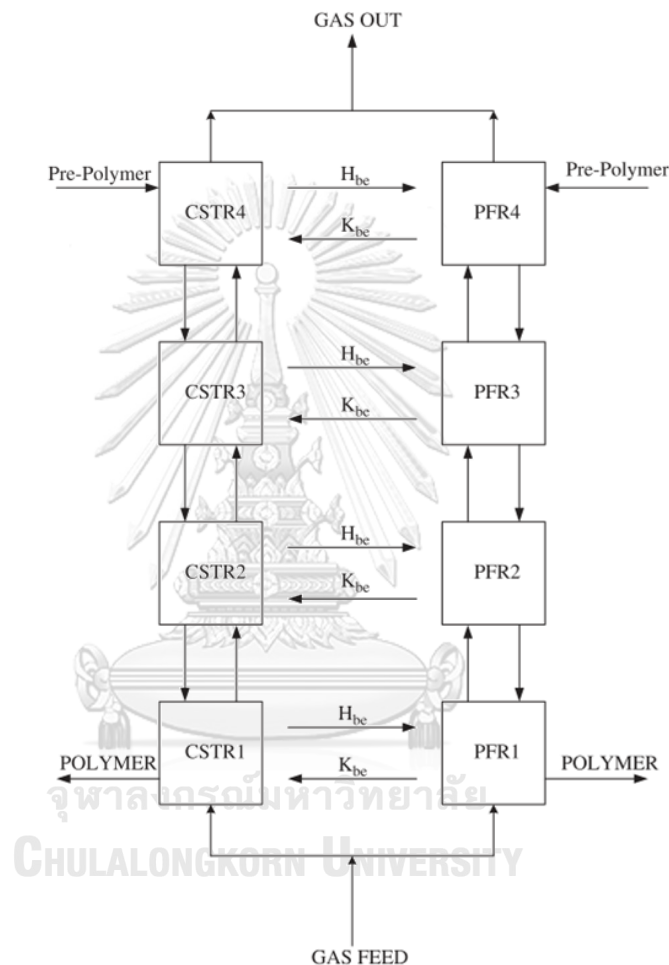


Figure 4.5 Schematic diagram of literature model[6]

In the CFD model, the system was divided into smaller segments known as grid cells. In this approach, the mixing of the gas and solid phases was not entirely homogeneous but instead depended on the behaviors of the system calculated from governing equations within each individual cell. Furthermore, the CFD model was capable of providing the radial distribution of gas and solid particles as shown in Figures 4.6 and 4.7.

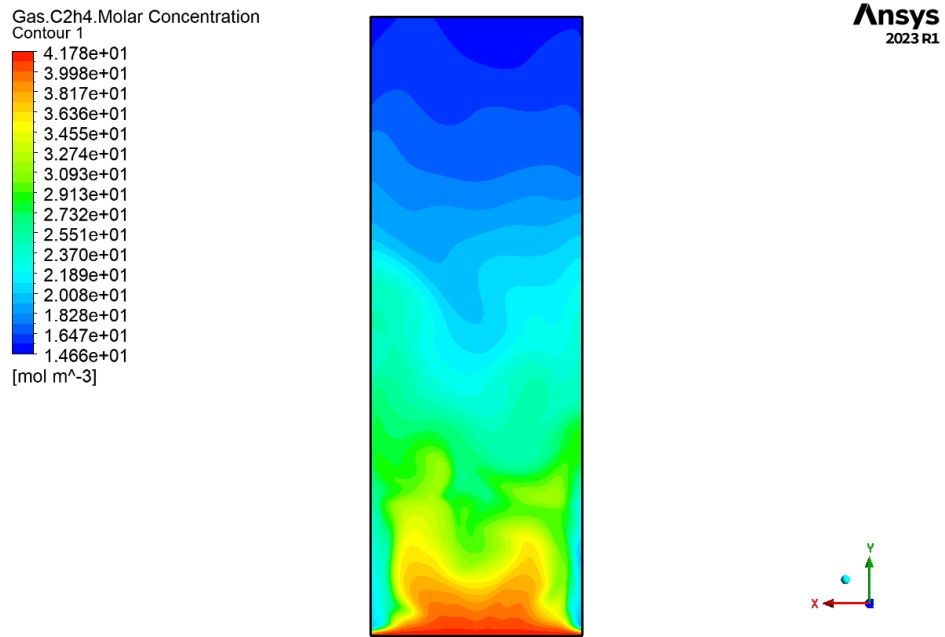


Figure 4.6 Ethylene distribution in the system

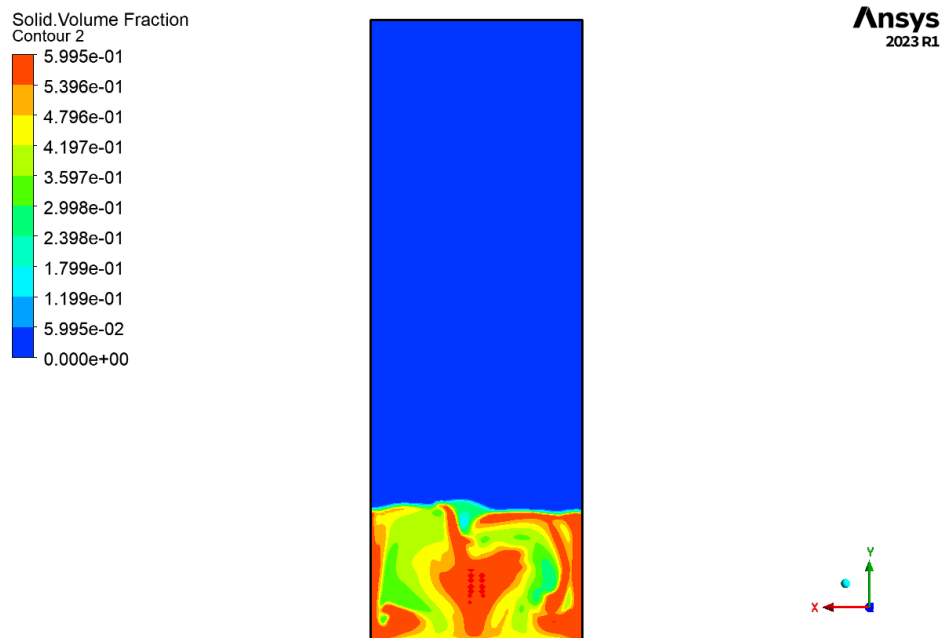


Figure 4.7 Solid distribution in the system

A lower system homogeneity leads to variations in monomer and comonomer concentrations within the system, resulting in a lower reaction rate compared to a homogeneous system represented by the moment value and leading to a lower average molecular weight of the polymer product as shown in the Figure 4.4.

Even though the error of this model was higher than 10%, this model provided the same trend of both number-average and weight-average molecular weight growth. Moreover, it could provide data on both hydrodynamics and polymer product properties. Thus, this model was appropriate for studying the polymerization reaction in a fluidized bed reactor in the next investigation.

4.4 Parametric Study

The parameters used in this study were suggested. The parameters investigated included 1-butene fraction, the ratio of H₂ per C₂, and the catalyst amount. In this study, the values of these parameters were adjusted, increasing or decreasing them by 30% from the base case value. To consider effect of each parameters and effect of interaction among them, 2^k factorial design was used in this study. Overall simulation run was 9 including base case, all run details was shown in the Table 4.3.

Table 4.3 Detail of the studied parameter of each run

Run no.	%Comonomer	H2 to C2 ratio	Catalyst amount
1 (Base case)	-	-	-
2 (+++)	+30%	+30%	+30%
3 (-++)	-30%	+30%	+30%
4 (+-+)	+30%	-30%	+30%
5 (--+)	-30%	-30%	+30%
6 (---)	-30%	-30%	-30%
7 (+--)	+30%	-30%	-30%
8 (-+-)	-30%	+30%	-30%
9 (++-)	+30%	+30%	-30%

Simulation results

Average molecular weight

Figures 4.8 and 4.9 showed the weight-average molecular weight in the system. When considering the instantaneous weight-average molecular weight in Figure 4.7, the comonomer content had a significant effect on the weight-average molecular weight. In the first hour of the simulation time, the weight-average molecular weight increased rapidly and showed a slight effect of the catalyst amount. However, the weight-average molecular weight continued to increase slightly, and the effect of the catalyst amount disappeared after the first hour.

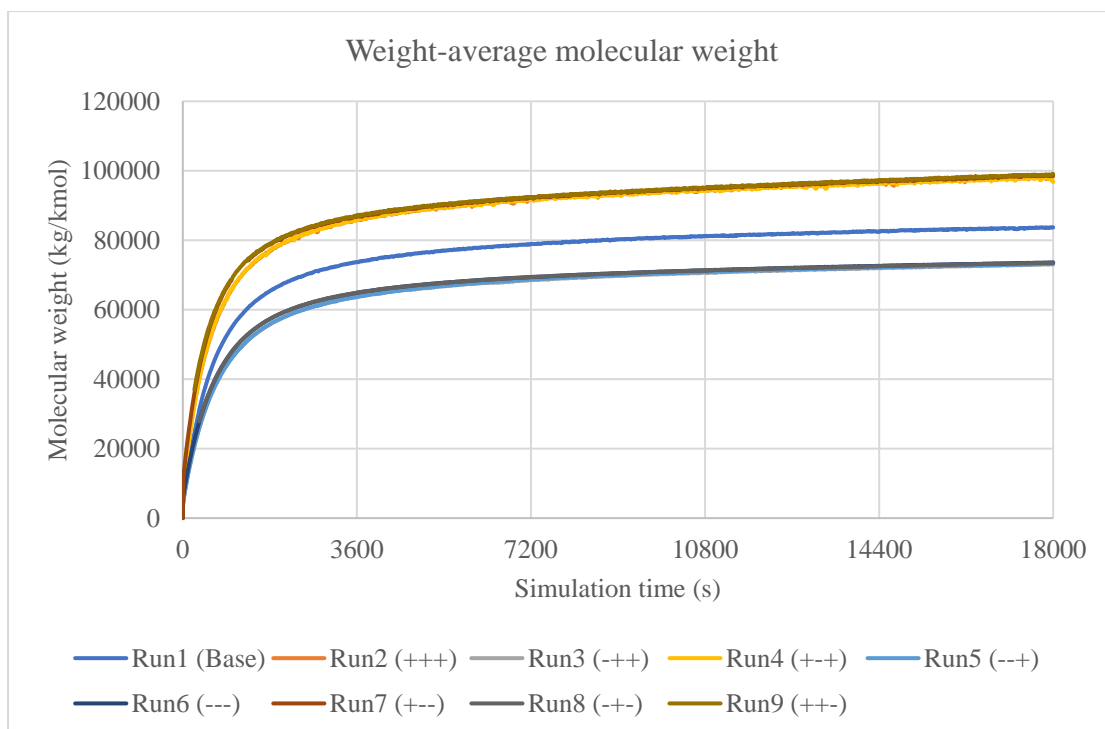


Figure 4.8 Instantaneous weight-average molecular weight

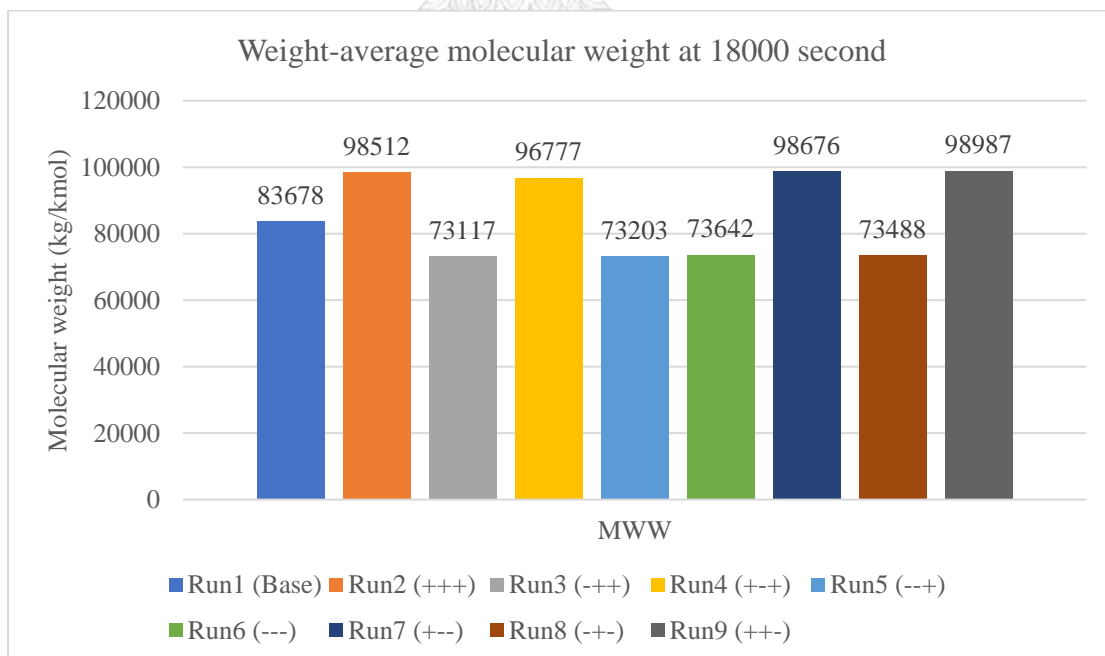


Figure 4.9 Weight-average molecular weight at 18000 second

Moreover, Figure 4.9 showed that increasing the comonomer content increased the weight-average molecular weight. On the other hand, decreasing the comonomer content decreased the weight-average molecular weight. However, the effect of the H₂toC₂ ratio and catalyst amount on the weight-average molecular weight was not significant.

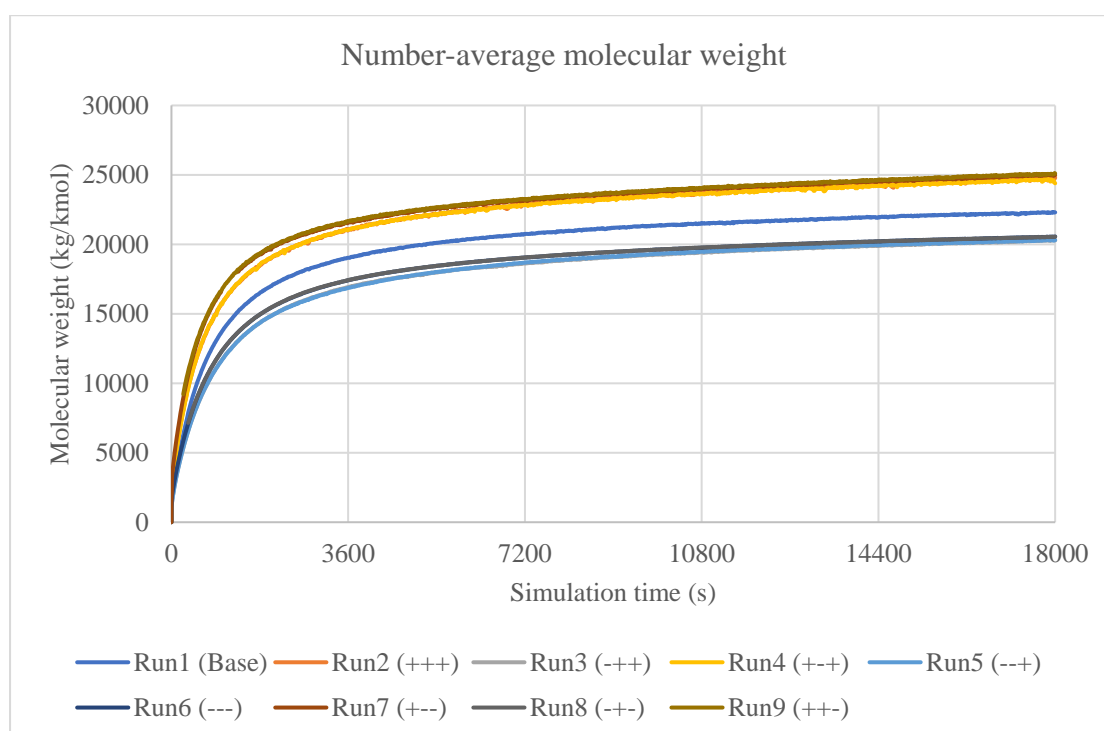


Figure 4.10 Instantaneous number-average molecular weight

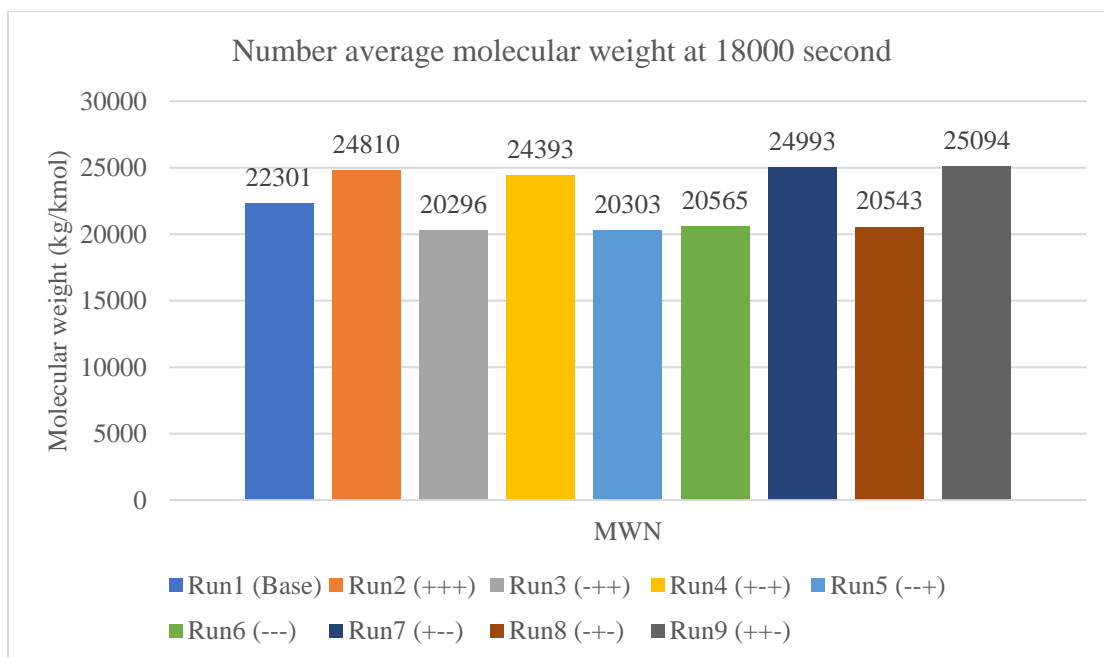


Figure 4.11 Number-average molecular weight at 18000 second

Figures 4.10 and 4.11 showed the number-average molecular weight in the system. Similar to the weight-average molecular weight, the comonomer content had a significant effect while H₂toC₂ ratio had no effect on the number-average molecular weight. In the first hour of the simulation time, the number-average molecular weight increased rapidly and then continued to increase slightly. However, the effect of the catalyst amount was more apparent in the number-average molecular weight than in the weight-average molecular weight.

To investigate the effect of the parameters clearly, the weight-average and number-average molecular weight were analyzed using the analysis of variance method.

Table 4.4 Analysis of variance table of weight-average molecular weight

Source	Sum of Squares	DF	Mean Square	F Value	Prob > F
Model	1.24E+09	3	4.13E+08	1.13E+03	< 0.0001
%Comonomer	1.24E+09	1	1.24E+09	3.40E+03	< 0.0001
H2toC2 ratio	4.08E+05	1	4.08E+05	1.11	0.3512
Catalyst amount	1.27E+06	1	1.27E+06	3.48	0.1365
Residual	1.47E+06	4	3.67E+05		
Cor Total	1.24E+09	7			

Table 4.5 Analysis of variance table of number-average molecular weight

Source	Sum of Squares	DF	Mean Square	F Value	Prob > F
Model	3.89E+07	3	1.30E+07	6.49E+02	< 0.0001
%Comonomer	3.86E+07	1	3.86E+07	1.93E+03	< 0.0001
H2toC2 ratio	2.97E+04	1	2.97E+04	1.488	0.2896
Catalyst amount	2.43E+05	1	2.43E+05	12.158	0.0252
Residual	7.99E+04	4	2.00E+04		
Cor Total	3.91E+07	7			

Effect of comonomer content

From the analysis of variance table, it is evident, with 95% confidence, that the parameter significantly affecting the weight-average and number-average molecular weight is the comonomer content. Increasing the comonomer content results in a higher comonomer concentration in the system, while decreasing it leads to a lower comonomer concentration, as shown in Figure 4.12. Furthermore, Figure

4.12 illustrates that the comonomer is not completely consumed, and there is excess comonomer that flows out of the reactor at the outlet.

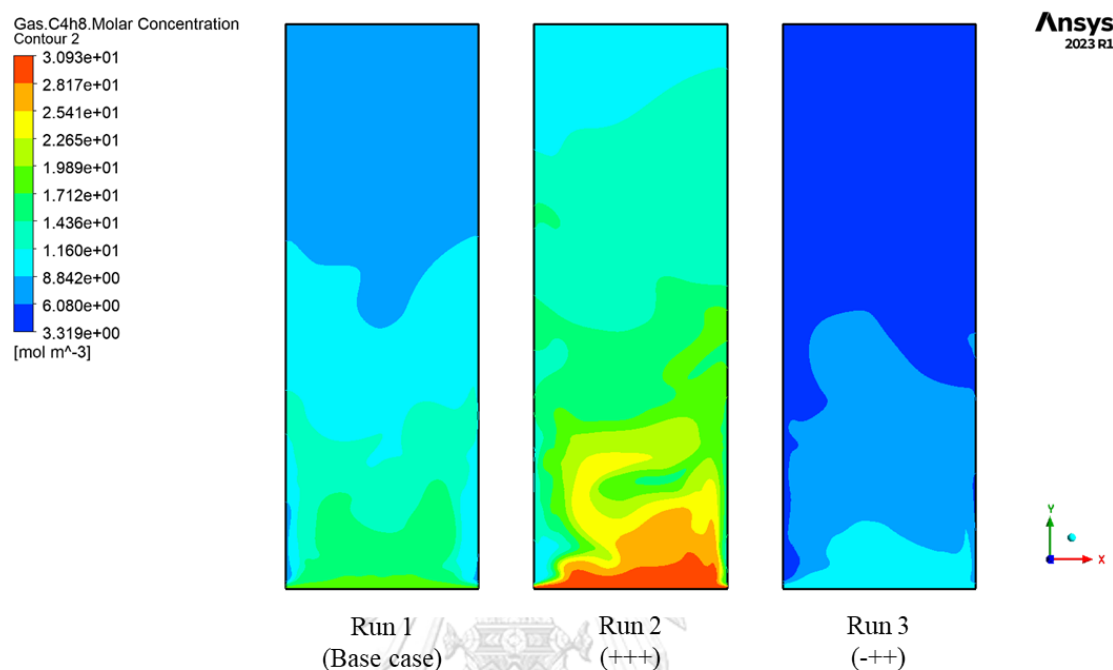


Figure 4.12 1-butene concentration in the system comparison of run 1, 2 and 3

Increasing the concentration of comonomer led to an increase in the reaction rate of the reactions involving comonomer consumption, which included initiation, propagation, and chain transfer to monomer. Due to the highest kinetic rate constant, as shown in Table 4.2, the majority of the comonomer was consumed in the propagation reaction, resulting in longer polymer chains in the system and leading to an increase in both the weight-average and number-average molecular weights.

On the other hand, decreasing comonomer concentration leads to a decrease in the reaction rate of the reactions involving comonomer consumption, resulting in

shorter polymer chains in the system and leading to a decrease in both the weight-average and number-average molecular weights.

Effect of H₂ to C₂ ratio

The hydrogen gas in the system was a one of chain terminate due to chain transfer to hydrogen reaction. In this study, the ratio of hydrogen gas to monomer was investigated. However, the ANOVA test showed that H₂ to C₂ ratio did not affect weight-average, number-average molecular weight. Considering the hydrogen distribution in the system as illustrated in Figure 4.13.

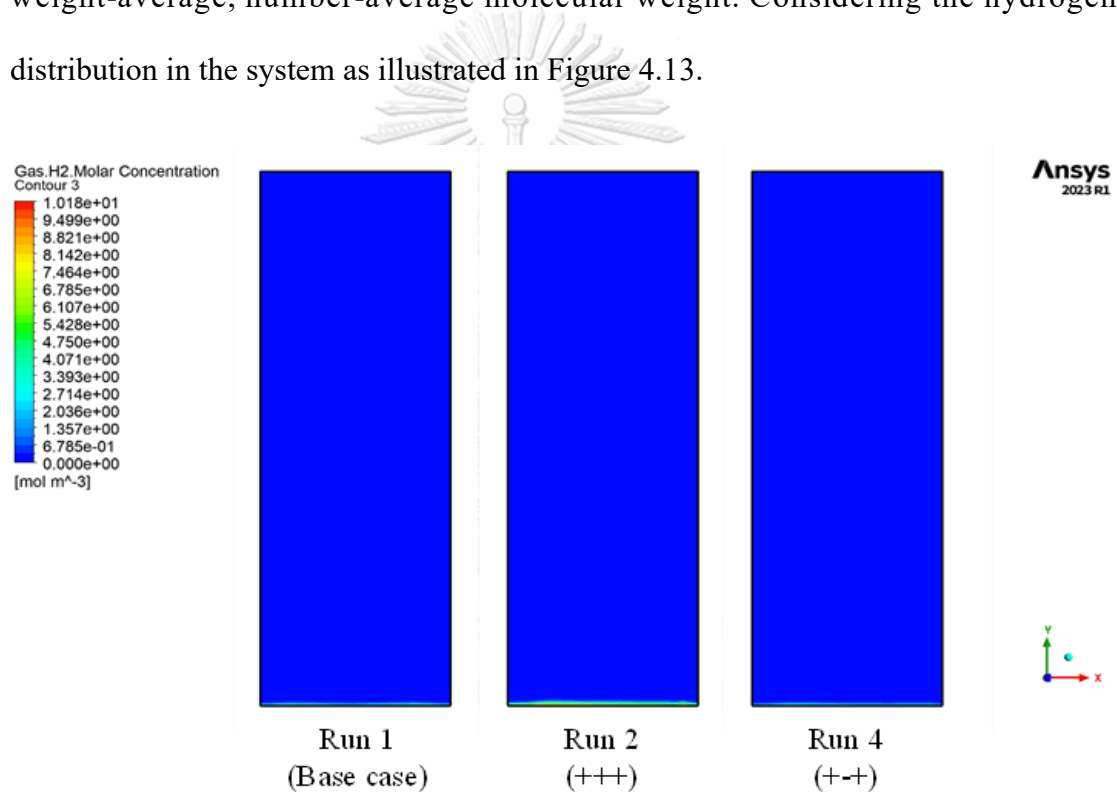


Figure 4.13 Hydrogen concentration in the system comparison of

Figure 4.13 illustrated that hydrogen gas was fed into the reactor at the bottom and consumed rapidly. When considering the mass flow rate of hydrogen gas, it was found that the hydrogen mass flow rates for runs 1, 2, and 4 were 0.00277 kg/sec, 0.00485 kg/sec, and 0.002579 kg/sec, respectively. Since the feed rate of hydrogen

gas was very low and the consumption rate was high, the hydrogen gas did not distribute evenly throughout the reactor and might not have a significant effect on the system.

However, the weight-average molecular weight and number-average molecular weight increased slightly when the H₂toC₂ ratio increased. This behavior occurred in the system with high comonomer content, and it was inconsistent with the real effect of H₂toC₂. On the other hand, the weight-average molecular weight and number-average molecular weight decreased slightly when the H₂toC₂ ratio increased. This behavior occurred in the system with low comonomer content, and it was consistent with the real effect of H₂toC₂. The inconsistent behavior might occur due to a numerical error resulting from certain assumptions made in the model.

Consider the 1st-order moment equation as equation 4.45.

$$\begin{aligned} \frac{d}{dt}Y(1,j) = & [M_T]\{ki_T(j)N(0,j) + kh_T(j)N_H(0,j)\} + kh_r(j)N_H(0,j)[AlEt_3] + [M_T]kp_{TT}(j)Y(0,j) \\ & + \{Y(0,j) - Y(1,j)\}\{kfm_{TT}(j)[M_T] + kfh_T(j)[AlEt_3]\} \\ & - Y(1,j)\{kfh_T(j)[H_2] + kfs_T(j) + kds(j)\} \end{aligned} \quad 4.45$$

In this model, a pseudo-kinetic rate was utilized as an average kinetic rate between the monomer and comonomer. Furthermore, the concentration in the moment equation was the total concentration. When the system contained a high comonomer content, the propagation term in the equation might have dominated the moment equations due to its higher kinetic rate compared to other reactions. This had led to inconsistent numerical results with the real effect of the H₂toC₂ ratio. Conversely, in a system with low comonomer content, the propagation term could have been weaker,

and the chain transfer to hydrogen term might have had a more significant effect on the moment values. As a result, the weight-average and number-average molecular weights decreased when the H₂toC₂ ratio increased in the system with low comonomer content.

Effect of the catalyst amount

Increasing or decreasing the amount of catalyst in the system did not affect the weight-average molecular weight but did affect the number-average molecular weight. In this study, the catalyst simply served as an initiator after being triggered by a co-catalyst. Increasing or decreasing the amount of catalyst affected solid behavior in the system as illustrated in Figure 4.14, increasing the amount of the catalyst led to higher solid bed height while decreasing the amount of the catalyst did not significantly decrease solid bed height. However, lower solid volume fraction in the bed could be observed when decreased amount of the catalyst.

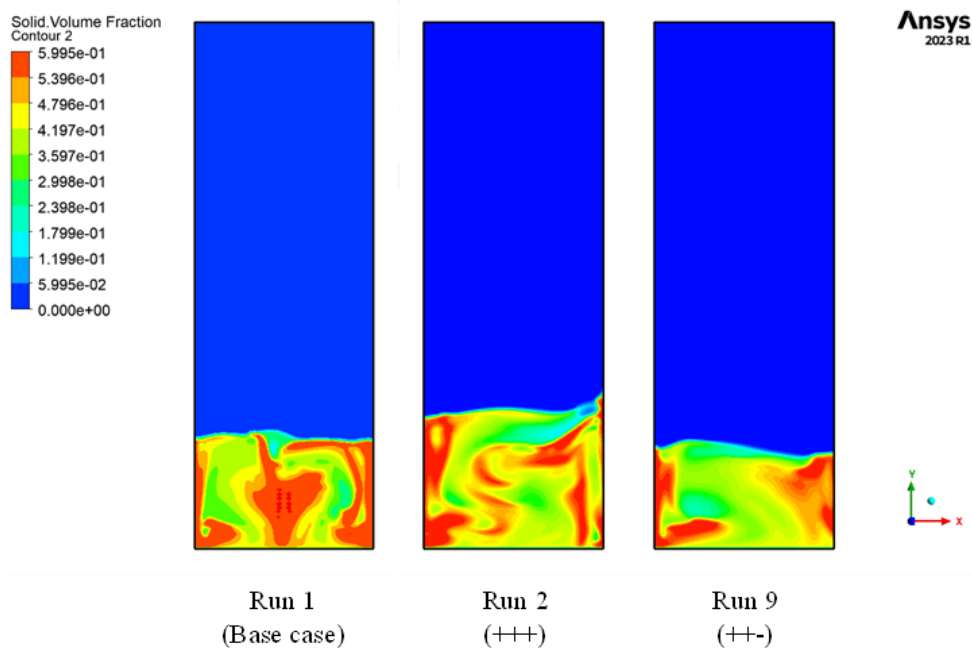


Figure 4.14 Solid volume fraction in the system comparison of run 1 2 and 9

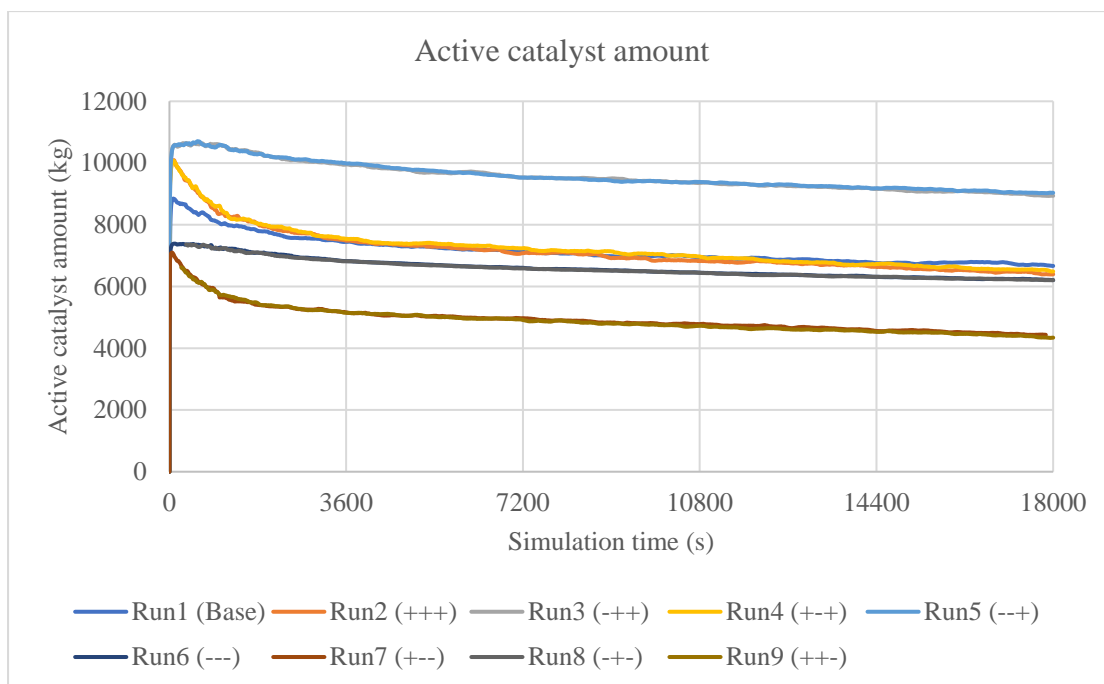


Figure 4.15 Instantaneous active catalyst amount in the system

Furthermore, from Figure 4.15, it can be observed that the amount of the active catalyst initially increases rapidly during the simulation due to the assumption of excess co-catalyst. However, active catalyst subsequently decreased due to the initiation reaction. The maximum amount of the active catalyst was dependent on the quantity of the catalyst, while the decreasing rate of active catalyst depended on the concentrations of the monomer and comonomer. Interestingly, the weight-average molecular weight was not affected by changes in the amount of catalyst. This was because weight-average molecular weight calculations assigned greater importance to heavier polymer chains. While increasing or decreasing of active catalyst amount affected to small polymer chain more than large chain.

However, when considering the number-average molecular weight, it was affected by changes in the amount of catalyst. Increasing the amount of catalyst

resulted in a decrease in the number-average molecular weight, while decreasing the amount of catalyst led to an increase in the number-average molecular weight. Since the number-average molecular weight gave equal importance to all polymer chains, changes in the amount of active catalyst due to catalyst variations affected the smaller polymer chains. An increase in the active catalyst amount led to an increase in the small chain content due to the initiation reaction, thus causing a decrease in the number-average molecular weight. Conversely, a decrease in the active catalyst amount resulted in a decrease in the small chain content, leading to an increase in the number-average molecular weight.

Polydispersity index

The polydispersity index (PDI) is calculated by dividing the weight average molecular weight by the number average molecular weight of a polymer. It is commonly employed as a measure to evaluate the width of molecular weight distributions in polymers. In comparison to the literature data [6, 36], the PDI value reported in those studies was around 4. In this model, the PDI reached 3.75 at 18000 seconds of simulation time, which closely matched the literature data.

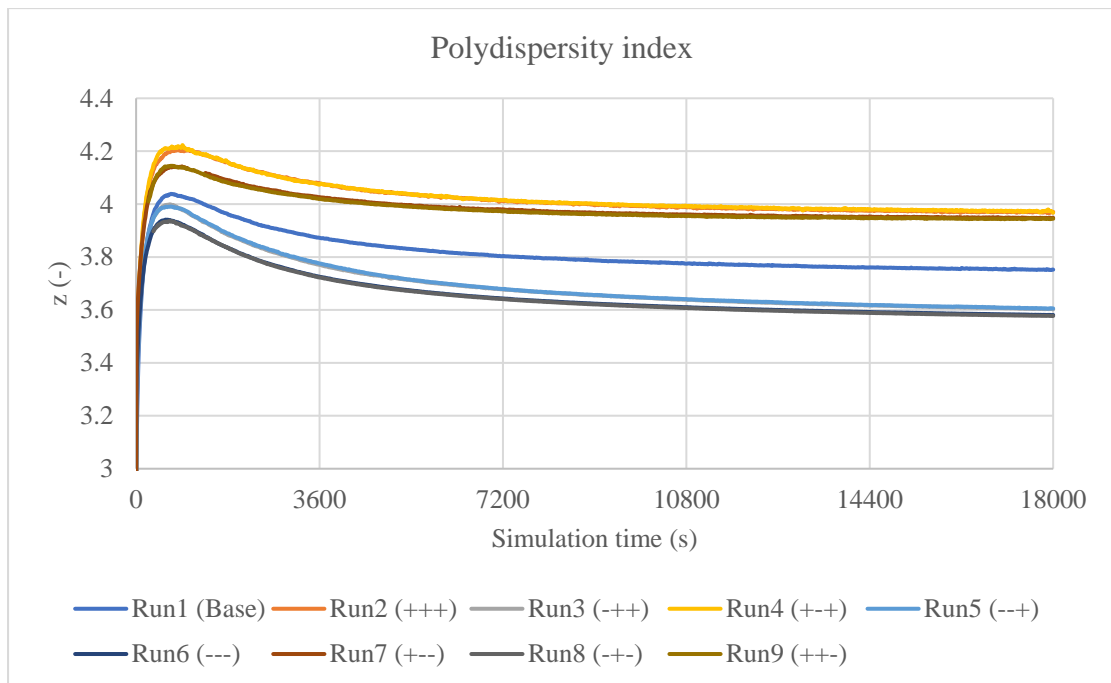


Figure 4.16 Instantaneous polydispersity index

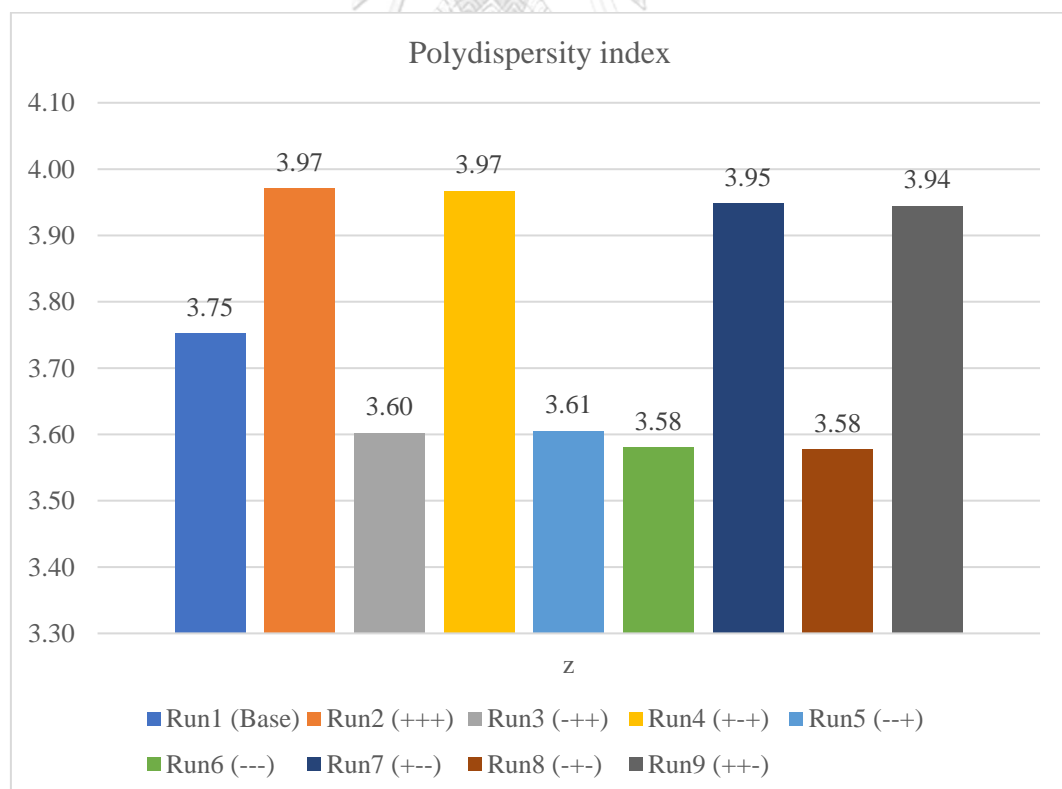


Figure 4.17 Polydispersity index at 18000 seconds

Table 4.6 Analysis of variance table of polydispersity index

Source	Sum of Squares	DF	Mean Square	F Value	Prob > F
Model	2.69E-01	3	8.97E-02	1.83E+04	< 0.0001
%Comonomer	2.68E-01	1	2.68E-01	5.47E+04	< 0.0001
H2toC2 ratio	5.80E-06	1	5.80E-06	1.183	0.3380
Catalyst amount	1.13E-03	1	1.13E-03	230.711	0.0001
Residual	1.96E-05	4	4.90E-06		
Cor Total	2.70E-01	7			

Considering the polydispersity index (PDI) of the product, it was found that PDI was affected by the comonomer content and catalyst amount. An increase in the comonomer content resulted in an increased PDI value, while an increase in the catalyst amount also led to an increased PDI value.

Regarding the effect of the comonomer content, as illustrated in Figure 4.18, it was found that increasing the comonomer content affected the weight-average molecular weight more than the number-average molecular weight due to a higher kinetic rate constant of the propagation reaction compared to the initiation reaction. The higher kinetic rate implied that the added comonomer in the system was more likely to be utilized in the propagation reaction for chain growth rather than in the initiation reaction for generating a new chain.

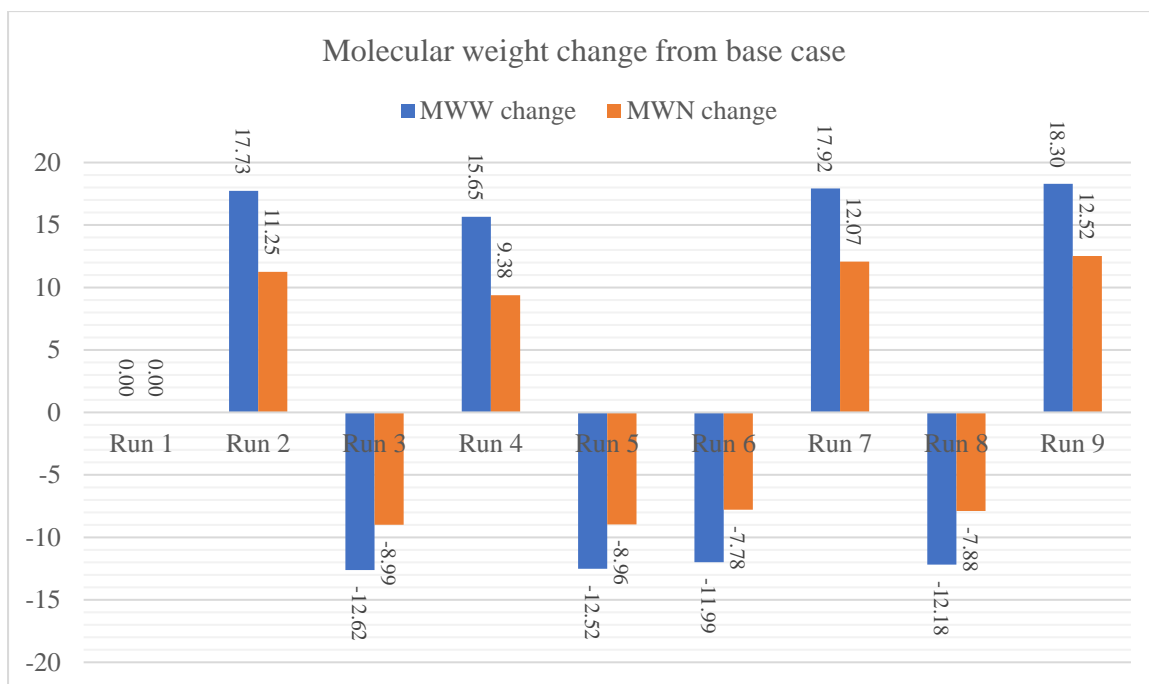


Figure 4.18 Percentage of molecular weight change

Since the increase in weight-average molecular weight was greater than the increase in number-weight molecular weight, it could be concluded that the fraction of long chains was higher compared to short chains, while the number of long chains did not increase at the same level. This behavior of the polymer product in the system resulted in a higher PDI value.

Moreover, as discussed in the section on molecular weight, it was found that the catalyst amount did not have a significant effect on the weight-average molecular weight. However, a significant effect on the number-average molecular weight was observed. The decrease in the number-average molecular weight, which resulted from an increasing amount of catalyst, suggested a greater increase in short chains compared to longer ones. This behavior led to an increase in the PDI value.

Chapter 5 Conclusion

In this study, a computational fluid dynamics model was utilized to investigate the copolymerization reaction of ethylene and 1-butene in a fluidized bed reactor. The polymerization model was developed using the method of moment approach. This chapter provides a concise summary of the study's novel findings in all sections, along with recommended avenues for future research. This study was divided into 2 parts as represented in Chapter III and IV:

Part I: Hydrodynamic model and segregation study

Part II: Computational fluidized dynamics model of ethylene-butene copolymerization reaction in fluidized bed reactor

Part I: Hydrodynamic model and segregation study

In this part, the dynamic behavior of a fluidized bed reactor was investigated using a two-dimensional model that employed the Euler-Euler approach. The model consisted of a four-phase system, including one gas phase and three solid particle phases. By conducting a grid independence test and considering the Courant number, the model provided reliable and accurate numerical results for the simulations. After adjusting the parameters and validating the model with existing literature data, it was confirmed that the model effectively represents the hydrodynamics of the fluidized bed reactor system.

During the development of the hydrodynamic model, segregation behavior was observed and investigated using a validated model. The effect of inserting baffles on segregation behavior was studied, with parameters such as baffles angle, baffles number, stage number, and stage arrangement being considered. The results suggested

that, in terms of relative segregation rate, inserting baffles with any configuration except for baffles with a 90-degree angle could reduce segregation behavior. The best configuration was found to be “above case” due to particles hindering, swirling and accumulation between the baffles stage.

Part II: Computational fluidized dynamics model of ethylene-butene copolymerization reaction in fluidized bed reactor

In this part, a copolymerization model developed using the method of moments was introduced to the hydrodynamic model to investigate the copolymerization reaction in a fluidized bed reactor. Weight-average, number-average, and polydispersity index were calculated from the model results and validated with literature data. The results showed lower weight-average and number-average molecular weights when compared with literature data due to the inhomogeneity of the system. However, the instantaneous weight-average and number-average molecular weights exhibited the same trend as the literature data. Thus, the model was used to investigate the operating parameters, including comonomer content, H₂-to-C₂ ratio, and catalyst amount. Weight-average, number-average, and polydispersity index were calculated and analyzed using statistical instruments.

The analysis results showed that the comonomer content directly affected the weight-average, number-average, and polydispersity index due to an increase in the propagation reaction rate. The catalyst amount had no effect on the weight-average molecular weight, while it inversely affected the number-average molecular weight due to variations in the initiator amount. However, the H₂-to-C₂ ratio had no effect on

the weight-average, number-average, and polydispersity index due to the small amount of hydrogen present in the system.

Research outcome and novel contribution

- The understanding of the method to develop a polymerization model through the method of moments.
- The understanding of the method to incorporate the polymerization model into a computational fluid dynamics model using the commercial program ANSYS FLUENT.
- The computational fluid dynamics model includes a polymerization model that can represent the ethylene-butene copolymerization reaction in the fluidized reactor.
- The understanding of segregation behavior and the effect of the baffles on segregation behavior.
- The understanding of the effect of operating parameters on the properties of the polymer product.

Limitation of the model

Limitations of the model arose due to the complexity of the polymerization reaction, necessitating the introduction of numerous assumptions to simplify the development process. Despite this, model validation demonstrated a good agreement between the model data and literature data. However, some assumptions did affect the model data, particularly the site-type of the catalyst. The use of 2-site types of the catalyst was lower than that of the real catalyst, which had over 5-site types.

Additionally, the pseudo-kinetic rate represented an average kinetic rate of each reaction in each computational cell. As the reaction in this system involved copolymerization, using an average value of the kinetic rate might lead to variations in the amount of the polymer product across different reactions during moment value calculations. These assumptions present limitations in the model and should be corrected in further studies.

Nevertheless, the model effectively represents this specific system due to the good agreement observed between the model data and literature data. To apply this model to simulate a different system, a validation method is recommended.

Recommendations for future studies

- The model in chapter 3 and 4 should be integrated to represent the segregation of the catalyst particles in the polymerization reactor.
- Temperature-dependent parameters such as viscosity and density should be used in Chapter 4 to provide a more realistic representation of the polymer product in the fluidized bed reactor.
- The model in chapters 3 and 4 should be improved for accuracy by using a three-dimensional model instead of a two-dimensional model.

REFERENCES

1. อนันตวรสกุล, ศ., วิศวกรรมปฏิบัติการเกิดพอลิเมอร์. 2016.
2. McAuley, K.B., J.F. MacGregor, and A.E. Hamielec, *A kinetic model for industrial gas-phase ethylene copolymerization*, in *AIChE Journal*. 1990. p. 837-850.
3. Fernandes, F. and L. Lona, *Heterogeneous modeling for fluidized-bed polymerization reactor*, in *Chemical Engineering Science*. 2001. p. 963-969.
4. Kiashemshaki, A., et al., *Reactor modeling of gas-phase polymerization of ethylene*, in *Chemical Engineering and Technology*. 2004. p. 1227-1232.
5. Alizadeh, M., et al., *Modeling of fluidized bed reactor of ethylene polymerization*, in *Chemical Engineering Journal*. 2004. p. 27-35.
6. Kiashemshaki, A., N. Mostoufi, and R. Sotudeh-Gharebagh, *Two-phase modeling of a gas phase polyethylene fluidized bed reactor*, in *Chemical Engineering Science*. 2006. p. 3997-4006.
7. Patel, H., F. Ein-Mozaffari, and R. Dhib, *CFD analysis of mixing in thermal polymerization of styrene*, in *Computers and Chemical Engineering*. 2010. p. 421-429.
8. Fathi Roudsari, S., F. Ein-Mozaffari, and R. Dhib, *Use of CFD in modeling MMA solution polymerization in a CSTR*, in *Chemical Engineering Journal*. 2013. p. 429-442.
9. Mastan, E. and S. Zhu, *Method of moments: A versatile tool for deterministic modeling of polymerization kinetics*, in *European Polymer Journal*. 2015. p. 139-160.
10. Xu, C.Z., et al., *CFD modeling of styrene polymerization in a CSTR*, in *Chemical Engineering Research and Design*. 2017. p. 46-56.
11. Xie, L., et al., *Multiscale Modeling of Mixing Behavior in a 3D Atom Transfer Radical Copolymerization Stirred-Tank Reactor*, in *Macromolecular Reaction Engineering*. 2017, Wiley-VCH Verlag.
12. Sarkar, D.K., *Fluidized-Bed Combustion Boilers*, in *Thermal Power Plant*. 2015. p. 159-187.
13. Wu, G., W. Chen, and Y. He, *Investigation on gas–solid flow behavior in a multistage fluidized bed by using numerical simulation*, in *Powder Technology*. 2020, Elsevier B.V. p. 251-263.
14. Kersten, S.R.A., et al., *Principles of a novel multistage circulating fluidized bed reactor for biomass gasification*, in *Chemical Engineering Science*. 2003, Elsevier Ltd. p. 725-731.
15. Li, Y., et al., *The simultaneous removal of SO₂ and NO from flue gas over activated coke in a multi-stage fluidized bed at low temperature*, in *Fuel*. 2020, Elsevier Ltd. p. 117862.
16. Davarpanah, M., et al., *Modeling VOC adsorption in a multistage countercurrent fluidized bed adsorber*, in *Chemical Engineering Journal*. 2020, Elsevier B.V. p. 124963.
17. Chen, Z., et al., *Coupling coal pyrolysis with char gasification in a multi-stage fluidized bed to co-produce high-quality tar and syngas*, in *Applied Energy*. 2018, Elsevier Ltd. p. 348-355.
18. Yang, S., H. Li, and Q. Zhu, *Experimental study and numerical simulation of*

- baffled bubbling fluidized beds with Geldart A particles in three dimensions*, in *Chemical Engineering Journal*. 2015, Elsevier. p. 338-347.
19. Jang, H.T., T.S. Park, and W.S. Cha, *Mixing-segregation phenomena of binary system in a fluidized bed*, in *Journal of Industrial and Engineering Chemistry*. 2010, The Korean Society of Industrial and Engineering Chemistry. p. 390-394.
 20. Zhang, Y., et al., *The exit impact on segregation of binary particles in the CFB system*, in *Powder Technology*. 2018, Elsevier B.V. p. 930-938.
 21. Park, H.C. and H.S. Choi, *The segregation characteristics of char in a fluidized bed with varying column shapes*, in *Powder Technology*. 2013, Elsevier B.V. p. 561-571.
 22. Akbari, V., et al., *Model-based analysis of the impact of the distributor on the hydrodynamic performance of industrial polydisperse gas phase fluidized bed polymerization reactors*, in *Powder Technology*. 2014, Elsevier. p. 398-411.
 23. Akbari, V., et al., *A CFD-PBM coupled model of hydrodynamics and mixing/segregation in an industrial gas-phase polymerization reactor*, in *Chemical Engineering Research and Design*. 2015, Institution of Chemical Engineers. p. 103-120.
 24. Akbari, V., et al., *2D CFD-PBM simulation of hydrodynamic and particle growth in an industrial gas phase fluidized bed polymerization reactor*, in *Chemical Engineering Research and Design*. 2015, Institution of Chemical Engineers. p. 53-67.
 25. ToolBox, T.E. *Fluid Flow - Equivalent Diameter*. 2003 [cited 2023 13/07]; Available from: https://www.engineeringtoolbox.com/equivalent-diameter-d_205.html.
 26. Coroneo, M., et al., *CFD prediction of segregating fluidized bidisperse mixtures of particles differing in size and density in gas-solid fluidized beds*, in *Chemical Engineering Science*. 2011, Pergamon. p. 2317-2327.
 27. Cornelissen, J.T., et al., *CFD modelling of a liquid-solid fluidized bed*, in *Chemical Engineering Science*. 2007, Pergamon. p. 6334-6348.
 28. Canonsburg, T.D., *ANSYS Fluent Theory Guide*, in *ANSYS Inc., USA*. 2013. p. 814.
 29. VASQUEZ, S. and *A Phase Coupled Method for Solving Multiphase Problems on Unstructured Mesh*. 2000.
 30. Inc., A., *ANSYS® Academic Research CFD, Release 2020 R2, Fluent User's Guide*. 2020.
 31. Grace, J., X. Bi, and N. Ellis, *Essentials of Fluidization Technology*. 2020.
 32. Goldschmidt, M.J.V., et al., *Digital image analysis measurements of bed expansion and segregation dynamics in dense gas-fluidised beds*, in *Powder Technology*. 2003. p. 135-159.
 33. Abbasi, M.R., A. Shamiri, and M.A. Hussain, *Dynamic modeling and Molecular Weight Distribution of ethylene copolymerization in an industrial gas-phase Fluidized-Bed Reactor*, in *Advanced Powder Technology*. 2016, Elsevier B.V. p. 1526-1538.
 34. Abbasi, M.R., et al., *Dynamic process modeling and hybrid intelligent control of ethylene copolymerization in gas phase catalytic fluidized bed reactors*, in *Journal of Chemical Technology and Biotechnology*. 2019.
 35. Tobita, H. and A.E. Hamielec, *Kinetics of free-radical copolymerization: the*

- pseudo-kinetic rate constant method*, in *Polymer*. 1991.
36. Kusolsongtawe, T. and P. Bumroongsri, *Two-stage modeling strategy for industrial fluidized bed reactors in gas-phase ethylene polymerization processes*, in *Chemical Engineering Research and Design*. 2018, Institution of Chemical Engineers. p. 68-81.





จุฬาลงกรณ์มหาวิทยาลัย
CHULALONGKORN UNIVERSITY

VITA

NAME	Suchart Kreesaeng
DATE OF BIRTH	25 August 1987
PLACE OF BIRTH	Prachuapkhirikhan
INSTITUTIONS ATTENDED	Chulalongkorn University Silpakorn University
HOME ADDRESS	9/190 Bang Phai, Mueang Nonthaburi District, 11000
PUBLICATION	Kreesaeng S, Chalermnsinsuwan B, Piumsomboon P. Effect of Channel Designs on Open-Cathode PEM Fuel Cell Performance: A Computational Study. <i>Energy Procedia</i> . 2015 Nov 1;79:733–45.
AWARD RECEIVED	Best poster award certificate from Kreesaeng, T., Chalermnsinsuwan, B. and Piumsomboon, P. Effect of channel design and operating parameters on open-cathode PEM fuel cell performance: A computation study. 2015 International Conference on Alternative Energy in Developing Countries and Emerging Economies (2015 AEDCEE), Bangkok, Thailand (2015) Best poster award certificate from Kreesaeng, T., Chalermnsinsuwan, B. and Piumsomboon, P. Effect of inserting baffles on the solid particle segregation behavior in fluidized bed reactor: a computational study. 2022 7th International Conference on Renewable Energy and Conversation (ICREC 2022), Paris, France (2022)